

INFORMATION TO USERS

This manuscript has been reproduced from the microfilm master. UMI films the text directly from the original or copy submitted. Thus, some thesis and dissertation copies are in typewriter face, while others may be from any type of computer printer.

The quality of this reproduction is dependent upon the quality of the copy submitted. Broken or indistinct print, colored or poor quality illustrations and photographs, print bleedthrough, substandard margins, and improper alignment can adversely affect reproduction.

In the unlikely event that the author did not send UMI a complete manuscript and there are missing pages, these will be noted. Also, if unauthorized copyright material had to be removed, a note will indicate the deletion.

Oversize materials (e.g., maps, drawings, charts) are reproduced by sectioning the original, beginning at the upper left-hand corner and continuing from left to right in equal sections with small overlaps.

Photographs included in the original manuscript have been reproduced xerographically in this copy. Higher quality 6" x 9" black and white photographic prints are available for any photographs or illustrations appearing in this copy for an additional charge. Contact UMI directly to order.

**Bell & Howell Information and Learning
300 North Zeeb Road, Ann Arbor, MI 48106-1346 USA
800-521-0600**

UMI[®]

**OPTICALLY PUMPED NMR STUDY
OF ELECTRON SPIN DYNAMICS IN THE
FRACTIONAL QUANTUM HALL REGIME**

**A Dissertation
Presented to the Faculty of the Graduate School
of
Yale University
in Candidacy for the Degree of
Doctor of Philosophy**

**by
Nicholas Kuzma**

Dissertation Director: Sean Barrett

December 1999

UMI Number: 9954328

UMI[®]

UMI Microform 9954328

Copyright 2000 by Bell & Howell Information and Learning Company.

**All rights reserved. This microform edition is protected against
unauthorized copying under Title 17, United States Code.**

**Bell & Howell Information and Learning Company
300 North Zeeb Road
P.O. Box 1346
Ann Arbor, MI 48106-1346**

ABSTRACT

OPTICALLY PUMPED NMR STUDY OF ELECTRON SPIN DYNAMICS IN THE FRACTIONAL QUANTUM HALL REGIME

Nicholas N. Kuzma
Yale University
December 1999

A new optically pumped nuclear magnetic resonance (OPNMR) laboratory has been built at Yale to extend the study of spin physics in the quantum Hall regimes to lower temperatures ($T \sim 300$ mK) and higher magnetic fields ($B \sim 12$ T).

This facility was used to measure the electron spin polarization \mathcal{P} as a function of temperature and the Landau level filling factor ν around $\nu = 1/3$ in two different electron-doped multiple quantum well samples. In addition, our OPNMR measurements provided the first evidence that below $T \approx 500$ mK, the spin-reversed charged excitations of the $\nu = 1/3$ ground state become spatially localized over the NMR time scale of about 40 microseconds.

The two-dimensional electron spin system at $\nu = 1/3$ could also be driven out of equilibrium by varying NMR pulse parameters, which led to the establishment of electron spin temperature different from the crystalline lattice temperature. Observation of this effect implies that for $T < 500$ mK the electron spin-lattice relaxation time τ_{1s} is between 100 microseconds and 500 milliseconds at $\nu = 1/3$.

We also report a preliminary attempt to use OPNMR as a probe of material properties in heterostructures made of GaN — a novel semiconductor with a band gap in the blue region of visible spectrum. Our first NMR measurements of the quadrupole shift and the linewidth at 1.5 K $< T < 300$ K provide evidence that the local electric field gradients have an angular scatter of $\pm 2^\circ$, exceeding the spread in the local crystalline lattice orientations by a factor of ~ 20 .

To my Parents
Nikolai Nikolaevich and Yaroslava Mikhailovna

Acknowledgements

I would like to thank Professor Sean Barrett for accepting me into his research group and for being my teacher when I needed one the most. Our first discussions of skyrmion physics and the magical trick of optical pumping took place amidst two empty rooms in the Sloane Lab basement back in January 1995. Since then that space has been transformed into a functional laboratory, where a lot of new science was discovered beyond our boldest expectations. I am indebted to Sean for teaching me NMR as well as many other useful things, from giving talks to creating that special atmosphere among the people you work with. Five years with Sean have been a fascinating experience for me, during which difficulties and hardships were outweighed by the sheer joy of working in Sean's group. A feeling of belonging that I still keep in my heart.

It was my privilege to work with Pankaj Khandelwal and, recently, Tolva Demen-tyev, on the projects described in this thesis and beyond. Pankaj joined the lab in the fall of 1995, when the big construction had barely started. Without his energy, skills, and effort our dreams would have never turned into a working lab, and ultimately, the data. We have shared a lot of desperate nights in the machine shop working on the rotator mechanism, as well as quite a number of far more pleasant night shifts spent at the spectrometer (one of us perched on top of the eight-foot ladder rotating the sample) as the data were coming out of the system. Working on the experiment together, we had never divided it into separate projects, until the time came to write

about it in the thesis. Thus, Pankaj deserves as much credit as I do for what is reported here, although it is only a fraction of the work done so far.

Anatoly Dementyev has been an excellent friend, whom I met just after he arrived at Yale. Our laboratory has benefited enormously from his enthusiasm and his desire to pursue the physical truth until all possible experimental means are exhausted. Tolya's persistence and sharp eyes (or, maybe, his great belief that he could see a peak) have led to the discovery of GaN satellite transitions, discussed in Chapter 7. I am happy that the system put together by us has already served him well: in the short time since Tolya joined us, an extensive set of measurements has been completed, with new results on composite fermion interactions and skyrmion dynamics. It was fun helping Tolya take the data and discuss with him and Pankaj the ways in which their new work supports and complements the results described here.

I want to thank all members of Professor Daniel Prober's group, and especially Peter Burke, Jim McCambridge, and Nick Rizzo for being patient with me and showing me many quick and practical ways to do science in this country. Anthony Massini taught me the fine art of machining during his class, and later provided an invaluable assistance with the rotator project. Professor Cornelius Beausang and the three generations of students taking Physics 381 in 1997-99 taught me how to teach, and I want to thank them for helping me organize a field trip to our NMR lab.

I would like to thank Professors Kurt Zilm, Robert Grober, Kurt Gibble, Mark Kasevich, David DeMille, and members of their groups, as well as staff of the Gibbs machine shop for sharing their expertise with us and lending us pieces of equipment and critical spare parts. I am also grateful to Professors Nicholas Read, Subir Sachdev, and Robert Schoelkopf for helpful discussions.

Stepan Fedorovich Isaev was my first math teacher. The door of his home was always open for me, and I will never forget the excitement and clarity with which we analyzed the most challenging problems. I also want to thank my physics teacher

Tatyana Nikolaevna Perenesey for putting so much of her work, energy, and spare time into all of us, was it an electricity experiment or a hike to the national song festival.

Alexander Rafailovich Zilberman has helped me to find my way in life. He shared with me and with many other desperate souls like myself his words, his books, his physics problems and computer chips, his classes and his tea stories, and in fact much more. His heart. I want to thank him for always being there for us, no matter how big or small our problems are.

I want to thank my roommates Konstantin Zuev, Alexander Korshkov, Mykola Schwetz, Kedar Damle, Joe Boyer, and Karl Voss for keeping in touch with me long after we moved apart, and for still accepting me at their homes now, any past experiences notwithstanding.

I would like to thank Yulia Dzhashiashvili and her family for their hospitality, love, and enormous moral support. Yulia's help was especially critical at the final stages of preparing this thesis and turning it in.

Finally, I want to express my gratitude to my parents, Nikolai Nikolaevich and Yaroslava Mikhailovna, for all that they have done towards this Ph.D. degree. The credit rightfully belongs to them much more than it does to me, and I am delighted to dedicate this dissertation to them. On behalf of my Mom and myself I would like to thank Sean and Nancy Barrett again for their hospitality, and for the good care they have taken of both of us while we were here.

Contents

Acknowledgements	ii
List of Tables	ix
List of Figures	xi
1 Introduction	1
2 Brief Review of the Quantum Hall Effect	7
2.1 The Classical Hall Effect	7
2.2 Basic Phenomenology of the Integer Quantum Hall Effect	8
2.3 Quantum-Mechanical Description	8
2.4 The Fractional Quantum Hall Effect	13
2.5 Spin in the Quantum Hall Effect	15
3 Optically Pumped NMR: Background and Previous Results	19
3.1 Optical Pumping and Dynamic Polarization	19
3.2 OPNMR Evidence for Skyrmions	21
3.3 Recent Applications of Optical Pumping beyond GaAs	24
4 Experimental Set-Up	25
4.1 Multiple Quantum Well Samples	25

4.2	Tilted Field Approach: The Swedish Rotator	28
4.3	NMR Techniques	32
4.3.1	Superconducting Magnet: Preparing the Field	32
4.3.2	Home-Built NMR Spectrometer. Pulse Generation	34
4.3.3	NMR Tank Circuits. Power Handling	37
4.3.4	Quadrature Detection and Signal Processing	39
4.3.5	OPNMR Timing Sequence	40
4.4	Optical Pumping	42
4.5	Temperature Control	45
5	Equilibrium OPNMR Measurements of Electron Spin Polarization and Dynamics in the Quantum Hall Regimes	51
5.1	Effects of Optical Pumping on NMR Spectra	51
5.1.1	Primitive Optical Spectroscopy: Optimizing the Wavelength	56
5.2	A “Motionally Narrowed” Interpretation of the OPNMR Line Shape	58
5.3	Skyrmion Peak at $\nu=1$: Measurements of Electron Density	63
5.4	Knight Shift Data in the Vicinity of $\nu=\frac{1}{2}$	65
5.4.1	Temperature Dependence $K_N(T)$ at $\nu=\frac{1}{2}$	65
5.4.2	Charged Quasiparticles: $K_N(\nu)$ Data around $\nu=\frac{1}{2}$	71
5.5	Broadening of the OPNMR Lineshape at $\nu < \frac{1}{2}$	76
5.6	Break-Down of Motional Narrowing	83
6	Non-equilibrium Measurements of Electron Spin Relaxation	91
6.1	Detection of RF heating	91
6.2	Knight Shift Thermometry of the Electron Spin System	94
6.3	Evidence for Establishment of a Common Electron Spin Temperature	96
6.4	Constraints on Possible Heating Mechanisms	98
6.5	An Upper Limit for Electron Spin Relaxation Time	101

7	NMR Measurements in GaN Epitaxial Films	103
7.1	Introduction and Theory	103
7.2	GaN Samples	108
7.3	NMR Spectroscopy	111
7.4	Search for the Satellites	113
7.5	Characterization of the Disorder	117
7.6	Future Goals	121
8	Conclusions	125
A	Calibration of RuO₂ thermometer in high magnetic fields	127
B	Quadrupole Aluminum NMR as a Precision Tilt Sensor	129
	Bibliography	133

List of Tables

4.1	Dimensions and other parameters of the GaAs samples	26
4.2	Gyromagnetic ratios and various NMR data for some nuclei of interest	36
5.1	Saturation of $K_2(T)$ at low temperature in the GaAs samples	70
7.1	Dimensions and composition data for the GaN samples	110
A.1	Measured field dependence of the RuO ₂ calibration data	127
A.2	Interpolation coefficients for the field-dependent RuO ₂ calibration	128

List of Figures

2.1	The Hall bar and other possible quantum Hall geometries	9
2.2	The integer quantum Hall effect: $\rho_{xy}(B)$ and $\rho_{xx}(B)$ data	10
2.3	The fractional quantum Hall effect: $\rho_{xy}(B)$ and $\rho_{xx}(B)$ data	14
2.4	Spin waves and skyrmions, schematic diagram	17
3.1	OPNMR measurements of electron spin polarization by Barrett et al.	22
4.1	Quantum well sample	27
4.2	Swedish rotator assembly	29
4.3	Set-up for testing the Swedish rotator	30
4.4	Schematic diagram of the home-built radio frequency spectrometer	35
4.5	Resonant tank circuits used in the NMR probe	38
4.6	OPNMR timing sequence	41
4.7	Optical assembly	43
4.8	Arrangement of the thermometer plate below the sample	47
4.9	Temperature response to laser light pulses	49
5.1	Examples of NMR spectra acquired without optical pumping	53
5.2	Typical optically pumped NMR spectra	54
5.3	OPNMR signal amplitude as a function of laser wavelength	57
5.4	Interpretation of motionally narrowed OPNMR spectra	59

5.5	Variation of local OPNMR parameters across the quantum well	61
5.6	$K_S(\nu)$ data near $\nu=1$	64
5.7	OPNMR spectra at $\nu=\frac{1}{3}$ as a function of temperature	66
5.8	Knight shift dependence on temperature, measured at $\nu=\frac{1}{3}$	68
5.9	Electron spin polarization as a function of temperature at $\nu=\frac{1}{3}$	69
5.10	$K_S(\nu)$ dependence near $\nu=\frac{1}{3}$	72
5.11	Electron spin polarization dependence on the filling factor near $\nu=\frac{1}{3}$	74
5.12	OPNMR spectra at $\nu = 0.267$ as a function of temperature	77
5.13	OPNMR spectra at $T = 0.46$ K as a function of the filling factor	78
5.14	Linewidth and K_S as functions of temperature for $0.267 \leq \nu \leq 1/3$	82
5.15	Simulated OPNMR spectra for the break-down of motional narrowing	85
5.16	Linewidth and K_S for $\nu \geq 1/3$ and in the other sample	87
5.17	“Topological” plot of the line width vs. Knight shift	88
6.1	OPNMR spectra showing the effects of rf heating at $T = 0.45$ K	93
6.2	Dependence of the effective spin temperature on the rf pulse length	95
6.3	Equivalence of rf-heated and conventionally heated OPNMR spectra	97
6.4	Time scale constraints on a possible scenario of rf heating	99
6.5	Evolution of the OPNMR line shape as a function of dark time	102
7.1	Bandgaps and lattice constants of common semiconductors	105
7.2	Simulated electric field profiles across a GaN quantum well	106
7.3	Schematic diagram of the GaN thin film samples	109
7.4	NMR spectra of GaN thin films at room and cryogenic temperatures	112
7.5	2 nd order shift of the central transition frequency as a function of tilt	115
7.6	The upper ⁶⁹ Ga satellite ($m = -\frac{1}{2} \rightarrow -\frac{1}{2}$) transition	118
7.7	Linewidth of the ⁶⁹ Ga central transition as a function of tilt	119
7.8	Attempts to detect indium NMR from a 200 nm epitaxial layer	122

7.9	OPNMR signal from a single GaAs quantum well	124
B.1	Typical ^{27}Al spectrum from a single crystal sapphire substrate	130
B.2	Quadrupole splitting in sapphire as a function of tilt	131
B.3	Quadrupole ^{27}Al NMR as a precision tilt sensor	132

Chapter 1

Introduction

One of the greatest successes of 20th century physics has been the ongoing development of a unified theoretical framework, which describes both the properties of materials used in everyday life and many exotic phenomena that have been discovered in modern physics laboratories around the world. To gain insights into the fundamental principles underlying this framework, matter is studied in extreme environments, such as ultra-low temperatures, high pressures, and strong magnetic fields. Under these extraordinary conditions, quantum mechanics gives rise to surprising effects in macroscopic systems, such as superconductivity, superfluidity, Bose-Einstein condensates of laser-cooled atoms, and the Quantum Hall effect (QHE). These macroscopic quantum phenomena possess many highly unusual properties, ranging from dissipationless transport of electricity through matter to nuclear ferromagnetism (as in superfluid ³He), vortices in superconductors and superfluids, and long-range entropy waves (second sound).

In most of these cases a macroscopic many-particle system finds itself in a configuration where all microscopic details of motion of a large number of individual constituents can be reduced to a small set of quantum numbers, which characterize the entire system in a neighborhood of a certain quantum-mechanical state. Pertur-

bations away from this special state can be described as sparse, weakly interacting “quasiparticles”, while the unperturbed background plays a role of the “vacuum”. These phenomena are especially appealing from a physicist’s point of view, since the systems that exhibit them are well-defined enough to develop a detailed first-principles theory, and at the same time offer experimental access to their quantum-mechanical parameters. Each discovery of a new macroscopic quantum system stimulated tremendous progress both in theory (e.g. Landau-Feynman theory of liquid helium, Bardeen-Cooper-Schrieffer theory of superconductivity) and experiment (SQUID magnetometry, atom interferometry, and many others).

Technological advances of the 70’s made it possible to trap electrons within extremely thin ($\sim 10^2$ Å) semiconductor layers, which opened up the study of two-dimensional electron systems (2DES) by condensed matter physics. While being of significant theoretical interest because of its fundamental properties, the 2DES is also closely related to the development of fabrication technology and has practical uses in electronics (e.g. in high electron mobility transistors, or HEMTs).

Application of strong magnetic fields (~ 10 Tesla) perpendicular to clean, high electron mobility¹ 2DES samples at low temperatures (< 2 K) led to discoveries of the integer quantum Hall effect (IQHE) by von Klitzing et al. in 1980 [1] and the fractional quantum Hall effect (FQHE) by Tsui et al. in 1982 [2]. They found that the Hall conductivity is quantized in integer or simple fractional multiples of the fundamental constant e^2/h with a remarkable precision (now better than 10^{-8}). The integer or fraction turns out to be equal to the Landau filling factor ν , defined as the number of electrons per unit flux quantum.

Several theoretical breakthroughs led to a very detailed picture of the physics governing the QHE [3, 4, 5]. While the “standard model” of the QHE is very well de-

¹Better than 10^4 cm²/(V s) for SiO₂ inversion layers and 10^6 cm²/(V s) for GaAs quantum wells.

veloped, it has been almost exclusively based upon and constrained by a single type of experiment, namely magnetotransport measurements. Indeed, while the transport measurements are uniquely suited to probe some fundamental characteristics of 2DES, they do not provide direct access to other important parameters, such as magnetization, spatial distribution of the carriers, etc. Therefore, in order to deepen our understanding of the physics of 2DES, it is imperative to develop new experimental probes. The data produced by these novel techniques will provide an extra testing ground for the existing theories, and may expose entirely new phenomena which would stimulate further theoretical progress.

Nuclear magnetic resonance (NMR) spectroscopy, which has made important contributions to condensed matter physics [6], is certainly a natural candidate for a new probe of 2DES. In principle, simple NMR measurements could be quite informative. The local field at the nucleus can be decomposed into fields produced by the laboratory magnet, the electron orbital momentum, the electron spins, the nuclear spins, etc., each contributing to the frequency of the resonance. The electron spin contribution is small (≤ 100 ppm), but detectable, and is called the Knight shift (K_s) [7]. The NMR lineshape can also provide insights into the dynamics of 2DES, while the nuclear spin-lattice relaxation time (T_1) measurements characterize electron spin-flip scattering processes. Thus, NMR experiments could be complimentary to magnetotransport measurements, since the latter do not directly probe the electron spin degree of freedom. This is particularly interesting because the Zeeman energy of valence electrons in the available magnetic fields is much smaller than the Coulomb interaction energy, which makes the spin degree of freedom uniquely sensitive to electron-electron correlations.

The typical dimensions of quantum semiconductor structures, however, make it difficult to use conventional NMR as a viable probe of 2DES. Sandwiched between thick barriers, the semiconductor quantum wells containing the 2DES are just a tiny

fraction ($< 1\%$) of the bulk sample. In equilibrium, the NMR signal produced by them is overshadowed by the tail of a much larger barrier signal that is at nearly the same frequency. Finally, typical nuclear Zeeman splittings (~ 5 mK in temperature units) correspond to the polarization of nuclei that is small even at low temperatures (~ 1 K) and high magnetic fields (~ 10 Tesla). As a result, typical noise levels greatly exceed the NMR signals from nuclei in the quantum wells. Going to still lower temperatures does not help much because the equilibration time of the nuclei becomes much longer than the time scale of the experiment.

Fortunately, a technique called optically pumped nuclear magnetic resonance (OP-NMR) has been able to circumvent the above difficulties. It involves resonant excitation of the electrons across the bandgap of a semiconductor quantum well using circularly polarized laser light, which creates a non-equilibrium electron spin configuration. The subsequent electron relaxation drives the nuclei into a highly polarized state, in a spin-spin $\mathbf{I}\cdot\mathbf{S}$ interaction process closely related to the Overhauser effect [6, 8]. This leads to a selective enhancement of the quantum well NMR signal by a factor of ~ 100 , making possible its direct, radiofrequency detection [9]. Due to the enormous difference in relaxation times between the electronic and nuclear spin systems ($\tau_{1e}/T_1 < 10^{-9}$), we can turn off the laser light, wait for the electrons to equilibrate, and still use an enhanced non-equilibrium nuclear spin polarization as a probe of an equilibrium 2DES.

In this Dissertation, we report OPNMR measurements in both fractional ($\nu = \frac{1}{3}$) and integer ($\nu = 1$) quantum Hall regimes, primarily focusing on the Knight shift and linewidth of the quantum well signal at and around $\nu = \frac{1}{3}$. These two probes provide new detailed information about spin polarization and dynamics of the 2DES.

The main result of our measurements is that the charged excitations of the $\nu = \frac{1}{3}$ ground state exhibit small, but measurable amount of spin reversal, about $\sim \frac{1}{10}$ of a spin flip per quasiparticle or quasihole. This result is supported by the linewidth

measurements around $\nu = \frac{1}{3}$, which reveal rich spin dynamics of the 2DES. At each filling factor $\nu < \frac{1}{3}$, the linewidth exhibits a sharp maximum as a function of temperature at $T \approx 0.5$ K, indicating a transition from the “motionally narrowed” to a “frozen” OPNMR lineshape, consistent with our simulations. The amplitude of this maximum drops off as the filling factor approaches $\nu \rightarrow \frac{1}{3}$, which we interpret as an additional signature of spin reversal associated with the charged excitations of the $\nu = \frac{1}{3}$ state. Comparing the broadened spectra to the simulated line shapes provides us with an estimate of $\sim 40 \mu\text{s}$ for the time scale over which the charged quasiparticles are “localized”.

We have also performed measurements at a fixed filling factor $\nu = \frac{1}{3}$ as a function of temperature, which probe the neutral spin-flip excitations of this ground state. Our detailed $K_s(T)$ data indicate that $\nu = \frac{1}{3}$ is a very “fragile” ferromagnet, which loses its polarization at much lower temperatures compared to $\nu = 1$. These data can be directly converted to the electron spin polarization $P(T)$, which thus provides the first experimental benchmark for the future theories of spin in the fractional quantum Hall regime.

During our Knight shift measurements of the electron spin polarization it was important to keep the 2DES in equilibrium with its environment by using weak radio-frequency (rf) tipping pulses long after the laser light was turned off. We have found that an unexplained direct coupling of the rf fields to the spins of 2DES significantly perturbs this equilibrium, leaving the electron spin system trapped at a higher temperature (compared to the bulk of the sample) for a relatively long time of at least $100 \mu\text{s}$. This value is a factor of 1000 larger than any electronic time scale reported in semiconductors so far.

In Chapter 2 we review the “standard model” of the quantum Hall effect and the importance of novel spin-sensitive experimental techniques. In Chapter 3 we will discuss OPNMR experiments reported previously by other groups. The experimental

difficulties that we had to overcome before we could carry out our measurements are described in Chapter 4, along with the details of our NMR apparatus, the optical pumping set-up, and the temperature control. Chapter 5 starts with the basics of OPNMR spectroscopy and includes all of our equilibrium results on electron spin polarization and spin dynamics, whereas the non-equilibrium measurements of electron spin-lattice relaxation time are described in Chapter 6. In Chapter 7, we explore another application of the NMR/OPNMR technique, describing our preliminary investigations of GaN epitaxial layers. Chapter 8 contains our conclusions.

Chapter 2

Brief Review of the Quantum Hall Effect

2.1 The Classical Hall Effect

As was first discovered more than a hundred years ago by American graduate student Edwin Hall, a current flowing perpendicular to a magnetic field not only gives rise to the mechanical force on the conductor, but also leads to a measurable voltage drop *perpendicular* to the current. Figure 2.1(a) illustrates this for the classic “Hall bar”: when the field B is pointing along z and the current I is flowing through a flat bar along x , a Hall voltage V_H develops along y , which depends linearly on both B and I :

$$V_H = \frac{B}{q n} I. \quad (2.1)$$

where q is the charge, and n is the number of carriers per unit area. This relationship follows directly from a steady state balance between the Lorentz and Coulomb forces $q \vec{v} \times \vec{B} = q \vec{E}_H$ and can be used in practice to determine the sign of the carriers (e.g. electrons or holes), or as a convenient magnetic field probe (as in Hall sensors).

2.2 Basic Phenomenology of the Integer Quantum Hall Effect

The Quantum Hall effect takes place in very thin ($w \sim 100 \text{ \AA}$) conducting layers at low temperatures¹ and manifests itself in deviations from the linear form given in Eq. 2.1. It is natural to define the two-dimensional conductivity and resistivity tensors σ and $\rho = \sigma^{-1}$ in terms of the sheet current density \mathbf{j} and electric field \mathbf{E} as:

$$\mathbf{j} = \begin{pmatrix} \sigma_{xx} & \sigma_{xy} \\ \sigma_{yx} & \sigma_{yy} \end{pmatrix} \mathbf{E}, \quad \text{and} \quad \mathbf{E} = \begin{pmatrix} \rho_{xx} & \rho_{xy} \\ \rho_{yx} & \rho_{yy} \end{pmatrix} \mathbf{j}. \quad (2.2)$$

such that Equation 2.1 becomes: $\rho_{xy}(B) = \frac{1}{en} B$. (2.3)

The quantum Hall effect in a clean sample is observed as step-like deviations (or *plateaus*) in ρ_{xy} from this linear law, such as shown in Figure 2.2(a). Each plateau occurs precisely (to better than 10^{-6}) at:

$$\rho_{xy} \left(i^{\text{th}} \text{ plateau} \right) = \frac{1}{i} \frac{h}{e^2}. \quad (2.4)$$

where i is an integer, e is the electron charge, and h is the Planck's constant. Simultaneously, the diagonal components of resistivity vanish ($\rho_{xx} = \rho_{yy} = 0$) near the center of each plateau in ρ_{xy} , as Figure 2.2(b) demonstrates.

2.3 Quantum-Mechanical Description

Following Landau [11] and assuming non-interacting electrons of mass m^* and g -factor g^* (determined by the band structure of bulk GaAs), we can write a single

¹In sufficiently thin conducting layers, the perpendicular motion of the electrons is quantized. This motion will be completely suppressed, if the gap between the lowest and the next excited states (or "sub-bands") due to such quantization is much greater compared to the Boltzmann factor $k_B T$ as well as other energy scales involved. In this limit, we can speak about a "two-dimensional" electron system.

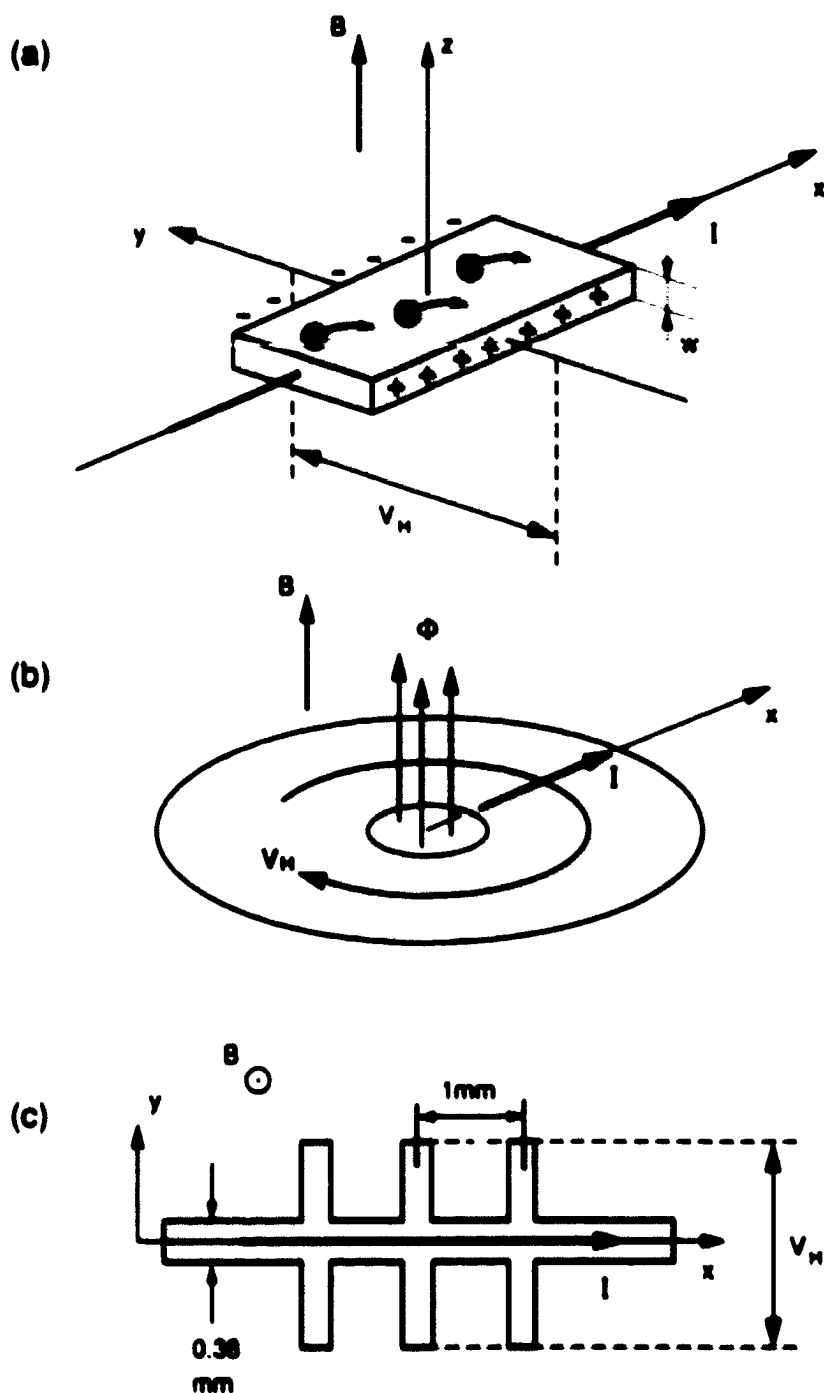


Figure 2.1: Sample geometries used in the quantum Hall effect: (a) the classic “Hall bar”. (b) a theorist’s concept of the “Corbino disk”, where the Hall voltage is applied azimuthally via $V_H = \frac{1}{2\pi} \Phi$ (as in Laughlin’s *Gedankenexperiment*), and (c) the top view of a typical sample used in magneto-transport measurements.

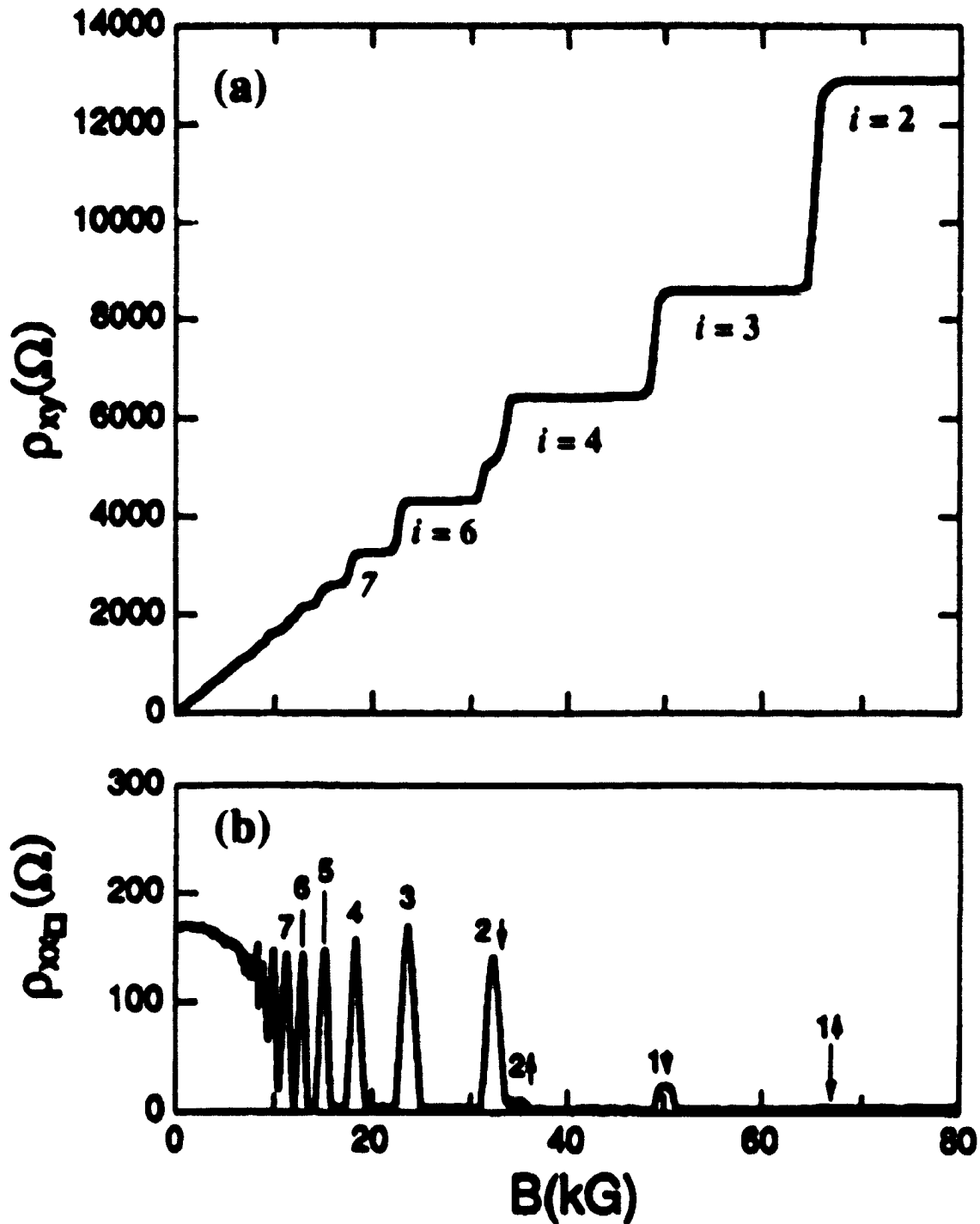


Figure 2.2: (a) Field dependence of the Hall resistivity ρ_{xy} , exhibiting plateaus at $h/e^2 = 25.812805 \text{ k}\Omega$ divided by an integer i . Plateaus for $i = 2, 3, 4, 6,$ and 7 can be clearly seen. (b) - The corresponding ρ_{xx} trace. Adapted from [10].

particle Hamiltonian as:

$$\mathcal{H} = \frac{1}{2m^*} \left(\hat{\mathbf{p}} - \frac{e}{c} \mathbf{A} \right)^2 - g^* \mu_B \mathbf{S} \cdot \mathbf{B} . \quad (2.5)$$

where μ_B is Bohr magneton. The magnetic vector potential \mathbf{A} can be chosen using Landau gauge ($A_y = Bx$, $A_x = A_z = 0$), which leads to the solution in the form²:

$$\psi(x, y) = \exp\left(\frac{i}{\hbar} p_y y\right) \chi(x) . \quad (2.6)$$

where $\chi(x)$ satisfies a linear oscillator equation:

$$\chi''(x) + \frac{2m^*}{\hbar^2} \left[(E + g^* \mu_B s B) - \frac{m^*}{2} \omega_c^2 (x - x_0)^2 \right] \chi(x) = 0 \quad (2.7)$$

with

$$\omega_c = \frac{eB}{m^*c} \quad \text{and} \quad x_0 = -\frac{c p_y}{eB} . \quad (2.8)$$

Thus the solutions $\psi(x, y)$ to Equation 2.5 can be expressed in terms of Hermite polynomials and are localized in x , but extended (as plain waves) along y , with the energy levels given by³:

$$E_n = \hbar \omega_c \left(n + \frac{1}{2} \right) \pm \frac{1}{2} g^* \mu_B B . \quad (2.9)$$

These are Landau levels, which in the absence of disorder are highly degenerate since p_y can assume any values in the continuum. If the geometry is finite, the momentum p_y becomes both quantized and limited since x_0 as defined by Eq. 2.8 corresponds to the center of $\chi(x)$ and has to be finite. The number of states per level can then be counted, and we can define Landau level filling factor as the number (integer or fractional) of these degenerate Landau levels occupied:

$$\nu = \frac{n \hbar c}{e B} . \quad (2.10)$$

²Here $i = \sqrt{-1}$.

³Note that in GaAs term $\hbar \omega_c$ is much larger than $E_Z = g^* \mu_B B$, so that Landau levels are arranged in pairs ($E_{2n+1} - E_{2n} = E_Z$), that are widely separated from each other.

where n is the two-dimensional electron density and $n_\phi = eB/hc$ is the density of magnetic flux quanta penetrating the sample plane. For example, at $\nu = 1$ the first Landau level is spin-up, with the next available state being spin-down, separated from others by a gap equal to Zeeman energy E_Z (see footnote on the previous page).

As the magnetic field changes (Fig. 2.2), the filling factor ν sweeps through the integer values, at which a gap to the next available state opens up and the system experiences sudden changes in energy needed to add or remove flux quanta. How does this lead to the observed plateaus in ρ_{xy} in Figure 2.2(a)?

Laughlin proposed an elegant explanation, which can be applied in the ‘‘Corbino’’ geometry, shown in Figure 2.1(b). We can pick the eigenfunctions (Eq. 2.6) such that they are localized in the radial dimension and extended around the annulus azimuthally. In our *Gedankenexperiment* we can apply the Hall voltage by varying a magnetic flux through the annulus, keeping the B field throughout the sample constant.

Extended states that enclose the varying magnetic flux will gain a phase factor of 2π around the loop for each extra quantum of magnetic flux added to the annulus, and thus their azimuthal momentum will change, resulting in the displacement of the wave function radially (since the radial coordinate and the azimuthal momentum correlate as r_0 and p_ϕ in Eq. 2.8). In each Landau level, the wave functions will shift into each other’s steps radially, transferring a unit of charge per Landau level, per flux quantum added, from one edge of the sample to the other.

In presence of some disorder this argument still holds, with one exception: the available states at the Fermi energy are localized, and thus do not contribute to the charge transport from edge to edge. This way the fundamental relation between the induced EMF $\mathcal{E} = \rho_{xy}I = \frac{e}{2\pi} \dot{\Phi}$ and the current $I = \frac{e}{2\pi} Q$ is fixed by Equation 2.4 even though the magnetic field is changing over a certain range. Thus the dependence of ρ_{xy} on the properties of just the extended states leads to the formation of plateaus.

2.4 The Fractional Quantum Hall Effect

Figure 2.3 illustrates the fractional quantum Hall effect, where by going to stronger magnetic fields and using samples with higher mobilities it is possible to observe plateaus similar to those in the integer effect, but occurring at the values of:

$$\rho_{xy} \text{ (plateau)} = \nu^{-1} \frac{h}{e^2}, \quad (2.11)$$

where $\nu = \frac{m}{n}$ is a simple fraction rather than an integer. The strongest effect takes place at $\nu = \frac{1}{3}$, with distinct plateaus in ρ_{xy} and minima in ρ_{xx} also observable at many other fractions, e.g. $\nu = \frac{1}{5}, \frac{2}{5}, \frac{2}{3}, \frac{3}{5}, \frac{4}{5}$, and so on.

Although similar in appearance to its integer predecessor, the fractional quantum Hall effect (FQHE) has one important distinction: it cannot be explained without considering electron-electron interactions. Indeed, the independent electron picture discussed in section 2.3 does not predict that any energy gaps — or any other feature — should be found at the fractional filling of $\nu = \frac{1}{3}$ as opposed to, for example, $\nu = \frac{1}{2}$.

By assuming that the electron spins are fully polarized by the strong magnetic fields at low temperatures, and keeping in mind the need to minimize Coulomb repulsion between electrons, Laughlin proposed the following famous form for the many-body electron wave function for a $\nu = \frac{1}{m}$ ground state [3]:

$$\psi_m(z_1, \dots, z_N) = \exp\left[-\frac{1}{4l_B^2} \sum_l |z_l|^2\right] \prod_{j < k} (z_j - z_k)^m, \quad (2.12)$$

where the complex variables $z_j = x + iy$ are functions of the j^{th} electron coordinates and $l_B = (\hbar c / eB)^{1/2}$ is the magnetic length.

This function significantly minimizes the Coulomb electron-electron interaction energy by placing m zeroes (vortices) in $\psi_m(z_i)$ at the location of all other ($j \neq i$) electrons, thus greatly reducing the probability of overlap between a given pair of electrons. Each vortex in $\psi_m(z_i)$ corresponds to an additional phase shift of 2π along a closed loop around the vortex, and thus can be associated with one magnetic

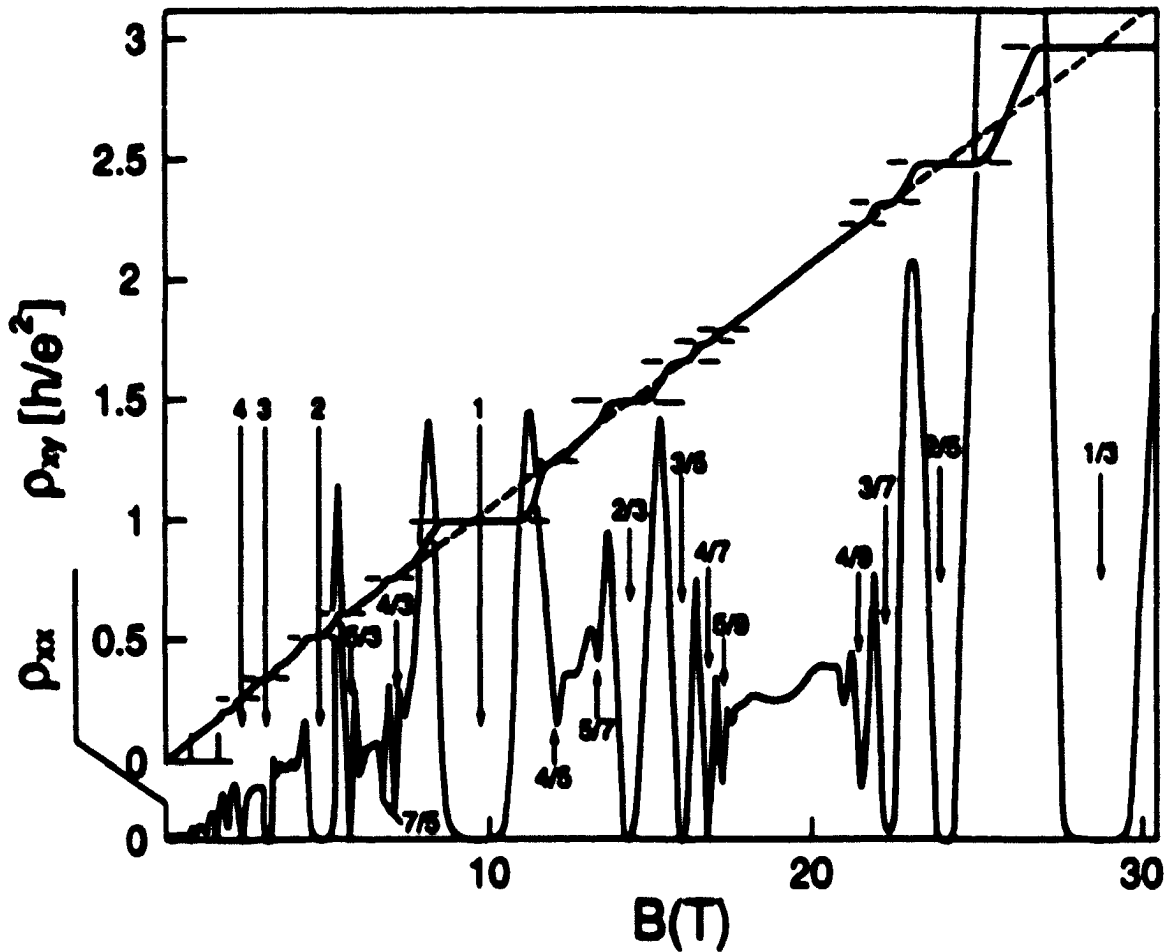


Figure 2.3: Overview of the observed fractions in the FQHE measurements. The dashed diagonal line represents the classical Hall resistivity (Eq. 2.3) and the solid curve with step-like structure (plateaus) the experimental results. Diagonal resistivity $\rho_{xx}(B)$ is drawn on a separate scale, with regions of $\rho_{xx} = 0$ (corresponding to the plateaus in $\rho_{xy}(B)$) and sharp spikes between some of them. The filling factors corresponding to each fraction are marked with arrows. Adapted from [12].

flux quantum. Placing m vortices on each electron translates into the filling factor $\nu = n/n_\phi = 1/m$. This suggests that the wave function in Eq. 2.12 will lead to a gap at $\nu = \frac{1}{m}$: adding or removing magnetic flux will create either free vortices or electrons having fewer than m flux quanta associated with them, at an extra energy cost.

Laughlin's "Corbino disk" argument can also be directly applied to his wave function ψ_m (Eq. 2.12), with a remarkable result: excitations associated with the free flux quanta or with the electrons lacking a vortex can be described as fractionally charged (e.g. $q = \frac{1}{m}$) quasiparticles and quasiholes [13, 14]. Indeed, such objects have been recently observed in the magnetic focusing [15] and shot-noise [16] experiments.

2.5 Spin in the Quantum Hall Effect

Although the existence of fractionally charged excitations has been by now experimentally established, the most basic questions about their key properties, such as effective mass, spin, and inter-particle interactions still remain to be answered theoretically and experimentally. For example, spin played no role in Laughlin's early description of the fractional quantum Hall effect, where he assumed that electrons are always fully polarized by a strong magnetic field for $0 < \nu < 1$.

Halperin was the first to point out [17] that this need not be the case in GaAs. The spin can be included in a Hamiltonian of a two dimensional electron system by considering the terms that correspond to the Coulomb electron-electron interaction and the Zeeman coupling of the electron spins to the external magnetic field:

$$\begin{aligned} \hat{H} = \int d^2r \left\{ \sum_n \frac{1}{2m^*} \left| \left(\mathbf{p} - \frac{r}{c} \mathbf{A} \right) \hat{\psi}_n(\mathbf{r}) \right|^2 - \kappa^* \mu_B \mathbf{B} \cdot \mathbf{S} \right\} + \\ + \frac{1}{2} \int d^2r \int d^2r' : [\hat{\rho}(\mathbf{r}) - \rho] V(\mathbf{r} - \mathbf{r}') [\hat{\rho}(\mathbf{r}') - \rho] : . \end{aligned} \quad (2.13)$$

where \mathbf{r} , \mathbf{p} , and \mathbf{A} are two-dimensional vectors in the (x, y) plane and $\nabla \times \mathbf{A} = \mathbf{B} = B\mathbf{e}_z$. Here $\hat{\psi}_n(\mathbf{r})$ and $\hat{\psi}_n^\dagger(\mathbf{r})$ are the fermion field operators, $\hat{\rho}(\mathbf{r}) = \sum_n \hat{\psi}_n^\dagger(\mathbf{r}) \hat{\psi}_n(\mathbf{r})$ and

$\mathbf{S}(\mathbf{r}) = \frac{1}{2} \sum_{\alpha, \beta} \hat{\Psi}_{\alpha}^{\dagger}(\mathbf{r}) \boldsymbol{\sigma}_{\alpha, \beta} \hat{\Psi}_{\beta}(\mathbf{r})$ are the electron density and spin density operators, and the colons $:$ denote a normal ordered product with respect to the fermion field operators. The first term describes the motion of spin- $\frac{1}{2}$ electrons in the perpendicular magnetic field (as in Equation 2.5), whereas the last term takes into account the Coulomb interaction between the electrons with the potential $V(\mathbf{r}-\mathbf{r}') = e^2/(\epsilon |\mathbf{r}-\mathbf{r}'|)$, assuming a constant background charge density ρ . For GaAs quantum wells, the dielectric constant is $\epsilon \approx 13$, and the effective electron mass and the effective g-factor are $m^* = 0.07 m_e$, and $g^* = -0.44$, where m_e is the bare electron mass in vacuum.

Defining the magnetic length to be $l_H = (\hbar c / e B)^{1/2}$ and using the numbers above, we can estimate that even in a 10 Tesla field the Zeeman energy of the conduction electrons⁴ ($E_Z = g^* \mu_B B \approx 3 \text{ K}$) is much smaller than both the Coulomb repulsion energy ($E_C = e^2 / \epsilon l_H \sim 175 \text{ K}$) and the cyclotron energy⁵ of similar magnitude (for the typical electron densities used). Therefore, the ground state of the total Hamiltonian may have some spins reversed, if the cost in Zeeman energy is outweighed by the gain in the Coulomb energy. The latter also depends on spin, since the total wavefunction (which includes both spatial and spin components) must satisfy Fermi statistics.

Similarly, the low-lying excited states of the system may have a total spin quantum number which is quite different from the spin of the ground state. Here we consider two types of excitations, neutral and charged, which are induced by increasing the temperature (e.g., spin waves) or by varying the filling factor (e.g. skyrmions) away from the $T=0$, $\nu=1$ fully polarized IQHE ground state. As Figure 2.4 shows, both the spin waves and the skyrmions cause a reduction in the total spin of the 2DES.

In a theory developed by S. L. Sondhi *et al* [18] and applied to $\nu = 1$ by H. A. Fertig *et al* [19], skyrmions are charged spin textures, described in terms of a smoothly

⁴Here all energies are in units of temperature (i.e. divided by the Boltzmann constant k_B).

⁵Given by the first term in Equation 2.9.

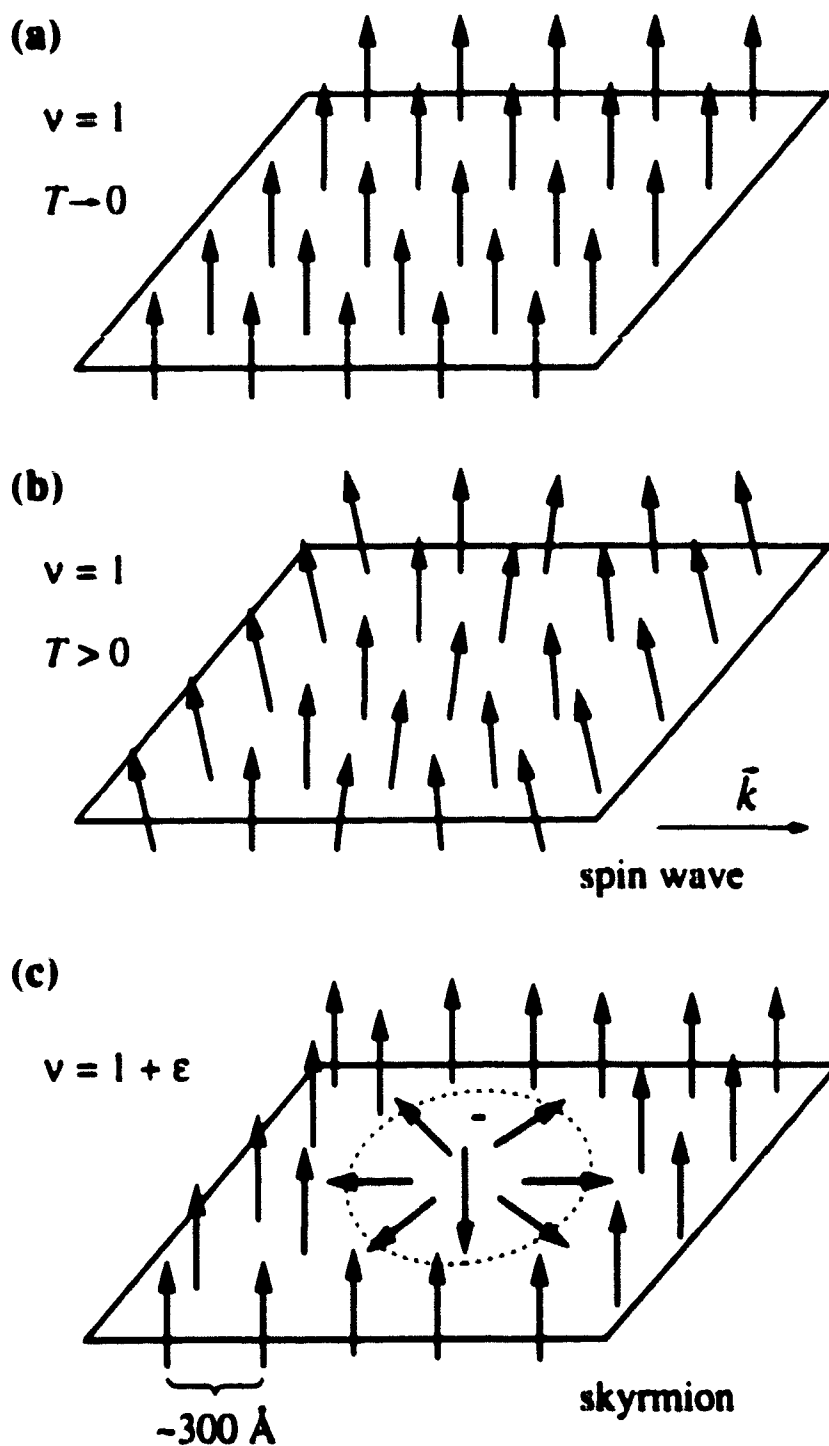


Figure 2.4: Schematic representations of a fully spin-polarized ground state (a), along with its neutral and charged excitations: (b) spin wave, and (c) spin texture called “skyrmion”.

varying unit vector field $\mathbf{m}(\mathbf{r})$. This defines the local spin orientation and gives the topological charge density via $\rho(\mathbf{r}) = (-\nu/8\pi)\epsilon_{\alpha\beta}\mathbf{m}(\mathbf{r}) \cdot [\partial_\alpha\mathbf{m}(\mathbf{r}) \times \partial_\beta\mathbf{m}(\mathbf{r})]$, with $\nu=1$ and an implicit summation over the two-dimensional coordinate indices α, β . The effective Hamiltonian is a functional of $\mathbf{m}(\mathbf{r})$ and can be approximated as:

$$E[\mathbf{m}] = \frac{\rho_s}{2} \int d^2r (\nabla\mathbf{m})^2 + \frac{\kappa^* \mu_B B}{4\pi l_H^2} \int d^2r [1 - m_z(\mathbf{r})] + \frac{e^2}{2\epsilon} \int d^2r \int d^2r' \frac{\rho(\mathbf{r})\rho(\mathbf{r}')}{|\mathbf{r} - \mathbf{r}'|}. \quad (2.14)$$

where $\rho_s = e^2/(16\sqrt{2}\pi\epsilon l_H)$ is the spin stiffness². The first term represents the Coulomb exchange energy cost, which in a two-dimensional case is independent of how large the spin texture is spatially. Instead, the effective size of the skyrmion is determined by a balance between the cost in Zeeman energy to flip additional spins (the second term in Eq. 2.14) and the benefit in Coulomb energy (the last term) of spreading the charge density over a wider area. This effective size can be parametrized by the amount of spin reversal, associated with each new unit of charge added to the system as the filling factor is changed, and thus can be measured experimentally.

The neutral excitations of a quantum Hall ferromagnet were considered by Y. A. Bychkov *et al.* [20] and C. Kallin and B. I. Halperin [21], who computed the dispersion relation for *spin waves* (I_0 is the modified Bessel function):

$$E(k) = \kappa^* \mu_B B + \frac{e^2}{\epsilon l_H} \sqrt{\frac{\pi}{2}} \left[1 - \exp\left(-\frac{k^2 l_H^2}{4}\right) I_0\left(-\frac{k^2 l_H^2}{4}\right) \right]. \quad (2.15)$$

This result, based on including both the direct and exchange Coulomb energies in addition to the Zeeman term, can be used to calculate the spin polarization of the $\nu = 1$ ground state as a function of temperature, yet another experimentally observable consequence of electron-electron interactions.

These advances in theory called for the development of novel spin-sensitive probes of the quantum Hall effect, as new testing grounds were needed to gain further insight into this rich macroscopic quantum phenomenon.

²Here ρ_s was not corrected for the finite quantum well thickness.

Chapter 3

Optically Pumped NMR: Background and Previous Results

3.1 Optical Pumping and Dynamic Polarization

Ever since the discovery of NMR by E. M. Purcell, H. C. Torrey, and R. V. Pound [22], the available NMR signal (and thus the smallest detectable sample size) has been a concern. A typical nuclear Zeeman splitting E_{Z_n} in a laboratory field of ~ 10 T is about 5 mK in temperature units, which means that even down to $T = 300$ mK the equilibrium distribution of nuclei among possible m_I states ($-I \leq m_I \leq I$) is close to uniform in the “hot” limit:

$$E_{Z_n} \equiv \hbar \gamma_n B \ll k_B T. \quad (3.1)$$

with the resulting nuclear polarization being very small:

$$\mathcal{P}_n \equiv \frac{\sum_{m_I} m_I \exp\left[\frac{\hbar \gamma_n m_I B}{k_B T}\right]}{\sum_{m_I} I \exp\left[\frac{\hbar \gamma_n m_I B}{k_B T}\right]} \approx \frac{1}{3} (I + 1) \frac{\hbar \gamma_n B}{k_B T} + O\left(\left[\frac{\hbar \gamma_n B}{k_B T}\right]^3\right). \quad (3.2)$$

In our case of $T = 300$ mK, $I = \frac{1}{2}$, and $\hbar \gamma_n B / k_B = 5$ mK, we only have $\mathcal{P}_n \approx 1.4 \times 10^{-2}$.

Since NMR experiment detects the net magnetization from N nuclear spins, $\langle M_z \rangle \propto N \mathcal{P}_n$.

the small polarization forces N to be large ($N > 10^{17}$). The “brute-force” approach of cooling the sample to boost its nuclear polarization (and thus NMR signal) is much more impractical than it might seem, since the longitudinal nuclear relaxation time (T_1) usually is prohibitively long (up to many hours in clean samples) at low temperatures. Thus, as the sample is cooled, the nuclear polarization lags behind other sub-systems, remaining much “hotter” than the lattice until the equilibrium is reached on the T_1 time scale. It is also necessary to wait for the nuclear magnetization to build-up after each $\pi/2$ tipping pulse, which effectively destroys $\langle M_z \rangle$.

This “conventional wisdom” was overturned in dramatic fashion by theorist A. W. Overhauser [8], who predicted in 1953 that up to a 1000-fold increase (compared to equilibrium) of the nuclear polarization can be achieved in a system of coupled electron and nuclear spins by saturating the electron spin resonance. Although greeted with great skepticism by the resonance community, his proposal was tested and upheld experimentally by T. R. Carver and C. P. Slichter [23], who were able to boost the polarization of ^7Li nuclei by a factor of 100 after irradiating the metal at the electron spin resonance frequency. The “Overhauser effect”, in its various guises, has gone on to be one of the most important and frequently used techniques in magnetic resonance.

G. Lampel was the first to observe similar effect in a solid by “optically-pumping” the electron system in pure silicon with a circularly polarized infra-red light in 1968 [24]. In his experiment he obtained an enormous increase in ^{29}Si signal by a factor of 15,000 in a very weak field of 1 G at 77 K. His seminal work led to the development of optically detected NMR techniques in GaAs [25].

All of these phenomena, collectively called “dynamic polarization”, arise from electron-nuclear spin-spin coupling, which can be represented by the $\mathbf{I}\cdot\mathbf{S}$ term in the Hamiltonian:

$$\mathcal{H} = \gamma_e \hbar B S_z + A \mathbf{I}\cdot\mathbf{S} - \gamma_n \hbar B I_z \approx \gamma_e \hbar B S_z + A I_z S_z - \gamma_n \hbar B I_z. \quad (3.3)$$

Irradiation of the sample repopulates the different m_x states, which changes the electron-nuclear relaxation rates away from their equilibrium values, leading to a build-up of large *non-equilibrium* polarization in the nuclear spin system. The spin-lattice relaxation rates in the electron and nuclear systems, however, differ by orders of magnitude, which makes it possible to detect nuclear hyperpolarization when the electrons have reached equilibrium, long after the irradiation of the electron system has stopped.

3.2 OPNMR Evidence for Skyrmions

Optical pumping was applied to GaAs quantum wells by R. Tycko and S. E. Barrett [9, 26, 27] in 1994–1995 to study spin physics of two-dimensional electron gas (2DES) in the quantum Hall regime. After detecting a signal [9] from the quantum wells, one of their first goals was to try to measure the electron spin polarization of the 2DES as a function of the filling factor and temperature near $\nu = 1$, which Prof. B. I. Halperin (Harvard) suggested was a good place to start.

The electron spin polarization may be obtained by measuring the Knight shift (K_x) of the quantum well nuclei, which is due to the same $\mathbf{I} \cdot \mathbf{S}$ Fermi contact hyperfine coupling term in Eq. 3.3 that is responsible for polarizing the nuclei during optical pumping.

Figure 3.1 (top) shows $K_x(\nu)$ data by S. E. Barrett *et al.* [26], which is in striking disagreement with the independent electron model described in Chapter 2, where the electron spins are assumed to be fully polarized in the partially filled first Landau level (i.e. at $\nu < 1$), while each electron introduced into the next available Landau level is spin-down, thus reducing the overall spin by 1, for $\nu > 1$ (solid line, Fig. 3.1 (top)).

Rather, these data suggest that electron-electron interactions lead to formation of

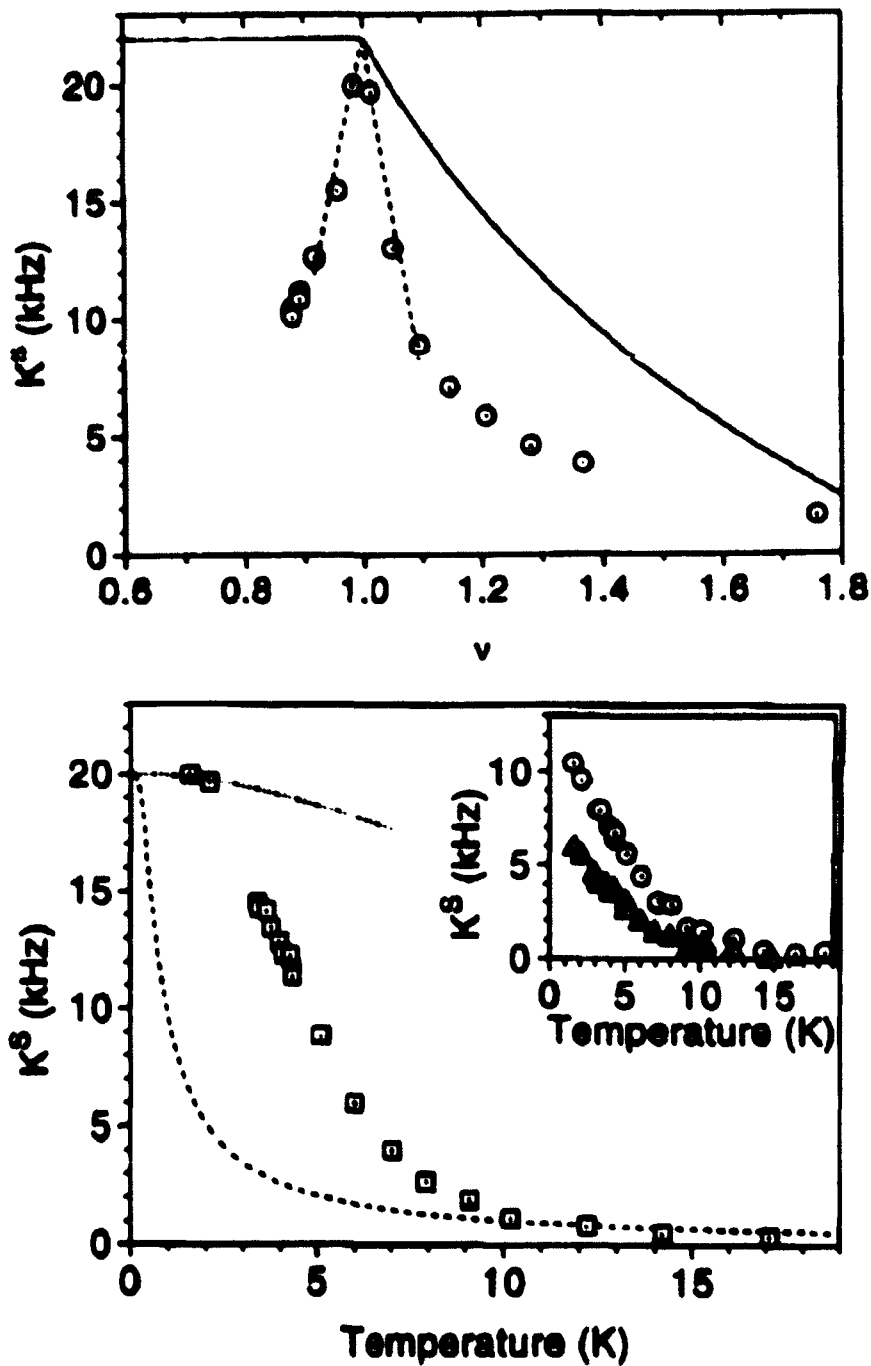


Figure 3.1: Top panel: Spin polarization plotted vs. filling factor ν and compared with both a single particle and Skyrminion-based model. The single-particle polarization is based on a simple counting argument, one spin flip per unpaired flux quantum for $\nu < 1$, and $S_z = 1$, for $\nu > 1$. Bottom panel: Electron spin polarization as a function of temperature at a filling factor close to $\nu = 1$. Reprinted from Barrett et al. [26].

charged spin textures at filling factors just below and just above $\nu = 1$. As charged excitations, the anti-skyrmions ($\nu < 1$) and skyrmions ($\nu > 1$) are apparently energetically more favorable compared to the isolated holes and spin-flipped electrons respectively, which results in a significant amount of spin reversal per unit charge, parametrized by $\dot{A} \approx \dot{S} \approx 3$ spin flips per anti-skyrmion or skyrmion. It is the presence of these quasiparticles that is believed to be responsible for the dramatic depolarization of the 2DES observed by S. E. Barrett *et al.* on either side of $\nu = 1$. These findings were subsequently confirmed by magnetoabsorption spectroscopy measurements of electron spin polarization by E. H. Aifer *et al.* [28] and M. J. Manfra *et al.* [29] in the neighborhood of $\nu = 1$, whereas the transport measurements right at $\nu = 1$ supported the existence of skyrmion anti-skyrmion pairs [30, 31].

The Knight shift temperature dependence data at $\nu = 1$ (Figure 3.1 (bottom)) probe the neutral spin-flip excitations which can be identified as thermally-excited spin-waves in the theoretical approaches of N. Read and S. Sachdev [32], M. Kasner and A. H. MacDonald [33], and other groups [34]. Electron-electron interactions are important here, since the data clearly does not fit the non-interacting model (dashed line, Fig. 3.1 (bottom)).

The exceptional ability of OPNMR to directly probe the electron spin degree of freedom makes this technique a tool of choice to study electron-electron interactions. Due to the fermionic nature of electrons these interactions strongly depend on the spin variable and thus are revealed in spin-sensitive measurements. This idea was at the basis of our motivation to use OPNMR in the study of the fractional quantum Hall effect, a phenomenon that exists only because of strong electron-electron interactions. Furthermore, both $\nu = 1$ and $\nu = 1/3$ ground states are expected to be fully spin-polarized, so we were interested in comparing the behavior of these primary integer and fractional quantum Hall ferromagnets.

3.3 Recent Applications of Optical Pumping beyond GaAs

In this section we review some of the latest work using optically pumped NMR by various research groups.

C. A. Michal and R. Tycko used optical pumping of InP to study polarization transfer between different nuclear species [35]. They found that ^{31}P nuclei, which are spin one-half, couple to the optically pumped polarization of ^{115}In in an unusual way. This causes the ^{31}P signal to develop very slowly (on the time scale of milliseconds) during a weak NMR tipping pulse, independently of the initial ^{31}P polarization. The contribution of indium to this effect was established directly in a separate measurement by applying a tipping pulse at the ^{115}In frequency, which modulates the evolution of ^{31}P signal. The exact mechanism of this coupling is not well understood, and the question of its existence in other semiconductor systems remains open (for instance, we have not seen it in our GaAs experiments).

In another development, T. Pietraß and M. Tomaselli established the possibility of optical pumping in CdS [36]. They report achievement of a factor of ~ 2 increase in ^{113}Cd polarization at a temperature of $T = 2\text{ K}$ after pumping the interband transitions in single crystals with a blue-green laser light. This increase is still significant since at that temperature the nuclear relaxation times are on the order of 2 hours, while the optical pumping is reported to boost ^{113}Cd NMR signal in about 10 minutes.

The reader is further referred to Chapter 7, where we describe our initial attempts to study epitaxial layers of GaN, a wide bandgap semiconductor with a uniaxially symmetric wurtzite crystal structure.

Chapter 4

Experimental Set-Up

4.1 Multiple Quantum Well Samples

The Quantum Hall effect study reported in this thesis would not be possible without samples of unprecedented quality, grown by Loren Pfeiffer and Kenneth West at Bell Laboratories. The samples are in many ways unique, as pieces from the same wafer provide new data for successive generations of experimentalists, in different research groups around the world.

We used two different electron-doped GaAs multiple quantum well (MQW) samples to study electron spins near the Landau filling factor $\nu = \frac{1}{3}$. Both samples, labeled 10W and 40W according to the number of quantum wells, were grown by molecular beam epitaxy on semi-insulating GaAs(001) substrates. The vital dimensions of the MQW structures for both samples can be found in Table 4.1.

Figure 4.1 shows a general schematic of the MQW structure, common to both samples, and the corresponding energy band diagram. The evenly spaced GaAs quantum wells are separated from each other by much wider $\text{Al}_{0.1}\text{Ga}_{0.9}\text{As}$ barriers. Silicon delta-doping spikes located in the center of each barrier provide the electrons that become confined in each GaAs well at low temperatures, producing 2DES with

Table 4.1: Dimensions and other parameters of the GaAs samples.

Parameter	(units)	Sample 40W	Sample 10W
Growth ID number		3 5 93.4	10 10 91.1
Quantum Well width, w	(Å)	300	260 *
Quantum Well material		GaAs	GaAs
Barrier width	(Å)	3600	3120 *
Barrier material		$\text{Al}_{0.1}\text{Ga}_{0.9}\text{As}$	$\text{Al}_{0.1}\text{Ga}_{0.9}\text{As}$
Number of identical layers		40	10
Substrate width	(mm)	0.5	0.5
Substrate material		GaAs (001)	GaAs (001)
Two-dimensional area	(mm ²)	6 × 5	6 × 4
Electron density, n	(cm ⁻³)	$(6.69 \pm 0.03) \times 10^{10}$	$(7.75 \pm 0.04) \times 10^{10}$
Field, at which $\nu=1$	(T)	2.76	3.20
Max. ⁷¹ Ga Knight shift	(kHz)	9.03	11.79
Electron mobility, μ	($\frac{\text{cm}^2}{\text{Vs}}$)	$> 1.4 \times 10^6$	$> 1.4 \times 10^6$

* These numbers were scaled down from their nominal as-grown values by 13.3% to make the Knight shift and the electron density self-consistent. The explanation for this reduction is that sample 10W was grown without wafer rotation, which could have led to a uniform gradient in the Ga flux, and thus the width of all layers, across a 2-inch substrate [37].

very high electron mobility ($\mu > 1.4 \times 10^6 \text{ cm}^2/\text{Vs}$). This MQW structure also results in a 2D electron density that is unusually insensitive to light, and extremely uniform from well to well [38].

Before studying the samples with NMR, we soaked them in 0.1 M solution of HCl

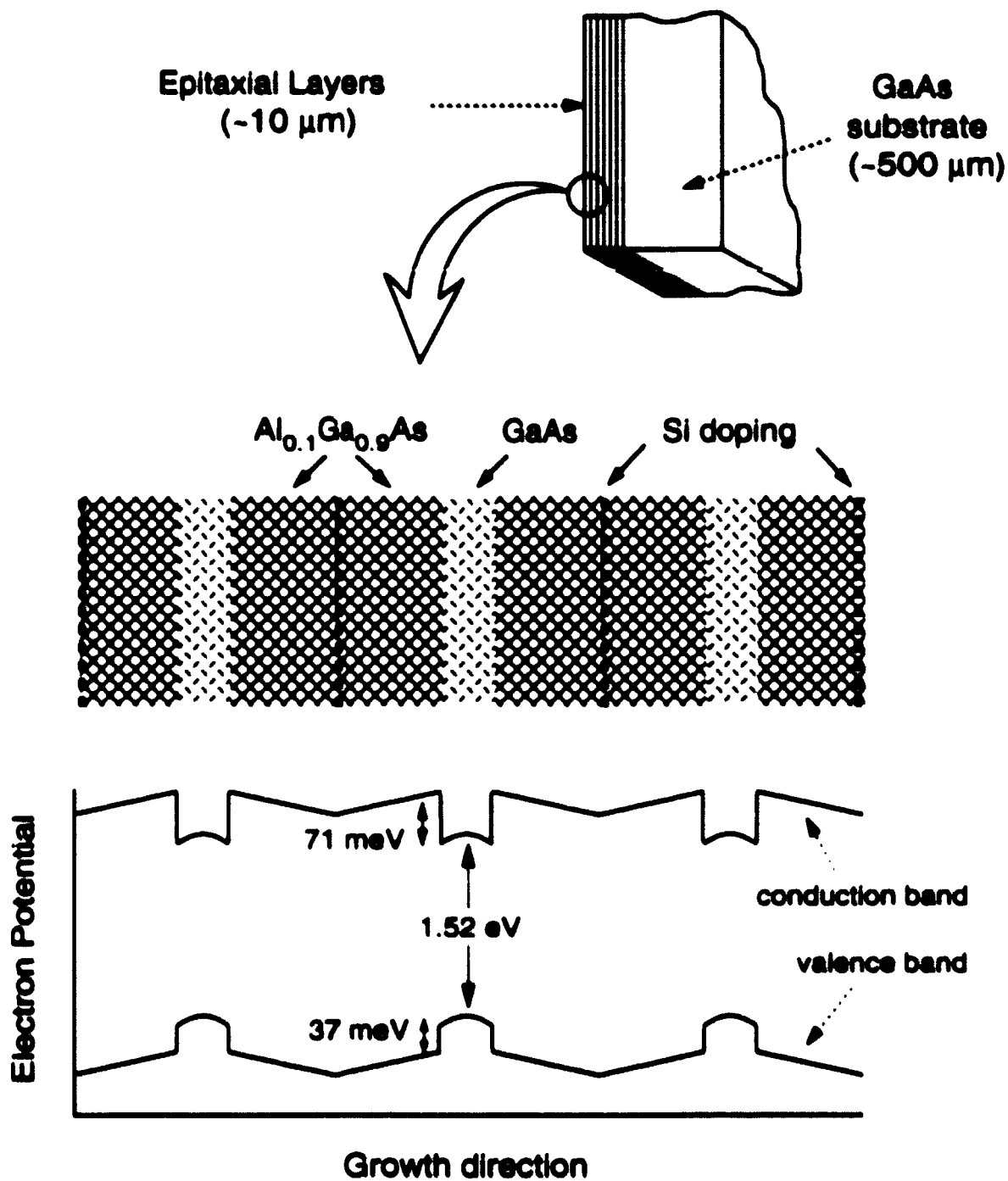


Figure 4.1: Schematic diagram of a quantum well sample, with the epitaxial layer structure and the corresponding electron energy bands shown as a function of the spatial coordinate z' along the growth direction.

over ~ 24 hours, to remove any Ga metal that was used to attach the substrate to the growth stage.

4.2 Tilted Field Approach: The Swedish Rotator

In any experimental study of the Quantum Hall effect it is important to be able to control the two primary thermodynamic quantities, namely the Landau level filling factor ν and the sample temperature T . While postponing the discussion of temperature control till section 4.5, we will focus here on controlling the filling factor $\nu = n/n_\phi = (nhc)/(eB_\perp)$ in our experiment. Here n is the two-dimensional electron density in the quantum well, $n_\phi = (eB_\perp)/(hc)$ is the density of magnetic field flux quanta penetrating the plane of the well, whereas e , h , and c are the elementary charge, the Planck's constant, and the speed of light, and B_\perp is the component of magnetic field perpendicular to the quantum well.

Our samples are grown without any gates that could allow us to vary the electron density n . On the contrary, both samples exhibit a remarkable reproducibility of n from cool-down to cool-down, as well as no detectable sensitivity to illumination by light. Thus the only control parameter with which one can manipulate the filling factor ν in the experiment is the perpendicular magnetic field B_\perp .

Now we are down to two possibilities: (a) we can sweep the total magnetic field B_{tot} , as is done in many magneto-transport and optical experiments, or (b) we can keep B_{tot} constant, and change the angle θ between \vec{B}_{tot} and the sample's growth direction \vec{z} , thereby changing the perpendicular field $B_\perp = B_{\text{tot}} \cos \theta$, and thus the filling factor $\nu = (nhc)/(eB_{\text{tot}} \cos \theta)$.

In practice, changing B_{tot} in an NMR system involves careful shimming of the magnet to achieve ~ 1 part per million (ppm) field homogeneity over the macroscopic volume of the sample (see section 4.3.1). This time-consuming and laborious pro-

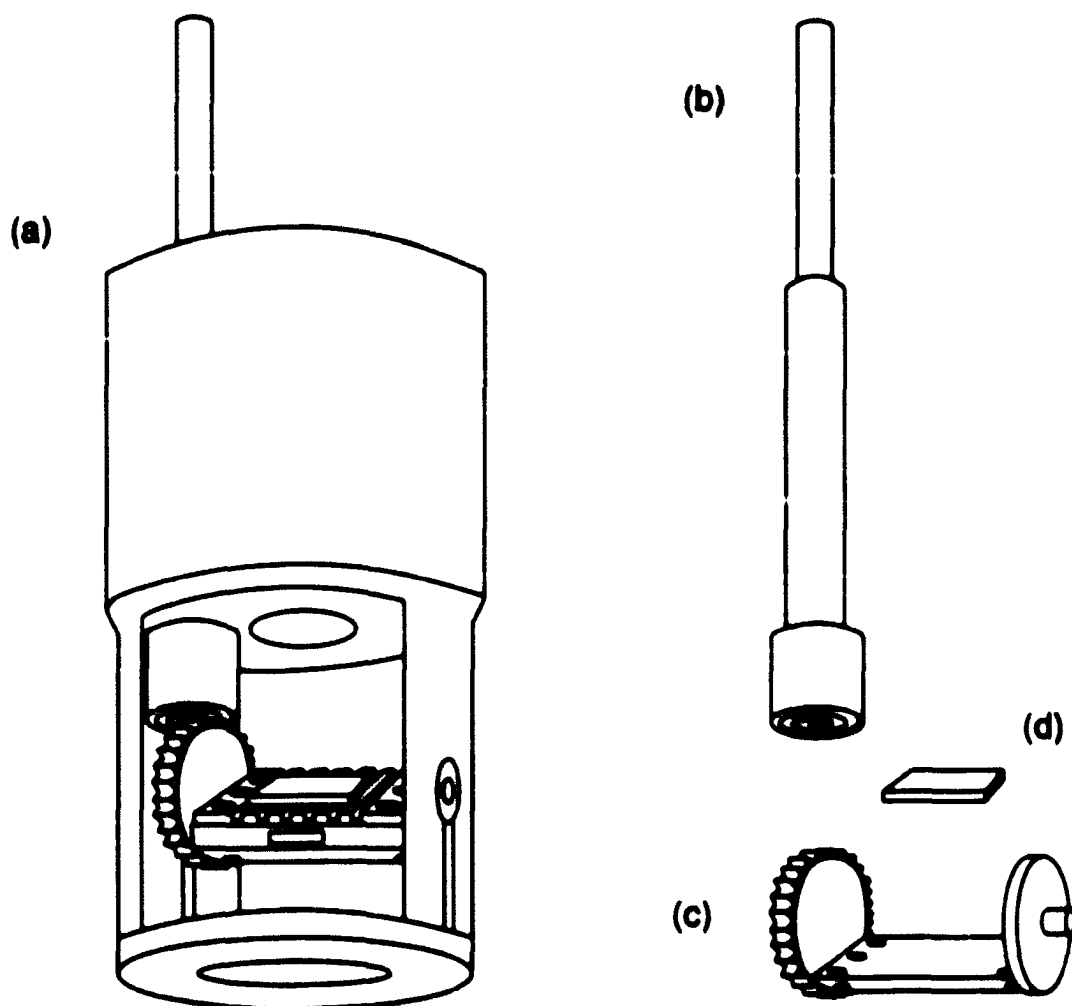


Figure 4.2: (a) Swedish rotator assembly, with (b) the spiral, (c) rotator platform, and (d) the sample shown separately, offset from one another for clarity. The rotator housing, the spiral, and the rotator platform are all made of brass to avoid differential contraction at low temperatures. In (a), note the grooved sapphire support under the sample and the hole cut through the rotator housing above the sample to allow the collimated light beam from the optical assembly (not shown here).

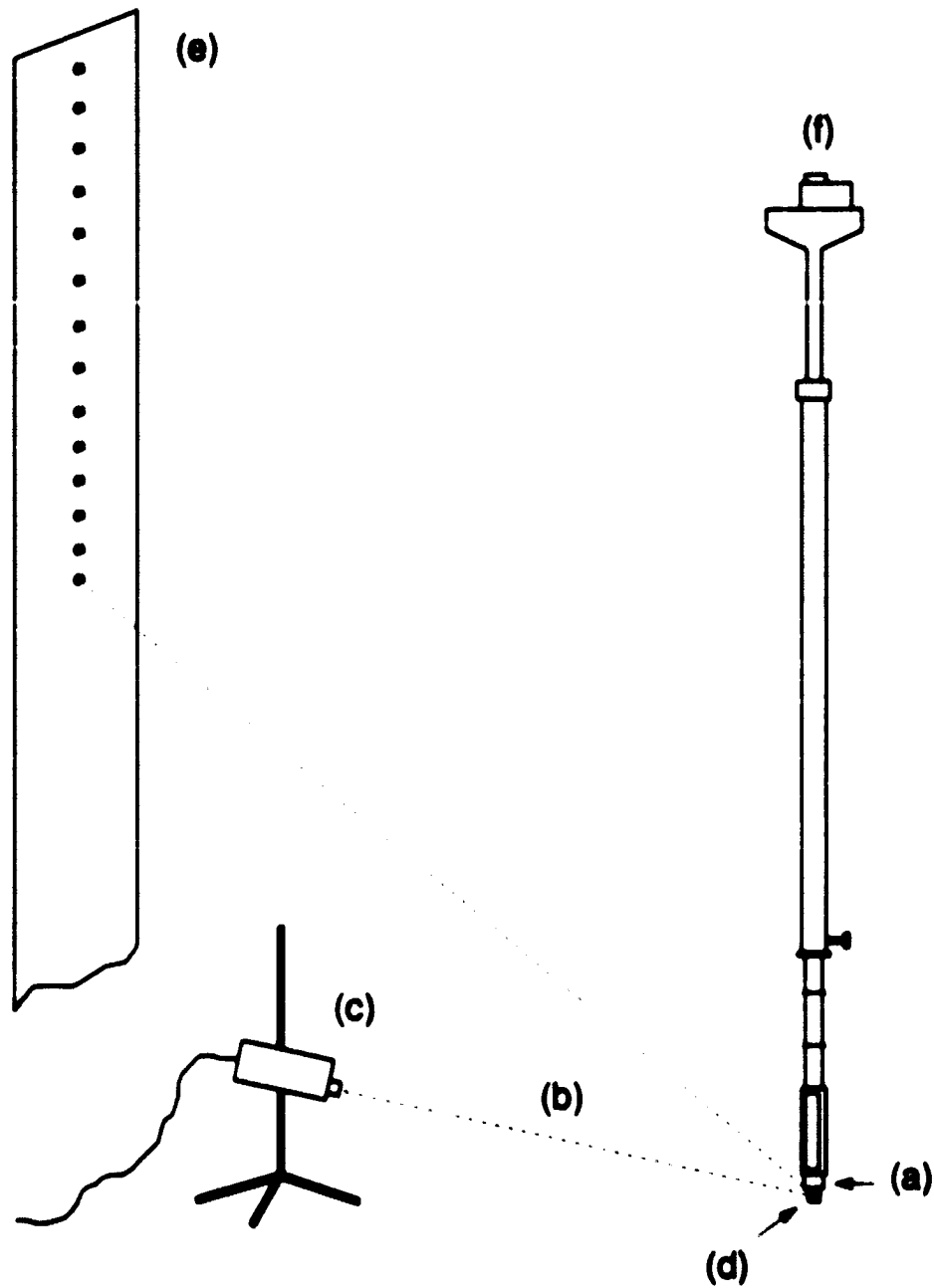


Figure 4.3: Set-up used for testing (a) the Swedish rotator, where (b) beam from (c) a 1 mW He-Ne laser was directed at (d) the mirror-like sample surface and reflected onto (e) a screen some distance away. Advancing (f) the rotator knob on top of the probe by $\Delta\theta = (20 \text{ divisions of the counter})$ at a time, the light spots on the screen were marked off with a pen. In case of a "perfect" rotator, we expect the marks to be distributed following a simple $\tan 2\theta$ law.

cedure makes choice (a) rather unrealistic when it comes to taking NMR data as a function of the filling factor ν . Instead, we adopted the "tilted field" approach (b), where the sample can be rotated *in situ* without stopping the low-temperature experiment.

Figure 4.2 shows the key elements of the "Swedish rotator", purchased from Oxford Instruments as part of the cryostat probe. The idea behind it is to save space in the congested radial dimension by placing the spiral (b) above rather than to the side of the gear-wheel (c). This arrangement, however, requires the fit between the housing (a), the spiral, and the gear-wheel to be made to much tighter tolerances compared, for example, to a simpler "worm-gear" design. This can be easily seen, since a small horizontal displacement of the spiral will immediately translate into a change in θ , whereas the "worm-gear" design is only sensitive to the vertical tolerances that are relatively easy to control.

Our experimental objective was to achieve an angular accuracy of $\pm 0.1^\circ$ over the wide range of angles ($-60^\circ < \theta < 60^\circ$). Figure 4.3 shows a simple set-up that we used to test the accuracy of the Swedish rotator. Initial testing uncovered two principal difficulties in the original Oxford design: (i) the deviations of the measured θ from the dialed-in values were $\pm 2.5^\circ$, and (ii) the spiral and the rotator housing were manufactured from different materials (plastic and brass, correspondingly), which would make it impossible to test the rotator at room temperature and guarantee its performance in a cryogenic environment due to significant differential contraction of rotator parts.

To alleviate both of these problems, the spiral was remachined from the same material (brass) as the housing, with tolerances of $\sim 10\ \mu\text{m}$. The detailed shape of the grooves had to be calculated to mesh exactly with the teeth of an existing gear-wheel, and a special cutting tool had to be ground to impart that shape onto the spiral. After numerous trials and errors the spiral of the right shape was made in

three copies.

At that point we found that a combination of pieces made of the same material with very tight tolerances leads, after a number of revolutions, to a critical build-up of burrs at the contact points of the rotating parts, suddenly causing the mechanism to lock-up. Using a dry lubricant ($0.7\ \mu\text{m}$ MoS_2 powder) extended the “mean time to jam” of the rotator to tens of revolutions. Finally, we treated all moving parts of the Swedish rotator with the “Dichronite” surface coating, provided by a company in Massachusetts.

Combined with MoS_2 , this treatment resulted in two years of flawless operation, after which occasional jams still took place. Over that time, the accuracy of the Swedish rotator degraded somewhat from $\pm 0.04^\circ$ to $\pm 0.1^\circ$ over the range $-25^\circ < \theta < 60^\circ$, as was estimated from testing shown in Fig. 4.3, and later confirmed by Al NMR measurements of electric quadrupole shifts in single crystal Al_2O_3 (see Appendix B for details).

4.3 NMR Techniques

4.3.1 Superconducting Magnet: Preparing the Field

All measurements described in this thesis were performed in an Oxford Instruments 89 mm/12 T *Trislatron*[®] magnet, which was operated in the persistent current mode during the experiments. Bringing the magnet to a new field involved a number of subtle points, ranging from safety precautions to measures necessary to achieve stable, spatially homogeneous magnetic field.

Prior to a field change, the desired range of frequencies for the given nucleus was scanned with an NMR probe taken out of the cryostat, to detect any FM radio stations that could interfere with NMR signals. A “quiet spot” in the spectrum was

picked, and the exact value of the field calculated. The magnet current leads were then attached and the field change would begin.

After some trials and errors we found that the magnet settles¹ at a new field much faster, if it is first brought to zero, then energized to a new value with an overshoot of ~ 0.017 T, and finally brought to the required field after a ~ 15 min wait. This procedure allowed us to achieve drifts of less than 0.1 ppm/hour in 24 hours after going into persistent mode. For comparison, typical drifts measured several months later would be on the order of 0.005 ppm/hour.

During the field change, attention needed to be paid to ensure proper electrical grounding in case of a quench; it also proved absolutely vital to have the superconducting shim power supply automatically "dump" the shim coils, thus letting any magnetic flux trapped in them out.

Once the temporal stability of the field was checked by monitoring a D₂O NMR signal overnight, the magnet was shimmed to straighten the field spatially. A set of six superconducting shim coils² was used to achieve a ~ 0.2 ppm magnetic field homogeneity over the sample volume. Shimming was done with a ~ 1 mm³ droplet of D₂O inside a capillary mounted in a shimming probe that was built for that purpose. The probe allowed precision positioning of the droplet within the sample space in the vacuum-tight ³He volume of the cryostat. Using this probe, magnetic field was mapped with deuterium NMR signal and the gradients $\frac{\partial}{\partial x}$, $\frac{\partial^2}{\partial x^2}$, $\frac{\partial}{\partial z}$, $\frac{\partial}{\partial y}$, $\frac{\partial^2}{\partial x \partial y}$, and

¹Once in the persistent mode, the magnet's field can drift due to (a) various transient "memory" effects, (b) flux leakage through the joints in the superconducting wiring, and (c) pressure fluctuations above the helium bath. Little can be done about (b), a manostat on the He exhaust will fix (c), but (a) depends crucially on how the magnet was energized. It is not uncommon for a magnet to drift upwards for days, when brought from high field to a lower value improperly.

²A complete second-order shim set would also include two more coils to handle $\frac{\partial^2}{\partial x^2}$ and $\frac{\partial^2}{\partial z^2}$ field gradients.

$\frac{\partial^2}{\partial x^2} \cdot \frac{\partial^2}{\partial y^2}$, corresponding to the magnet's installed shim coils, were zeroed by adjusting shim currents in the coils. Typically, shimming would take several hours and cost several liters of liquid helium due to an increased boil-off when the current leads are attached.

4.3.2 Home-Built NMR Spectrometer, Pulse Generation

The experiments were carried out using a home-built NMR spectrometer, based on a TecMag *Aries* pulse programming and data acquisition unit (Figure 4.4). The spectrometer was designed to cover the radiofrequency (rf) range of 10 to 165 MHz, in order to accommodate most nuclei of interest (Table 4.2) in the magnetic fields up to 12 Tesla.

A software package (*MacNMR*, part of the TecMag module) allowed one to lay out any pulse sequence of up to 128 steps, and cycle through it as long as practically reasonable, up to several days, with a possibility of changing parameters from cycle to cycle using "tables" instead of single values for any parameter. The duration of each step could be set to up to 210s in multiples of $0.1 \mu\text{s}$, with the exception of data acquisition points, that had to be spaced by at least $1 \mu\text{s}$ from each other, which translates into having a full 1 MHz frequency window anywhere in the rf range of the spectrometer.

For each step in the pulse sequence, binary outputs could be set independently on 20 fast TTL logic [39] lines, which could be connected through a fan-out box (Fig. 4.4) to external devices (such as rf gates¹) to produce rf pulses, to operate an optical shutter, thus forming light pulses, or to switch the frequency synthesizer phase

¹A set of gate drivers was built to convert TTL logic signals into $\pm 20 \text{ mA}$ current pulses necessary to operate S1 gates. Each driver was monitored by a home-made protection circuit, which would block both long and high duty-cycle pulses from reaching the power amplifier.

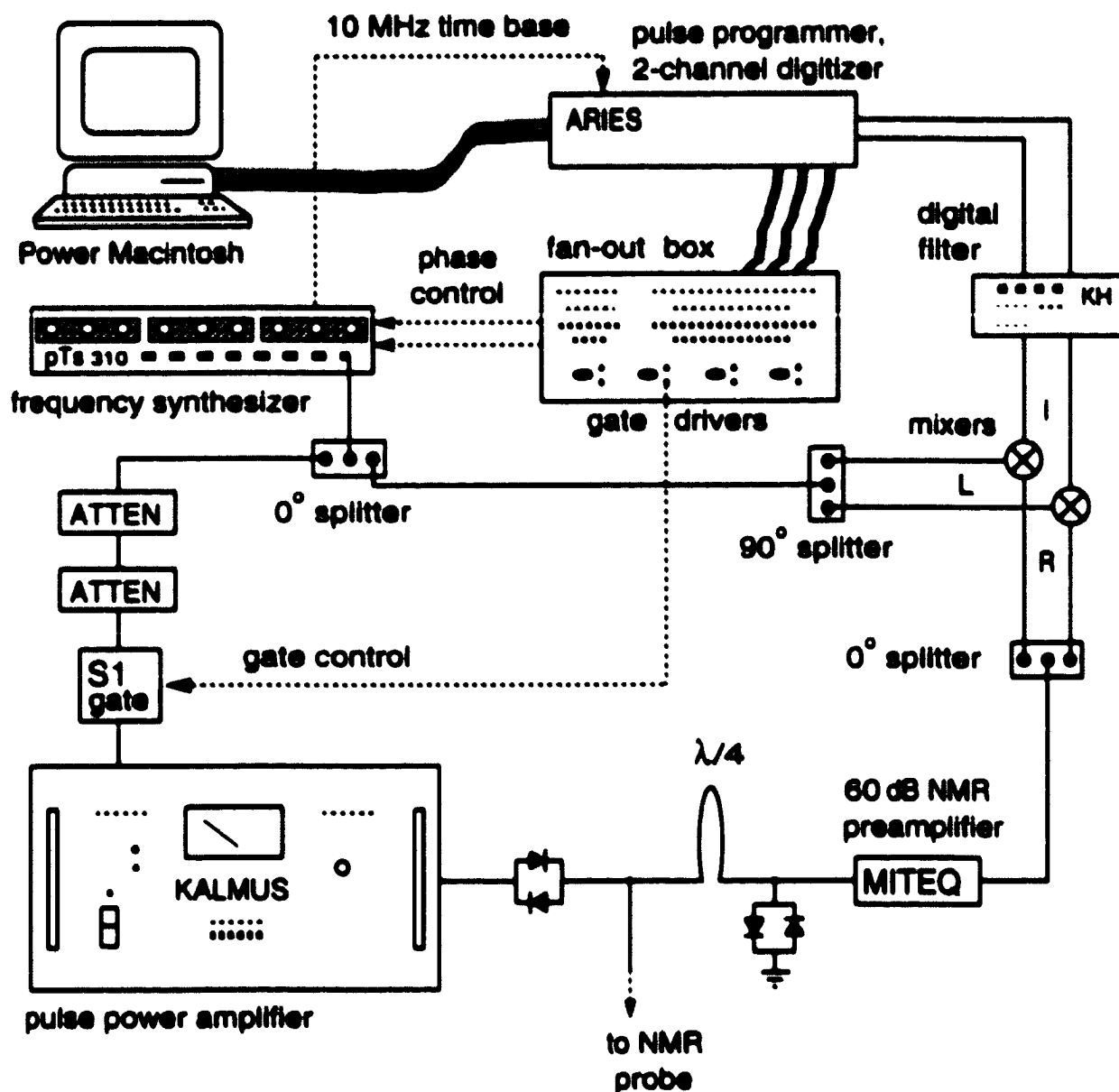


Figure 4.4: Schematic diagram of the home-built radio frequency spectrometer, used in all NMR/OPNMR measurements reported in this thesis. The transmitter (bottom-left corner) produces up to 1 kW of output pulse power in the 10–160 MHz range, with less than a 100 ns response time. The receiver circuit (right, bottom to top) has up to 100 dB of total gain and includes a quadrature detector, followed by a 2-channel digital low-pass filter and a 2-channel A/D converter with the 1 MHz acquisition rate. Also shown is a standard NMR frequency synthesizer with an oven-controlled temperature-stabilized oscillator, which provides the time base for the experiment, and is a frequency source for the transmitter and the mixers in the receiver circuit

Table 4.2: Gyromagnetic ratios and various NMR data for some nuclei of interest.

Property	(units)	^{71}Ga	^{69}Ga	^{75}As	^{27}Al	^{115}In	^{113}In	^2D
Nuclear spin	I	$\frac{3}{2}$	$\frac{3}{2}$	$\frac{3}{2}$	$\frac{5}{2}$	$\frac{9}{2}$	$\frac{9}{2}$	1
Natural abundance	(%)	39.9	60.1	100	100	95.7	4.3	0.015
Gyromagnetic ratio	$\frac{\gamma_n}{2\pi}$ ($\frac{\text{MHz}}{T}$)	13.00	10.23	7.30	11.09	9.34	9.32	6.54
12 T frequency	(MHz)	155.9	122.7	87.6	133.1	112.1	111.9	78.5
El. quadrup. moment	Q (10^{-4} A^2)	0.11	0.17	0.31	0.15	0.81	0.80	0.003

in multiples⁴ of 90° , as needed for the CYCLOPS sequence [40], to simultaneously cancel any phase imbalance or voltage offsets in both data acquisition channels. Once loaded into the pulse programmer, the pulse sequence was executed independently from the computer, using a 10 MHz frequency standard from the synthesizer as a time base.

The rf pulses (typically 1 to 20 μs long) were formed in the transmitter part of the spectrometer by chopping an rf sine wave, coming from the synthesizer, with a fast ($\sim 7 \text{ ns}$ switching time) S1 gate, and then amplified in the Kalnus power amplifier up to 200 W (or about 280 V peak-to-peak (Vpp) into the 50 Ω line). These high voltage

⁴By using other available control lines it would be possible to change the phase of PTS synthesizer in multiples of 0.225° , beyond what is normally needed for a standard CYCLOPS sequence.

rf pulses with a square envelope were then sent down a semirigid coaxial cable to the resonant tank circuit inside the cryostat.

4.3.3 NMR Tank Circuits, Power Handling

Depending on the frequency, we used one of the two simple circuits, shown in Figure 4.5. By varying capacitances C_1 and C_m , a given circuit was tuned to resonate at the required rf frequency and at the same time its reflected power was minimized to be below 1% (20 dB) of the incident rf power [41]. Under those conditions a typical quality factor Q was about 100. This value was close to optimal, balancing frequency selectivity ($\propto Q$) with the decay rate of the circuit ring-down ($\propto Q^{-1}$). A usual width Δf of the tank circuit resonance was ~ 1 MHz, while the ring-down decayed to the noise level of our preamplifier in $\sim 10 \mu\text{s}$ after the pulse.

As in many other solid-state NMR experiments that involve broad lines, excitation pulse power was at a premium³ in our measurements, limited severely by arcing in strong magnetic fields in the low-pressure helium gas atmosphere [42]. Usual precautions were taken to avoid pointy spikes of solder; wires were varnished and capacitors were wrapped with mylar film to minimize contact with the helium gas that would cause sparks due to its low threshold to electrical break-down. The process of detection and elimination of the trouble spots was carried out using a transparent hermetically sealed vessel that was adapted to be fitted around our NMR probe, filled with low-pressure helium, and inspected for sparking in complete darkness as the pulses were sent on into the circuit. In each of our NMR experiments later, the reflected power from the probe was monitored through a 40 dB Bird directional

³The rf magnetic field amplitude H_1 during the pulse of length τ_{pulse} defines the tipping angle for the nuclear spins, $\alpha = \frac{1}{2} \gamma_n H_1 \tau_{\text{pulse}}$, where γ_n is the nuclear gyromagnetic ratio (Table 4.2). Usually α is fixed (e.g. $\alpha = \pi/2$), while τ_{pulse}^{-1} is made much greater than the desired spectral width to avoid non-uniform excitation. For this reason stronger pulses are needed to measure broad NMR lines.

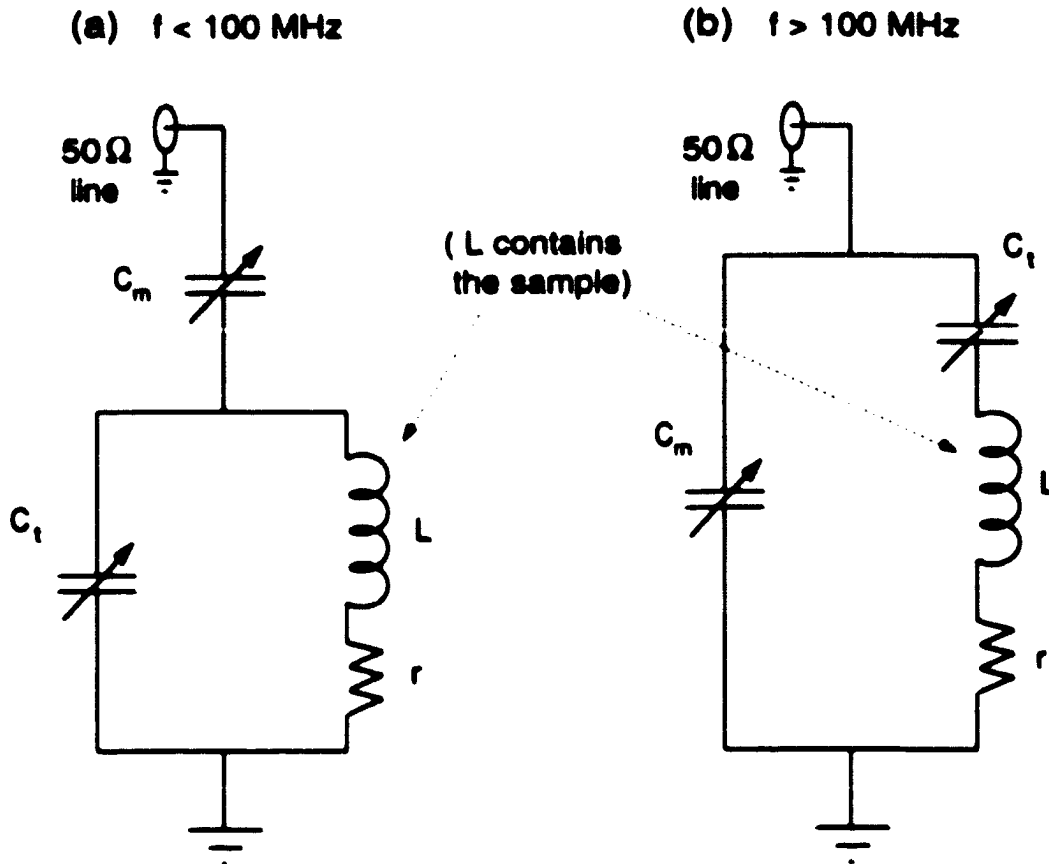


Figure 4.5: Series-parallel (a) and parallel-series (b) resonant tank circuits used in our NMR probe. For a typical 6-turn copper coil and the 2 25 pF variable capacitors that could fit into our limited probe space, it was advantageous to use “b” as opposed to “a” above ~ 100 MHz. Most of the time the variable capacitors shown had to be supplemented by the fixed capacitors in the 1 120 pF range, in order to simultaneously tune the circuit at a given frequency $f = \omega/(2\pi)$ and match it to the $50\ \Omega$ coaxial line impedance. The total values C_t and C_m needed for the tuning and the matching capacitances, respectively, can be calculated using the formulae:

$$(a) \quad C_t = \frac{L\omega - \sqrt{r/50\Omega} \sqrt{r^2 - (50\Omega)r + L^2\omega^2}}{\omega(r^2 + L^2\omega^2)} \quad ; \quad C_m = \frac{\sqrt{r/50\Omega}}{\omega \sqrt{r^2 - (50\Omega)r + L^2\omega^2}}$$

$$(b) \quad C_t = \frac{L\omega + \sqrt{(50\Omega - r)r}}{\omega(r^2 - (50\Omega)r + L^2\omega^2)} \quad ; \quad C_m = \frac{\sqrt{(50\Omega/r) - 1}}{\omega(50\Omega)}$$

where the effective resistance r (on the order of a few ohm) reflects total losses in the circuit. The value of r is frequency- and temperature-dependent.

coupler using a Tektronix digital oscilloscope, so that arcing could be easily observed when it happened as it distorted the envelope of the reflected rf pulse [41]. As a result of these efforts, 15 W power levels (77 V_{pp} into 50 Ω) were achieved at low ³He temperatures⁶ without arcing, with corresponding ⁷¹Ga 90° tipping times⁷ being 7 μs for $H_1 \approx 55$ G.

4.3.4 Quadrature Detection and Signal Processing

Throughout all experiments described in this thesis quadrature detection [41] was used, which effectively allows one to record both x and y components of the precessing nuclear magnetization (referenced to the frame rotating with the frequency of the synthesizer) into two data acquisition channels, commonly called “real” and “imaginary”. This was accomplished by splitting the output of the 60 dB Miteq preamplifier into two identical in-phase signals (with a two-way 0° Mircircuits splitter/combiner) and mixing them with a pair of pure sine waves at the synthesizer frequency, one of which was delayed in phase by 90° (Mircircuits level 7 mixers and a two-way 90° splitter/combiner of the proper frequency range were used as shown in Fig. 4.4).

The output “I” (intermediate frequency) signals from the mixers were then further amplified, low-pass filtered, and amplified again using a two-channel Krohn-Hite digital filter. The filter was operated in the “Butterworth” mode (4-pole, or 24 dB/octave attenuation in the rejection band) and its cut-off frequency was set to $f_c = \frac{1}{2} \tau_{\text{acq}}^{-1}$, where τ_{acq}^{-1} denotes the data acquisition rate⁸ for each channel. The resulting group

⁶Measurements in a ³He bucket cryostat presented no arcing problems (up to 100 W), since for the most part of the experiment (up to 5.5 hours at 1.5 K) the tank circuit was completely immersed in liquid helium which has a much higher breakdown threshold than the gas.

⁷Note that only $\frac{1}{2} H_1$ is involved in tipping the nuclear spins.

⁸Usually the data were acquired at a rate of 100 or 200 kHz for Ga (depending on the sample), and 1 MHz for Al in sapphire.

delay [43] for both signals was $\tau_{\text{delay}} = \frac{149.7^\circ}{360^\circ} f_c^{-1}$, where 149.7° is the phase slope per Hz of a Butterworth filter. Finally the voltages in both channels were digitized and stored as a function of time in a TecMag data acquisition module, averaged over multiple NMR “scans” to boost signal to noise if necessary, and dumped into computer memory for further processing.

To obtain a spectrum $I(f)$ from the recorded free induction decay of magnetization $M_z(t)$, digital data processing was used [41]. Typically, it involved (i) base line adjustment to suppress constant voltage offsets; (ii) gaussian broadening of 0.5 kHz full width at half maximum (FWHM) to reject long-lasting harmonic noises; (iii) complex fast Fourier transform (FFT); (iv) phase 1 correction to compensate for missing first data-points, filter group delay, etc.; and (v) phase 0 correction to compensate for the cable length plus an unknown phase shift in the impedance-matched tank circuit. If any distortion still remained in the base line due to persistent ring-down or otherwise corrupted first few data points in the time domain, (vi) low-order harmonics were fitted to the base line in the frequency domain and were then subtracted off to avoid shifting of an apparent peak position due to underlying slope in the base line.

4.3.5 OPNMR Timing Sequence

The basic OPNMR timing sequence that was routinely used with the GaAs quantum well samples is shown in Figure 4.6(a).

At the low temperatures nuclear relaxation times can be extremely long (up to several hours), making nuclear polarization essentially history-dependent, and the nuclear equilibrium (Fig. 4.6(b)) hard to reach quickly. To avoid this complication, the sequence always starts with a saturation pulse train, which repeatedly (up to 60 times) tips the nuclear spins and lets them spread in the x y plane, effectively scrambling them so that the net polarization becomes zero (Fig. 4.6(c)).

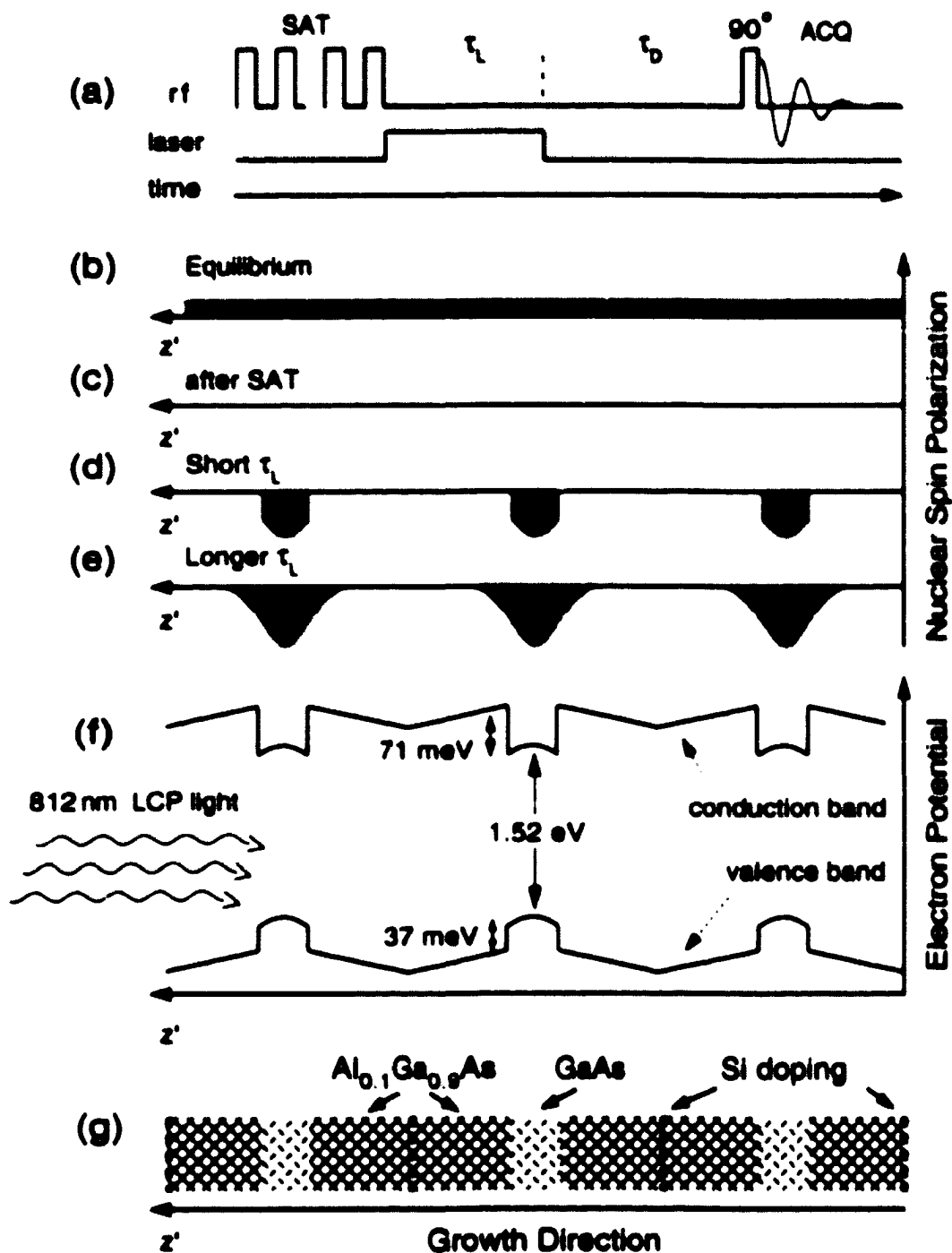


Figure 4.6: (a) OPNMR timing sequence, which includes a saturating train of rf pulses (SAT), a "Light on" period τ_L followed by a "Dark time" τ_D ; a single 90° tipping pulse, and NMR acquisition (ACQ). (b-e) the nuclear polarization in the spatial dimension z' , along with (f) the band diagram and (g) the schematic of the sample, same as in Fig. 4.1.

Shortly after that a home-made TTL-controlled optical shutter is opened to let the light through, and optical pumping takes place. Fig. 4.6(d) shows the nuclear polarization building up preferentially near the center planes of the quantum wells, where the three-dimensional electron density is the highest, and the light tuned to 1.52 eV gap in the pure GaAs is absorbed (Fig. 4.6(f)).

As the light is left on for a longer time (several minutes), nuclear spin diffusion due to nuclear dipole-dipole couplings slowly takes place, leading to a build-up of polarization in the regions of barriers close to the quantum wells (Fig. 4.6(e)).

The light is eventually turned off, and the electrons in the sample equilibrate with the lattice, which in turn equilibrates with the helium bath (see Section 4.5 for details). Nuclear spins possess the longest time constant, and a significantly enhanced (due to optical pumping) nuclear polarization can be still detected with a single 90° pulse long after all other processes have reached thermal equilibrium.

Ordinarily this sequence was repeated up to 256 times to increase the signal-to-noise ratio, limited, in principle, by the hold time of a liquid ^3He puddle. Optical pumping efficiency drops off sharply at high tilt angles, and also at certain filling factors where the electron-nuclear coupling is suppressed due to a gap in the excitation spectrum, e.g. at $\nu = 1$. In such instances a "dynamic" approach was sometimes used, where optical pumping was accomplished at low tilts and then the sample was rotated quickly to the desired θ before applying the tipping pulse. The use of this approach was rather limited due to friction, which caused excessive wear of the delicate rotator mechanism and also led to sample heating.

4.4 Optical Pumping

We used Coherent continuous wave lasers (a 7 Watt *Innova 300* Argon-ion to pump a 1.5 Watt tunable Titanium:sapphire of the *890* series) as a source of light.

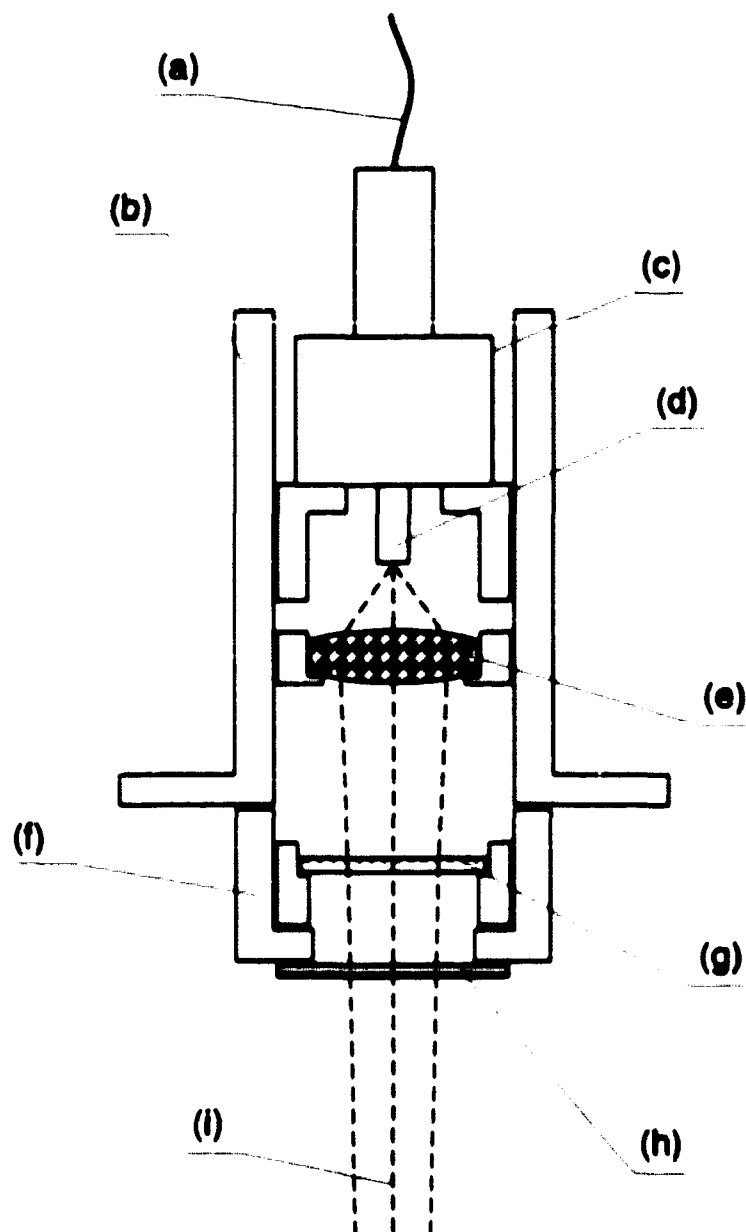


Figure 4.7: Optical assembly that terminates (a) the multimode optical fiber at the 1.5 K point in the cryostat ~ 20 cm above the sample. The housing (b) contains (c) the optical fiber connector with a ceramic tip (d) above the lens (e). Attached below is (f) the polarizer assembly, with (g) a linear polarizer in a small adjustable mount, and (h) a quarter-wave plate. The dashed lines (i) show the collimated light beam.

backed-up (in case of failure) by a 35 mW temperature-controlled diode laser. The frequencies of both systems were calibrated using a wavelength-meter, kindly lent to us by Prof. Bob Grober's group a number of times. Upon exiting the laser, the light was sent through a $\lambda/2$ plate and a linearly-polarizing beam-splitting cube so that the power of the light could be adjusted by rotating its polarization direction using the plate, thus determining which fraction of the light would travel straight through the cube, and which would be sent 90° away into the beam trap. Light was further chopped with a home-made TTL-controlled beam shutter and brought into the cryostat via a multimode optical fiber, which was cemented through a vacuum feed-through and had a convenient "FC" connector on top of the cryostat probe.

Figure 4.7 shows the optical assembly⁹, which was mounted ~ 20 cm above the sample at the 1.5 K point of the cryostat. Upon exiting the fiber, the diverging (about $\pm 20^\circ$) light cone was collimated with an anti-reflection coated lens (Fig. 4.7(e)) and then left-circularly polarized by going through a Polacor linear polarizer (a grating of microscopic parallel metal strips) and a true first-order quarter-wave plate. Half of the light power was absorbed by the linear polarizer, so a good thermal link to the 1 K pot of the cryostat was essential to handle this heat load.

In practice, the fast axis of the quarter-wave plate was aligned 45° to the direction of strips on the linear polarizer about once a year by minimizing power variations of the light that passed first through the assembly and then through a slowly rotated polarizing cube. Before each cool-down, the size of the light spot hitting the sample was adjusted by sliding the tip of the fiber connector (Fig. 4.7(d)) up or down relative to the lens. The collimated beam was then aimed at the sample by adjusting double nuts on the three screws that held the optical assembly in space above a baffle in the cryostat. This arrangement worked well over two years of experiments, with minor

⁹We thank Prof. D. Heiman and Dr. F. Plentz (MIT) for helpful discussion of the optical assembly design.

set-backs when the lens occasionally unglued from its mount and needed to be glued back on again¹⁰.

4.5 Temperature Control

The low temperature measurements ($0.29 < T < 20$ K) described in this thesis were performed using either a ^3He sorption-pumped *Heliox* cryostat made by Oxford Instruments, or an Oxford ^4He bucket dewar that Prof. Kurt Zilm's group at the Chemistry department kindly lent to us in 1996. A special vacuum adapter and a spacer were machined to accommodate the Heliox probe in the bucket dewar, which was used to trouble-shoot our optics and the NMR circuits in an easy-to-run bucket¹¹ cryostat. We used it at 4.2 K when vented into the atmosphere, or pumped on it continuously letting it equilibrate around 1.5 K. In the GaN measurements (Chap. 7) we took some

¹⁰A problem here was due to thermal differential contraction between the glass and the metal (brass) of the mount. To avoid cracking the lens at low temperatures, it was only glued to the mount at one point on its circumference. Subsequent thermal cycling led to occasional failures of this joint.

¹¹Although quite simple, the bucket dewar design was remarkably efficient: a single transfer of ~ 5 liters of liquid ^4He would last for about 8 hours at 4.2 K, or 6 hours at 1.5 K. Its outer diameter was 3.5" (88.9 mm) which fit perfectly into the room-temperature bore of our superconducting magnet, while its inner diameter of 2.5" (63.5 mm) left plenty of space for experiments. It could be cooled down from room temperature in 1.5 hours and provided nearly ideal non-sparking and absolutely stable liquid helium environment. For example, below 2.1 K, the helium was a superfluid with extremely high thermal conductivity and therefore no bubbling that could scatter light during optical pumping. Finally, this cryostat was absolutely non-magnetic even in a 12 T field, so no additional shimming was required. Compare this to the ^3He alternative: 8 hours, 25 liters of liquid ^4He just to cool down, 100 liters/day liquid ^4He consumption during experiments, available probe diameter of only 31 mm, arcing, need to recharge ^3He pot every half an hour when using 30 mW of light... only to get down to 0.29 K !

data at 77 K by filling the bucket dewar with liquid nitrogen. It lasted for 2 days and later had to be emptied out. there was still plenty of liquid inside.

The ^3He cryostat could be stabilized easily either at 1.5 K (by keeping the charcoal sorption pump warm, at ~ 45 K), or close to its base temperature of 0.29 K (by cooling the charcoal to 4 K with fresh ^4He). At the intermediate temperatures an Oxford ITC temperature controller was used to actively adjust the charcoal sorption pump temperature, and thereby its pumping speed, trying to keep the ^3He pot temperature constant. The following *PID* control settings were used: $P = 0.5$, $I = 2$, $D = 0$ for $0.5 \text{ K} < T < 1.5 \text{ K}$, and $P = 0.38$, $I = 0.5$, $D = 0$ for $T < 0.5 \text{ K}$. Above 1.5 K a different control strategy was employed, since we could not pump on liquid ^3He any more. The 1 K pot mechanical pump could be throttled first, to get the 1 K pot temperature as high as 3 K, and the charcoal sorption pump needed to be kept at a lower constant temperature of 30 K. If necessary, a heater wrapped around the ^3He pot was employed to actively control its temperature via an ITC controller using the following *PID* settings: $P = 20$, $I = 2$, $D = 0$.

Apart from controlling the temperature of the ^3He pot, it was necessary to ensure a good thermal contact between the sample and the ^3He bath, and to measure the sample temperature as it changed in response to quite powerful (up to $\sim 10 \text{ mW}$) laser light pulses.

Figure 4.8 shows how the thermal contact to the sample was made while keeping the NMR coil, wrapped around it, electrically insulated from the underlying copper plate. The sample was glued to a grooved support (Fig. 4.8(c)) made out of a single crystal sapphire, an excellent thermal conductor at low temperatures and at the same time one of the best electrical insulators¹². The sapphire support was in turn

¹²In addition, sapphire crystals have a uniaxial symmetry, and the spin $\frac{5}{2}$ aluminum nuclei in them possess a non-zero quadrupole moment (Table 4.2). This coincidence makes sapphire an excellent tilt sensor as well (see Appendix B).

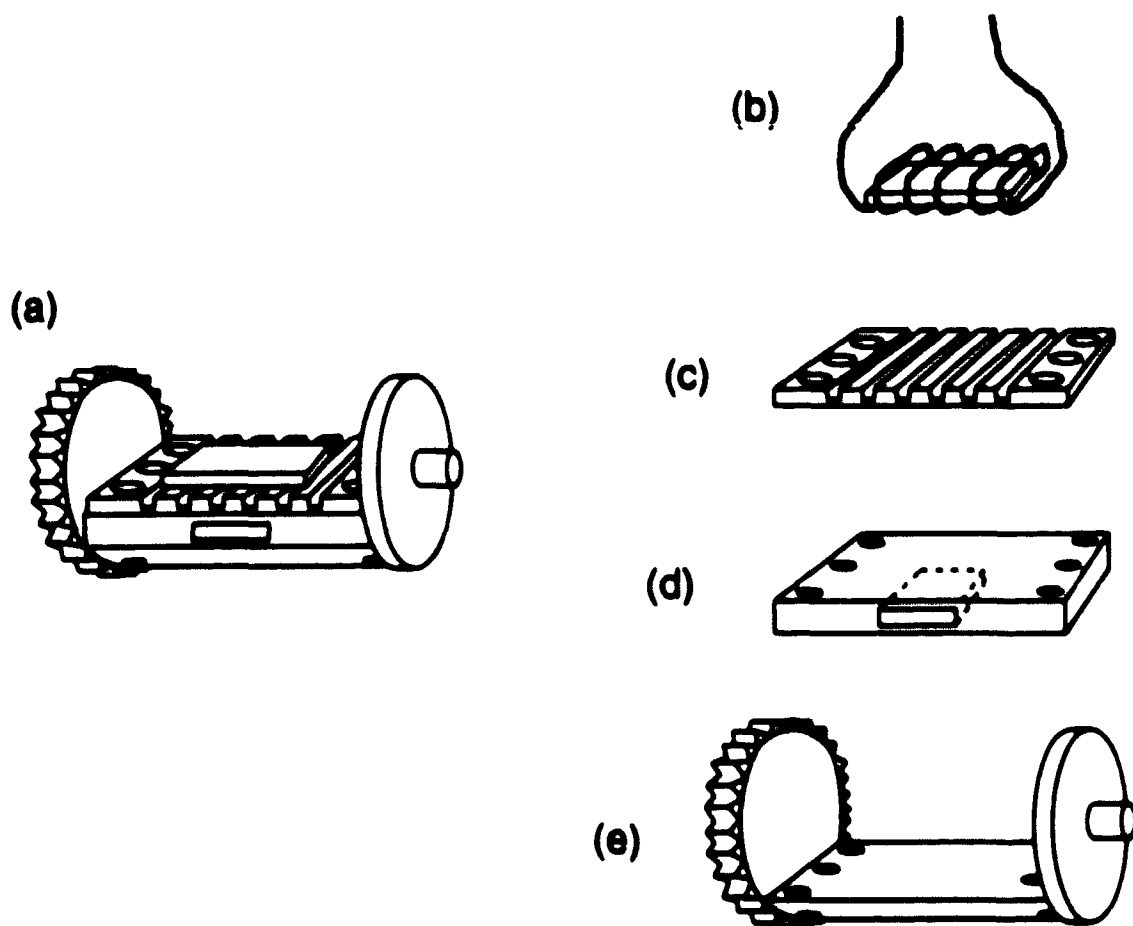


Figure 4.8: The rotator platform (a assembled, e bare) with (b) the sample, (c) the grooved sapphire support, and (d) the copper thermometer plate shown separately, offset from one another for clarity. Note an NMR coil wrapped around the sample in (b), and the slit cut in the copper plate (d) to accommodate the RuO_2 thermometer (not shown).

attached to a copper plate (Fig. 4.8(d)) which, being in good thermal contact (via sapphire) with the sample, served two purposes: it provided a heat sink to the brass rotator housing for the sample¹³, and also contained a RuO₂ thermometer, shown in Figure 4.9(a) at position 2, which was used during the experiments to track the sample temperature in real time.

One of the major concerns was how the sample temperature would respond to the light pulses and how fast it will equilibrate with the ³He bath after the light was turned off. To find out the answer, we placed one more RuO₂ sensor temporarily on top of the sample surface¹⁴ (Fig. 4.9(a), position 1) and performed a test OPNMR experiment while recording the temperature. Figure 4.9(b) shows the results, from which the following conclusions can be drawn: (a) although the sample temperature gets as high as 2 K when illuminated by a 10 mW laser pulse, it drops back down to ~350 mK fairly fast (less than a minute), reaching 0.5 K as soon as 5 s after the light has been turned off; (b) our permanent thermometer at position 2 gives an accurate reading of the sample temperature except when the light is on (this was also verified directly by sampling sensors 1 and 2 during the same pulse); and (c) the effects of the dropping liquid ³He level were observable, but did not radically change the sample's thermal response to light until the very end, when the liquid was completely boiled off. Thus, (a) argues that OPNMR measurements are possible down to the lowest temperatures of ~0.3 K, since the nuclear relaxation times at these temperatures are usually on the order of at least several minutes, long enough for the sample to cool

¹³Due to thermal Kapitza resistance [44] at the interface between the sample and liquid ³He, the cooling of the sample mostly took place through the brass housing of the rotator (Fig. 4.2(a)) that was a good thermal conductor and also had a much larger area of contact with liquid helium compared to the sample.

¹⁴The sensor was glued onto the sample with G. E. varnish to the side of where the light spot was directed, and shielded from scattered light by aluminum foil.

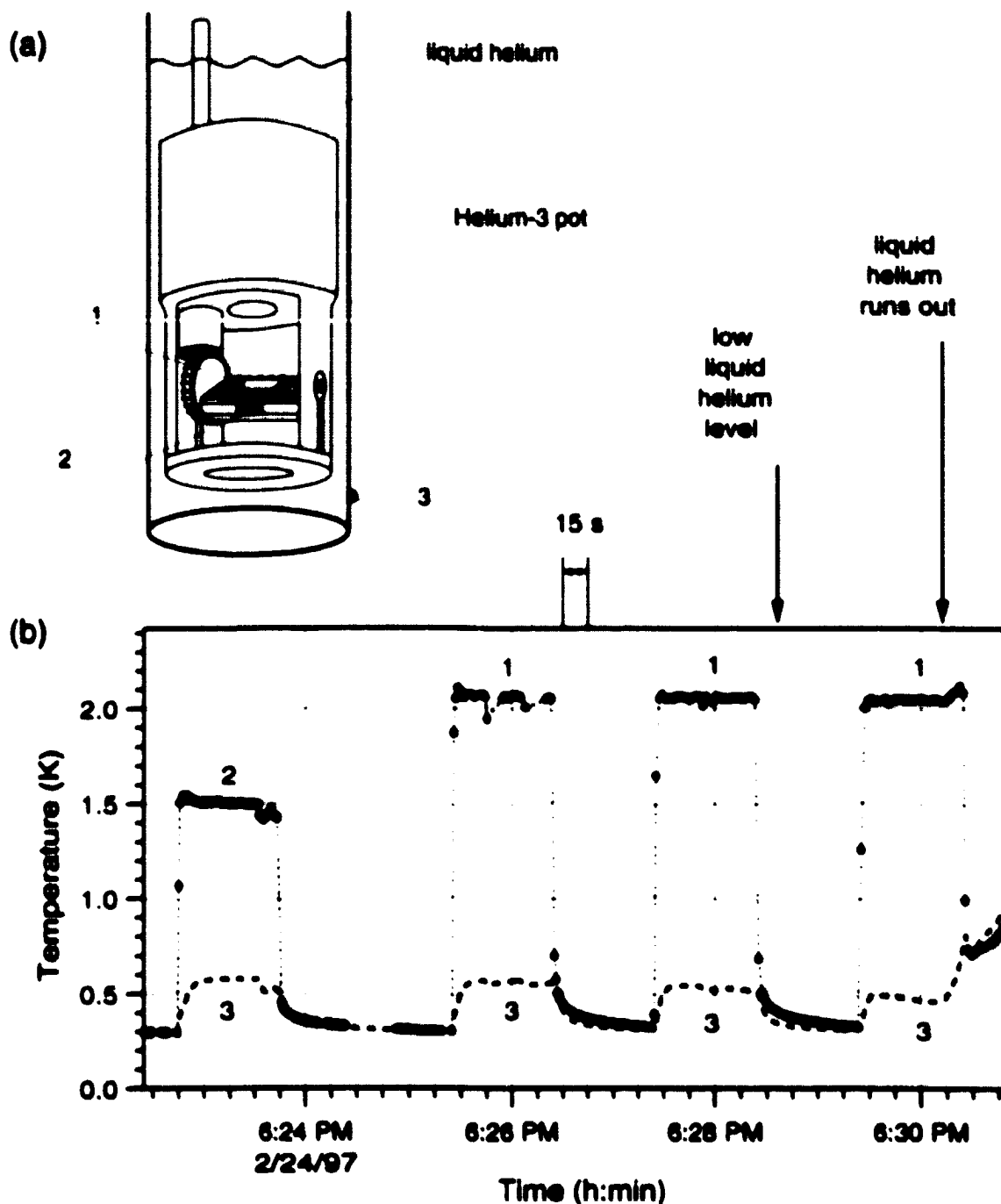


Figure 4.9: (a) Temperature response to light, measured with RuO_2 sensors at positions 1 - 3, plotted (b) as a function of real time. Several 60 s long, $\sim 10 \text{ mW}$ pulses of red (812 nm) light lead to depletion of the remaining liquid ^3He , causing the temperature of ^3He bath (sensor 3, thick dash) to run away in the end. Note, that as the liquid level becomes low, the temperature at the sample surface (sensor 1, not normally used in experiments) takes slightly longer to fully equilibrate with the bath.

down during τ_D before the NMR pulse arrives (Fig. 4.6(a)), while (c) offers evidence that the sample cooling mostly takes place through the rotator housing as opposed to direct contact with the liquid, validating our choice of sapphire and copper as means of heat sinking the sample.

Finally, the last remaining question on temperature control concerns the effect of high magnetic fields on RuO_2 sensors, that were initially calibrated at zero field. It was absolutely vital in our thermodynamic measurements to know the sample temperature exactly at any field, so we calibrated our thermometers anew in fields up to 12T using a field-independent capacitance reference (see Appendix A for the calibration data and analytic interpolations for sensor 2).

Chapter 5

Equilibrium OPNMR

Measurements of Electron Spin Polarization and Dynamics in the Quantum Hall Regimes

5.1 Effects of Optical Pumping on NMR Spectra

Optical pumping provides unique ways of manipulating a low-temperature NMR experiment, thus making possible use of non-equilibrium electrons to enhance NMR signals, which in turn can be used to provide crucial information about the equilibrium state of the electronic system at a later time. We will start this chapter by discussing NMR in the absence of optical pumping first, and then consider OPNMR spectroscopy in detail.

Figure 5.1 shows a series of ^{71}Ga NMR spectra of sample 40W, taken over a wide range of conditions. Following “traditional” NMR conventions, we plot Fourier-

transformed intensity of the NMR signal versus the "offset" frequency¹ $\Delta f = f - f_0$, where $f = \frac{\gamma}{2\pi} B_{\text{loc}}$ is the frequency of a given nucleus exposed to the local field B_{loc} , and f_0 is the fixed synthesizer frequency, usually selected near the spectrum center for the nuclear species of interest (see Table 4.2) in the given magnetic field B_{ext} .

Assuming that the magnet's field B_{ext} and the nuclear polarization² \mathcal{P}_n are uniform throughout the sample, we can say that the NMR signal intensity at each frequency f is measuring the number of nuclei exposed to the local field $B_{\text{loc}} = 2\pi f/\gamma$, so that the observed distribution of B_{loc} provides information about magnetic environments of the nuclear species³.

As Figure 5.1(a) shows, at room temperature the spectrum consists of only one line, which is essentially a Gaussian with a full width at half maximum (FWHM) of about 3 kHz. Our room temperature measurements indicate that the dependence of this width for ⁷¹Ga and ⁶⁹Ga on the tilt angle θ between the sample's growth direction (001) and the magnetic field \vec{B}_{ext} is well described by:

$$\Gamma_{\text{FWHM}}^{(71)} \text{ [kHz]} = 3.26 - 0.168 \times (1 - 3 \cos^2 \theta)^2. \quad (5.1)$$

¹In the early days of NMR [45], magnetic field was swept constantly around a central value, while the oscillator frequency was fixed. That way, an "up-field" shift at a fixed frequency corresponds to $B_{\text{loc}} < B_{\text{ext}}$, which translates into a "down-frequency" shift when using modern pulsed NMR techniques at a fixed B_{ext} . Following this convention, "down-frequency" shifts are still sometimes plotted to the right of the origin, while the "up-frequency" shifts are to the left.

²Nuclear polarization \mathcal{P}_n is uniform if the nuclear system is in equilibrium.

³In principle, ⁷¹Ga, ⁶⁹Ga, and ⁷⁵As all have spin $\frac{3}{2}$, and thus three allowed transitions for $\Delta m_j = -\frac{3}{2} \rightarrow -\frac{1}{2}$, $-\frac{1}{2} \rightarrow \frac{1}{2}$, and $\frac{1}{2} \rightarrow \frac{3}{2}$. These might show up in spectra as three distinct lines if an electric field gradient couples to the quadrupole moment of the nucleus. GaAs lattice, however, has a Zincblende structure which by symmetry does not allow any gradient at the locations of nuclei. Unless the sample is badly strained, such that significant piezo-electric fields develop (as was the case in earlier experiments [46] with the sample's substrate etched off), no quadrupole splitting is observed.

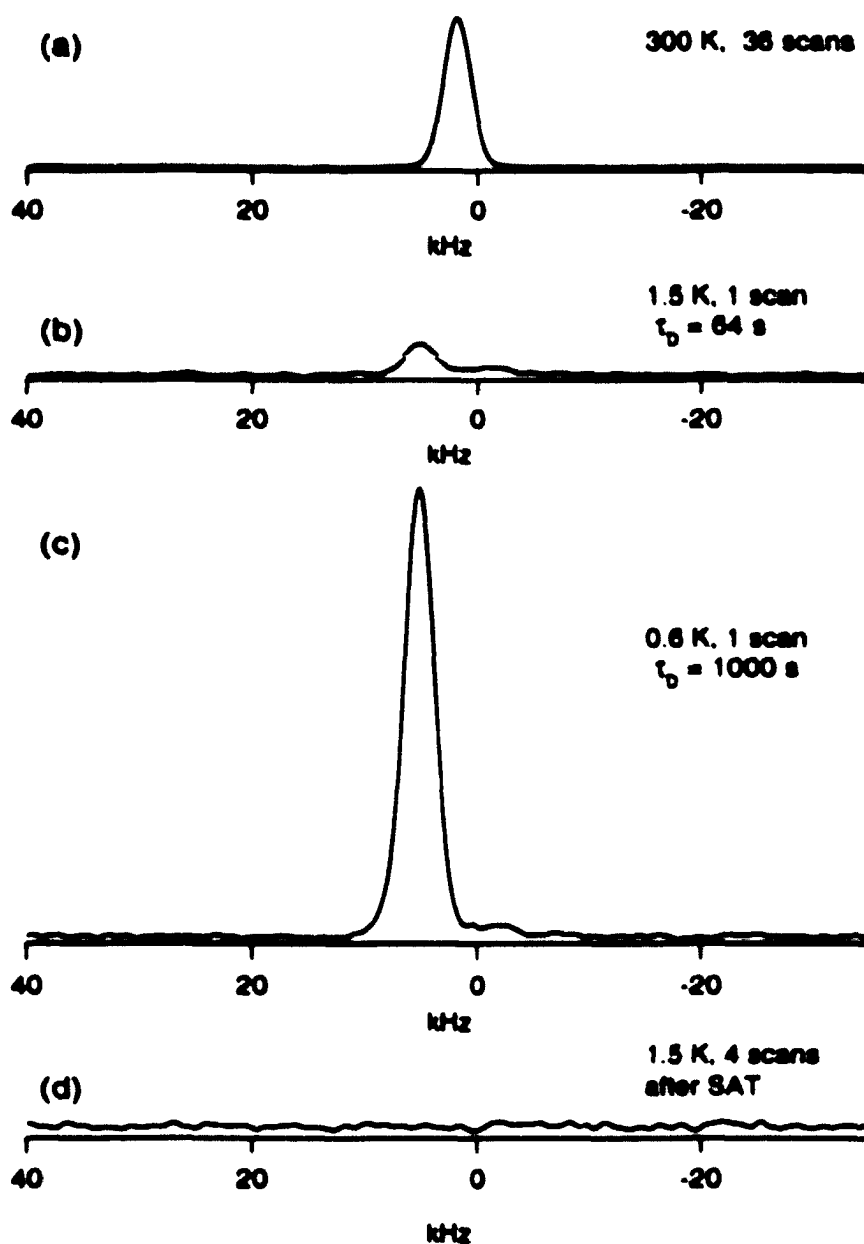


Figure 5.1: ^{71}Ga NMR spectra of sample 40W, acquired without optical pumping at $B_{\text{rot}} = 12$ T ($f_{\text{rot}} = 155.93$ MHz): (a) room temperature, averaged over 32 scans with 2 s repetition. (b) a single scan at 1.5 K taken after waiting for 64 s. (c) same at 0.6 K after waiting for ~ 1000 s, and (d) average of 4 scans, each taken immediately after a saturation pulse train, labeled SAT in Fig. 4.6(a). The signal in a-c is coming mostly from the 0.5 mm thick GaAs substrate (Fig. 4.1), although some quantum well signal can be seen in (b) and (c) shifted down in frequency (i.e. to the right) from the dominant substrate signal. Also note a ~ 3.5 kHz shift of substrate frequency from (a) to (b) upon cool-down, due to paramagnetic impurities in the rotator assembly.

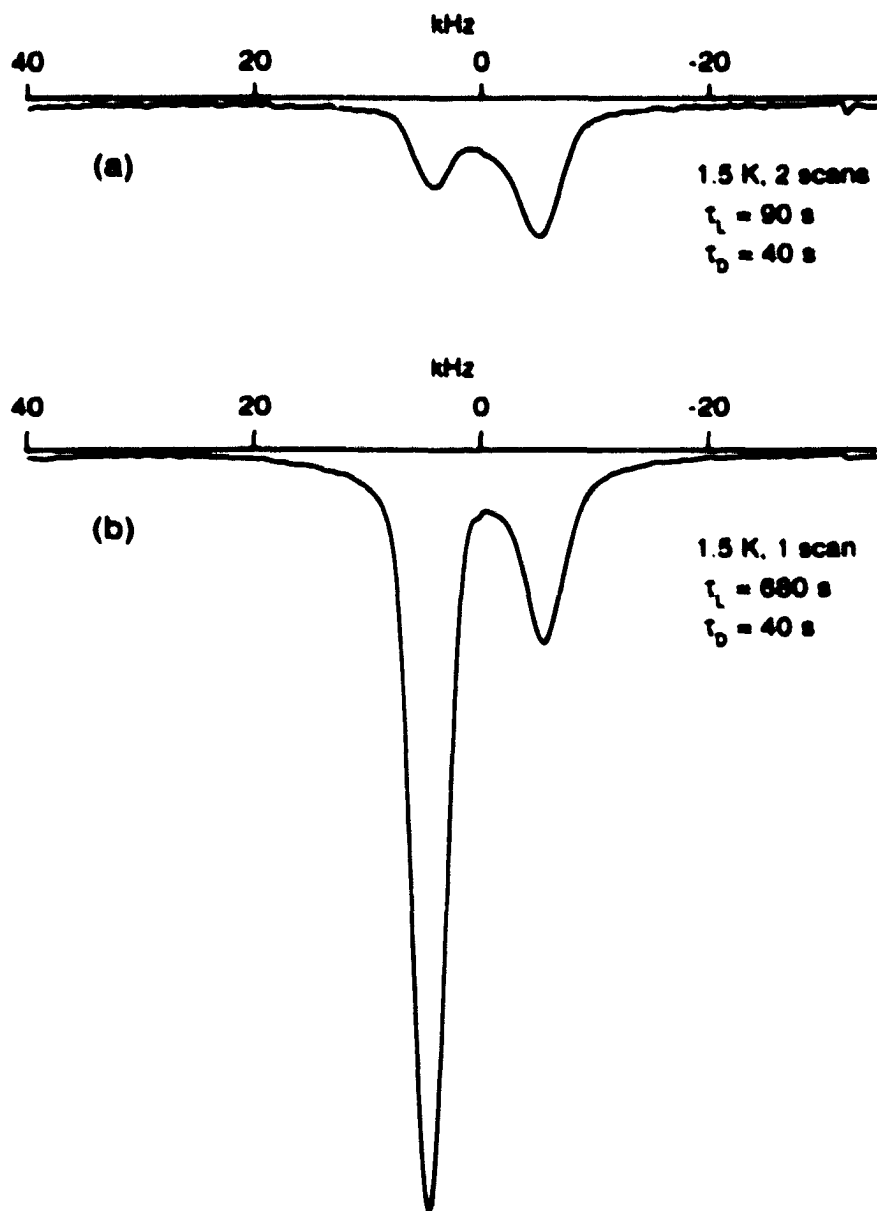


Figure 5.2: Optically pumped ^{71}Ga NMR spectra of sample 10W (tilted by $\theta=36.8^\circ$), acquired at 12 T (155.93 MHz) after (a) usual and (b) long optical pumping times of 90 s and 680 s respectively followed by a “Dark” time $\tau_D=40$ s. Note, that the signals are inverted, corresponding to the emission rather than absorption of rf photons by an inversely-populated nuclear spin system. Both peaks are now clearly visible, one (to the right) coming from ^{71}Ga nuclei in the quantum wells, that saturate at long optical pumping times, and the other (to the left) from the nuclei in the adjacent barriers. During optical pumping the barrier signal grows continuously as more and more nuclei there are polarized through the nuclear spin diffusion.

$$\Gamma_{\text{FWHM}}^{(\infty)} \text{ [kHz]} = 2.75 - 0.128 \times (1 - 3 \cos^2 \theta)^2. \quad (5.2)$$

consistent with being due to the dipole-dipole coupling to near-by nuclear spins [6].

At low temperatures (Fig. 5.1(b c)) nuclear relaxation rates become very long, especially in the substrate that has no free electrons to couple to the nuclear spin system. Fortunately, a saturation pulse train can quickly destroy any history-dependent nuclear polarization (Fig. 5.1(d)), so that measurements can be repeated one right after another starting with the same initial conditions. Figure 5.1 also shows that in principle it is possible to observe quantum well signals with a regular NMR, if, for example, the number of quantum wells in the sample is increased and the barrier/substrate peak does not mask the quantum well signal (e.g. due to a large difference in the nuclear relaxation times T_1 or because the frequency shift between the two is much larger compared to the dipolar width).

Much more can be done, however, by using optical pumping with left-circularly polarized (LCP) light. Figure 5.2 shows OPNMR spectra, obtained after 90s and 680s of illumination. First of all, the quantum well signal (shifted down in frequency compared to the barrier) is clearly seen, both signals being inverted (emissive), compared to the absorptive "dark" NMR signals. We can identify these two signals as follows: the dependence of their amplitude on pumping time τ_L (compare Fig. 5.2 (a) and (b)) indicates that a peak to the left corresponds to a much larger reservoir of nuclear spins (i.e. the $\text{Al}_{0.1}\text{Ga}_{0.9}\text{As}$ barriers and the GaAs substrate of the multiple quantum well structure shown in Fig. 4.1). In contrast, the peak to the right is the first to rise during τ_L , but quickly saturates at longer pumping times. Also, by varying the wavelength of light we can probe the optical absorption spectrum of the quantum well (as discussed below), so that a direct identification of the optical pumping frequency corresponding to the narrowest bandgap in the MQW structure (i.e. 1.52 eV in the GaAs quantum wells, Fig. 4.1) is possible.

5.1.1 Primitive Optical Spectroscopy: Optimizing the Wavelength

The main purpose of optical pumping is to selectively boost the NMR signal in the quantum wells (which contain much fewer nuclei) relative to other parts of the sample. To optimize OPNMR measurements in this respect, it is advantageous to perform “NMR-detected” optical spectroscopy on each sample at a new value of magnetic field prior to other measurements. This was usually done in a ^4He bucket cryostat (with a better handling of high rf and light power) by changing the wavelength of laser light one step at a time, taking an OPNMR spectrum, and plotting the signal amplitude of the quantum well peak versus the laser wavelength.

Figure 5.3 shows the data acquired this way with the left-circularly polarized light for the two samples in a 12 T field⁴. No optically pumped quantum well signal is observed below 1.523 eV (i.e. above 814 nm), although some pumping does take place at those wavelengths in a much thicker GaAs substrate. The NMR signal of the substrate, however, is not shifted to the right (e.g., the dominant peaks in Fig. 5.1(b,c)) by the coupling to the unpaired spins of the two-dimensional electron system (2DES), which makes it possible to distinguish the absorption in the quantum well from that elsewhere in the sample.

Finally, we should mention the difference between the LCP and RCP light as possible sources of optical pumping⁵. At high magnetic fields the degeneracy in the valence and conduction bands is lifted [47]; thus pumping with the LCP (or RCP) light links the sub-bands corresponding to different spin states. Due to these

⁴The picture is somewhat different at lower fields, e.g. at 4 T the absorption edge is shifted out to 817 nm.

⁵In our convention, the light is assumed to propagate along the direction of magnetic field \hat{B}_{tot} , i.e. down, if the magnetic field is pointing down (as in our set-up), or up, if the field is up (as in the earlier experiments [9, 26], that used a cryostat with optical windows in the bottom).

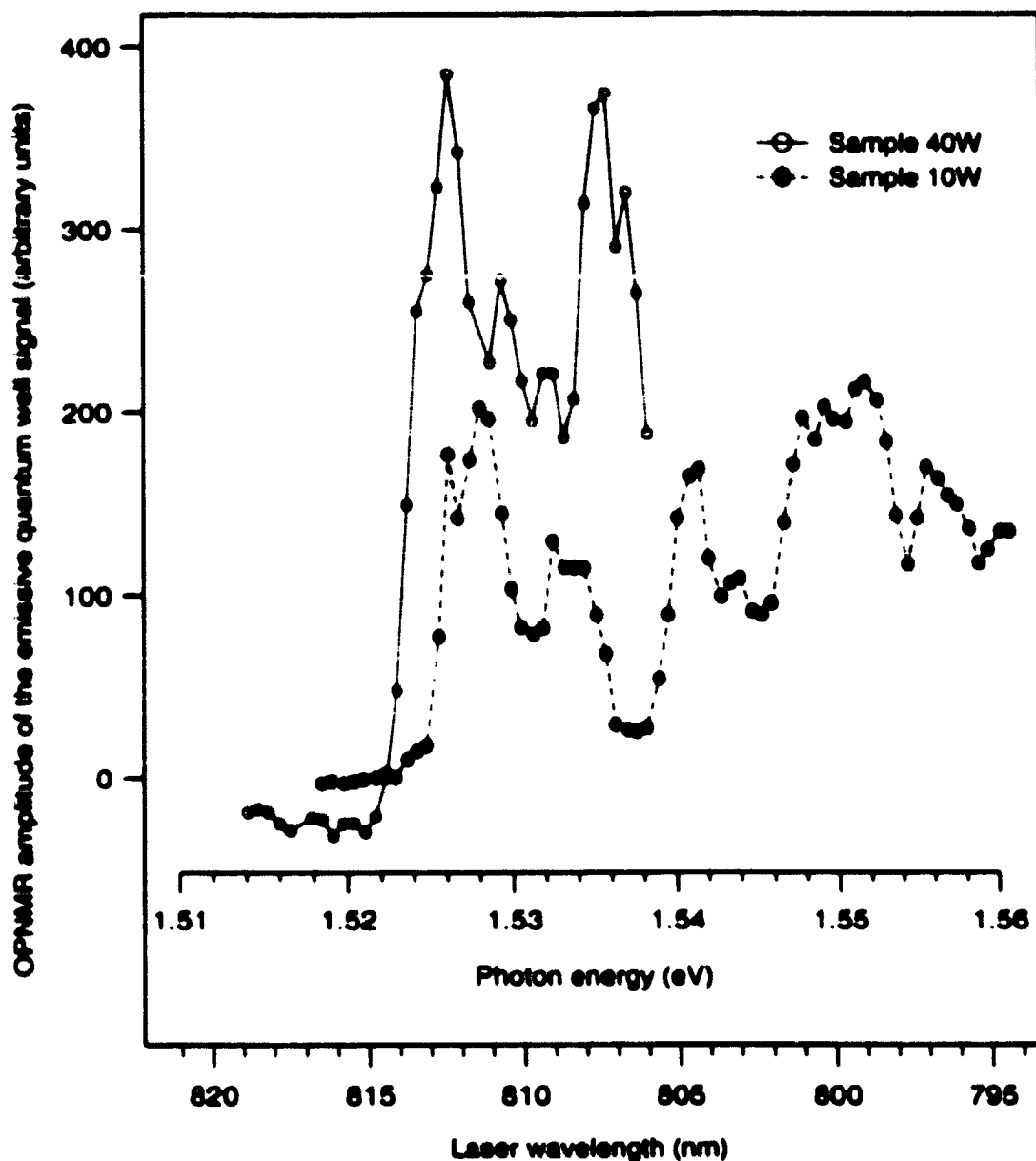


Figure 5.3: OPNMR signal amplitude at the quantum well peak frequency as a function of laser wavelength, shown for samples 40W and 10W at 12 T (155.93 MHz). A quantum well absorption edge at 1.525 eV can be seen in both samples (compare to the band diagram in Fig. 4.1). Lines are to guide the eye.

circumstances, optical pumping with the LCP light leads to stronger NMR signals compared to the RCP light.

5.2 A “Motionally Narrowed” Interpretation of the OPNMR Line Shape

In this section a detailed model for the OPNMR line shape will be proposed. A key underlying assumption of “motional narrowing” will be defined in terms of basic nuclear and electron length- and time-scales at these low temperatures.

A typical ^{71}Ga OPNMR emission spectrum⁶, shown in Figure 5.4 (solid line), exhibits two peaks: one (labeled “W”, usually asymmetrically shaped) that arises from nuclei in the GaAs quantum wells, and the other (labeled “B”, more symmetric) which can be ascribed to nuclei in the $\text{Al}_{0.1}\text{Ga}_{0.9}\text{As}$ barriers [26, 27, 48, 49]. The Fermi contact hyperfine interaction between the unpaired electron spins \mathbf{S}_j of the 2DES and the nuclear spins \mathbf{I}_i , located in the quantum wells is described by the “electron-nuclear” term \mathcal{H}_{e-n} in the total spin Hamiltonian:

$$\mathcal{H}_{e-n} = \frac{8\pi}{3} \gamma_e \gamma_n \hbar^2 \sum_{ij} \mathbf{I}_i \cdot \mathbf{S}_j \delta(\mathbf{R}_i - \mathbf{r}_j), \quad (5.3)$$

where γ_e and γ_n are the gyromagnetic ratios for electrons and nuclei located at positions \mathbf{r}_j and \mathbf{R}_i , respectively, and the delta-function picks out only those electrons⁷ that have a non-zero overlap with a given nucleus i . This coupling to the electron spins of 2DES shifts the quantum well ^{71}Ga OPNMR peak (“W” in Fig. 5.4) down in frequency from the barrier (“B”) peak by K_N , which we define to be the Knight

⁶For convenience, we are going to plot emissive spectra upright from this point forward.

⁷In GaAs, as in many metals, electrons in the conduction band have predominantly S -like wave functions.

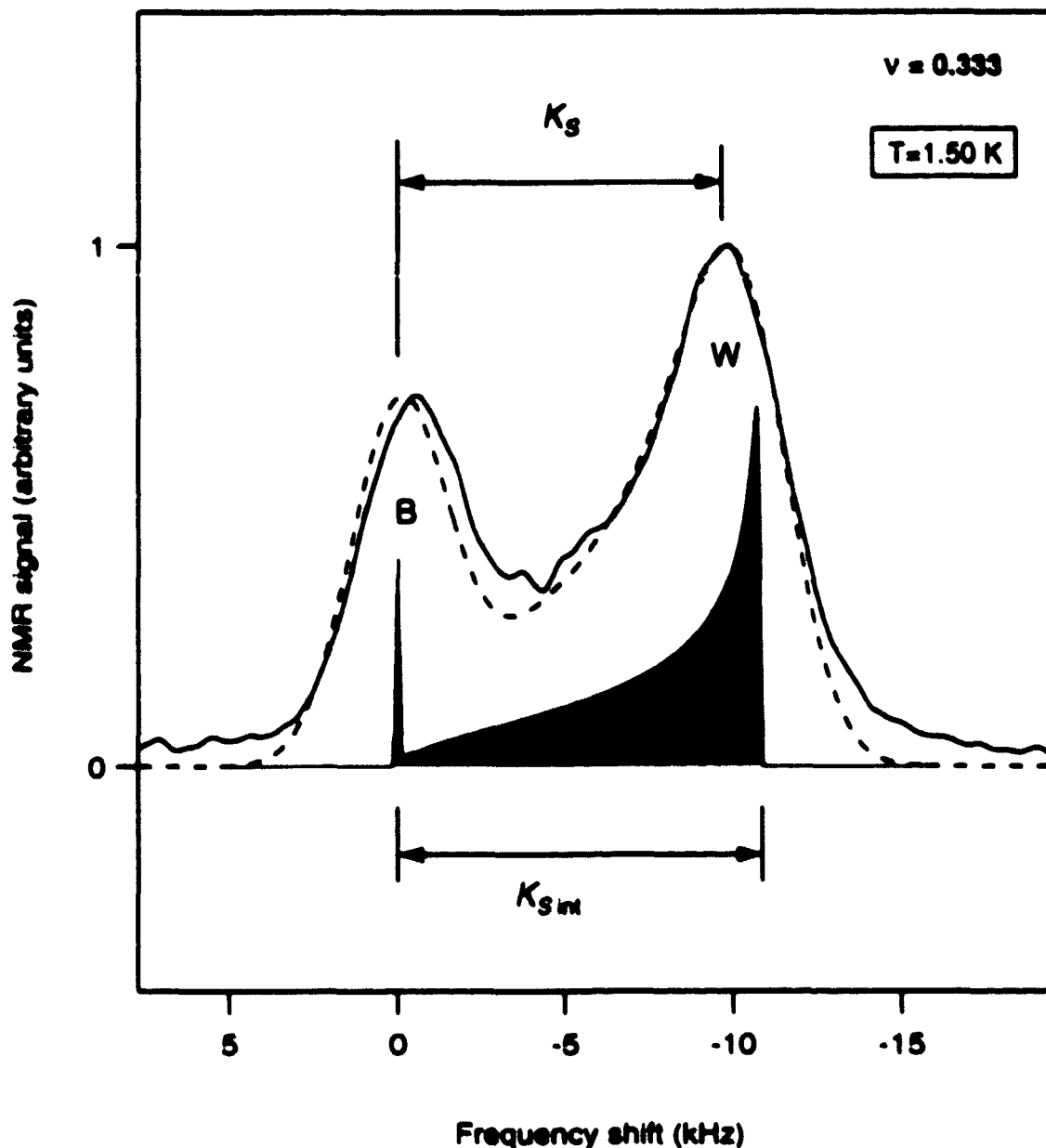


Figure 5.4: Interpretation of the OPNMR spectrum when motional narrowing is present: a ^{71}Ga emission spectrum (solid line) of sample 10W, taken at $\theta = 36.8^\circ$ and $T = 1.5 \text{ K}$, in $B_{\text{tot}} = 12 \text{ T}$ (155.93 MHz); the fit (dashed line, see Equation 5.4) is obtained by broadening the intrinsic line shape (shaded region) with a 3.5 kHz FWHM Gaussian. Empirically, $K_{S(m)} = K_S + 1.1 \times [1 - \exp(-K_S/2.0)]$ (all in kHz).

shift⁸ [6, 50].

The well peak, shown in Figure 5.4, is not a simple Gaussian, but has an asymmetric intrinsic⁹ structure due to the following two factors: first, the quantum confinement within the well causes the electron probability density (Fig. 5.5(b)) to vary across its width w as $\rho(z') \approx \cos^2(\pi z'/w)$, for $|z'| \leq w/2$ [51, 52]; and second, the optical pumping preferentially polarizes nuclei in the electron-rich center of the quantum well more¹⁰ than it does in the electron-poor regions near the barriers (Fig. 5.5(d)). Taking these two effects into account, the intrinsic line shape (Fig. 5.4, shaded region) may be represented by the sum of the quantum well signal $\sqrt{f/(K_{sim} - f)}$, shown in Fig. 5.5(e), and $a_b \delta(0)$ for the unbroadened barrier signal. Upon further convolution of this intrinsic line shape with a 3.5 kHz FWHM Gaussian¹¹ $g(f)$ for the nuclear dipolar broadening, we obtain the following two-parameter fit (Fig. 5.4, dashed line):

$$I(f) = I_b + I_w = a_b g(f) + \int_0^{K_{sim}} df' g(f - f') \sqrt{\frac{f'}{K_{sim} - f'}} \quad (5.4)$$

The first parameter a_b is the amplitude of the barrier signal, which grows during τ_L as the optically pumped nuclear magnetization diffuses out of the quantum well. The second parameter extracted from the fit is the hyperfine shift for nuclei in the

⁸Although of similar nature as in metals, Knight shift in semiconductor heterostructures is several orders of magnitude smaller and has an opposite sign (i.e. $\sim 1\%$ at room temperature in metals vs. $\sim -0.01\%$ at 1 K in our samples) due to a much lower density of unpaired electron spins combined with differences in the effective electronic g -factor (the latter affects the average electron spin polarization, but not K_s produced by a given electron).

⁹In this Chapter, we use the word “intrinsic” to describe effects that would be observed in the absence of dipolar broadening (see section 5.1).

¹⁰In simulations, we used nuclear polarization of the form $\langle I \rangle(z') \propto \rho^X(z')$, and found an exponent $X = 1$ to be consistent with all of our data. Thus $\langle I \rangle(z') \propto \rho(z') \propto f(z')$.

¹¹An experimentally observed $\sim 10\%$ increase in the dipolar linewidth due to cool-down from room temperature was taken here into account.

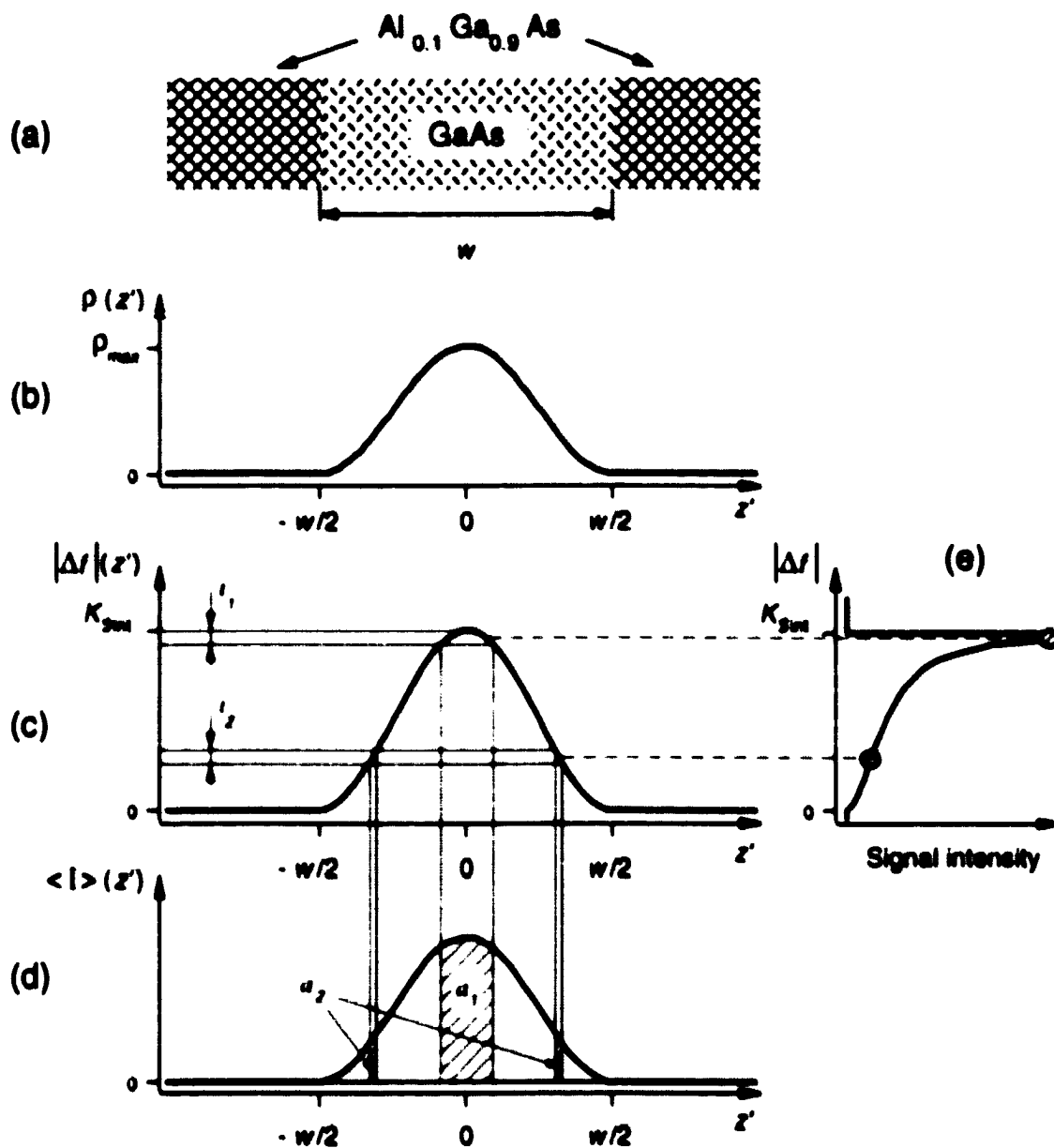


Figure 5.5: (a) Schematic of the quantum well structure and (b) the corresponding electron probability density $\rho(z')$ plotted along the growth direction z' . Within our model, both (c) the local shift of NMR frequency and (d) the local optically pumped nuclear spin polarization are proportional to $\rho(z')$. Shown in (c) are two equally wide frequency intervals ν_1 and ν_2 , which map onto unequal regions along z' , with the corresponding NMR signal intensities represented in (d) by areas a_1 and a_2 . The distribution of NMR signal in the frequency domain (i.e. the "intrinsic spectrum") is thus plotted in (e) for the range of frequency shifts $|\Delta f|$ from 0 to K_{Snt} .

center of the well¹²:

$$K_{sim} = \mathcal{P} \frac{n}{w} (4.5 \pm 0.2) \times 10^{-16} \text{ [kHz cm}^3\text{]}. \quad (5.5)$$

where \mathcal{P} is the electron spin polarization, which is defined in terms of spin-up and spin-down electron densities as:

$$\mathcal{P} = \frac{n_{\uparrow} - n_{\downarrow}}{n_{\uparrow} + n_{\downarrow}}. \quad (5.6)$$

Thus, fits to OPNMR spectra provide a direct measure of the electron spin polarization \mathcal{P} in the quantum well.

Finally, an important remark concerning the interplay of the electron and nuclear length scales over the time of a typical NMR measurement needs to be made. For the samples used, the average inter-electron separation is $\sim 300 \text{ \AA}$, and the magnetic length $l_H = (\hbar c / e B_z)^{1/2}$ (which can be thought of as a radius of the electron's smallest cyclotron orbit) is $\sim 80 \text{ \AA}$. Both of these length scales are much greater than the average inter-nuclear distance of $\sim 4 \text{ \AA}$.

This said, it must be realized that if the electron spins were localized on the time scale of our NMR measurement (nuclei probe their environment for $\sim 100 \mu\text{s}$ before they dephase), we *would not* get the line shape described above. Rather, the nuclei that are within regions of higher electron density will experience a larger hyperfine field compared to the nuclei outside of such regions. If the spread in the local electron densities $\delta n/n$ exceeds $\Gamma_{FWHM}^{(71)} / K_{sim} \sim 0.3$, such localization will be observed in the OPNMR spectra as an inhomogeneous broadening of the well line shape.

As long as the spectrum is well described by our fit (Eq. 5.4), the electron spins must be *delocalized*, so that their motion along the quantum well over the $\sim 100 \mu\text{s}$ NMR time scale averages out their local density fluctuations to less than 30%. We will say that the "motional narrowing" [6] of the line shape occurs in such case.

¹²The 4.4% error comes from a fit to the $K_S(\nu = \frac{1}{2}, T \rightarrow 0)$ data on three samples (10W, 40W, and a sample studied in [26]). For individual samples, \mathcal{P}/K_{sim} scaling is known to better than 2%.

5.3 Skyrmion Peak at $\nu=1$: Measurements of Electron Density

Using the Swedish rotator, we could vary the angle θ ($-60^\circ < \theta < 60^\circ$) between the sample's growth axis z^2 and the applied field \vec{B}_{tot} *in situ*, thus changing the filling factor ν defined as:

$$\nu = \frac{n}{n_\Phi} = \frac{n\hbar c}{eB_{\text{tot}} \cos \theta} \quad (5.7)$$

where n is the number of electrons per unit area in each quantum well and n_Φ is the two-dimensional density of the magnetic flux quanta, produced in each quantum well by the perpendicular component of magnetic field $B_\perp = B_{\text{tot}} \cos \theta$.

Figure 5.6 shows our Knight shift measurements¹³ in the two samples near $\nu=1$. The excellent agreement between positive θ (squares) and negative θ (circles) data points is consistent with the rotator accuracy of $\pm 0.1^\circ$ and was used to calibrate the rotator offset for each sample¹⁴. We infer the densities n for each sample from these measurements, assuming that $K_N(\theta)$ curve peaks exactly at $\nu=1$. The obtained density values, also listed in Table 4.1, are:

$$n_{40W} = 6.69 \times 10^{10} \text{ cm}^{-2} \quad \text{and} \quad n_{10W} = 7.75 \times 10^{10} \text{ cm}^{-2} \quad (5.8)$$

consistent with low-field magnetotransport characterization of the wafers. These values are very robust, as the four independent runs shown in Figure 5.6 for sample 40W reproduce n to within $\pm 0.5\%$.

Note that the sharp peak in K_N at $\nu=1$ is quite similar to the “skyrmion feature” previously observed [26] in a higher density sample at stronger magnetic fields. The

¹³The magnetic field was lowered from its usual 12 T value to reach this filling factor.

¹⁴A small constant correction (less than 1°) to the rotator readings was needed after each change of sample and/or cryostat to compensate for misalignments of different parts involved in positioning the sample with respect to the field.

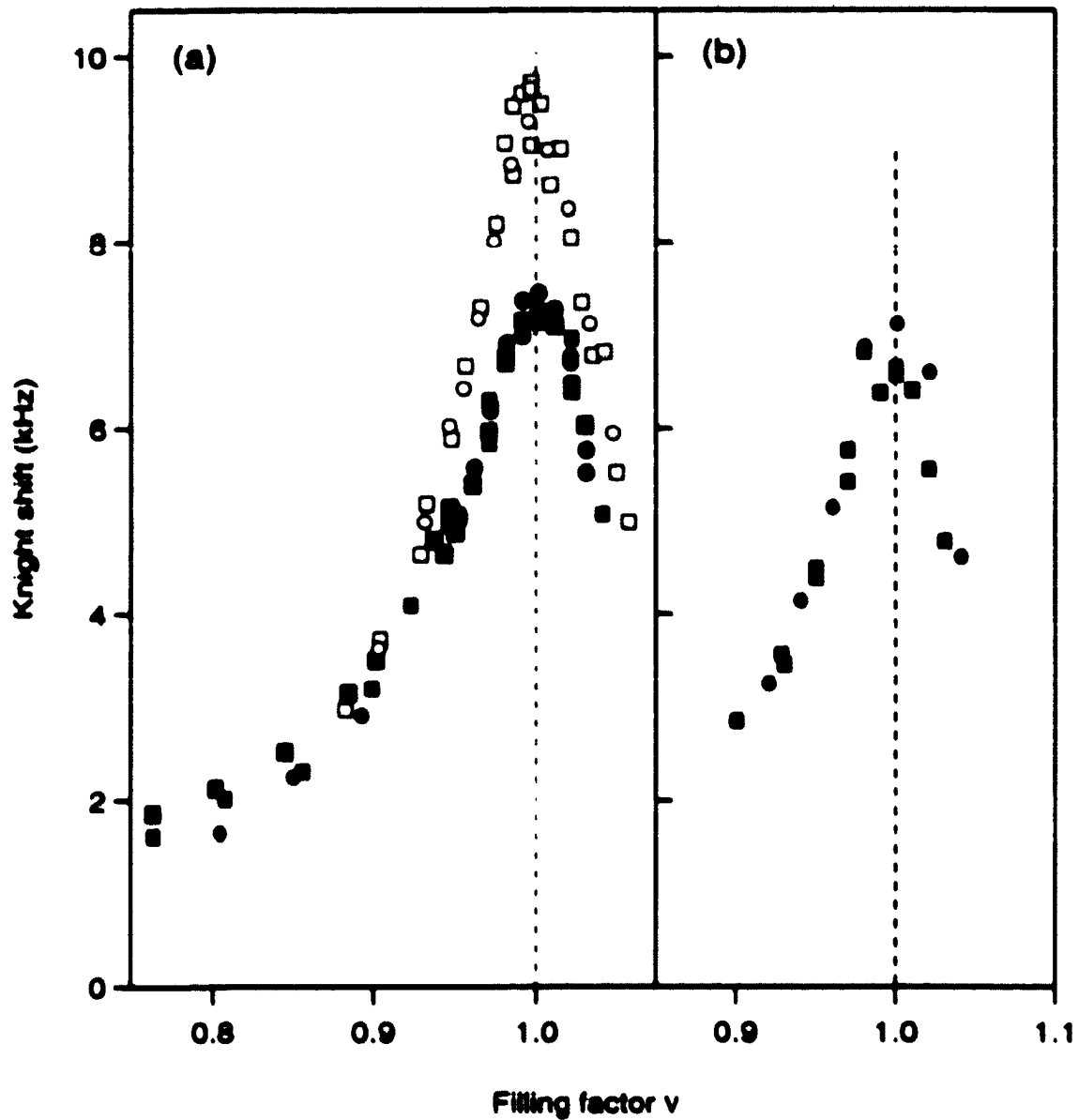


Figure 5.6: $K_S(\nu)$ data, measured near $\nu=1$ at $T = 1.5$ K: (a) samples 40W (filled and crossed symbols, three separate runs) and 10W (open symbols) at $B_{tot} = 3.6263$ T; (b) sample 40W at $B_{tot} = 3.2589$ T. Everywhere, round and square symbols denote data taken at negative and positive values of θ . The densities inferred from these measurements are: $n_{40W} = 6.69 \times 10^{10} \text{ cm}^{-2}$ and $n_{10W} = 7.75 \times 10^{10} \text{ cm}^{-2}$.

size¹⁵ of the skyrmion (anti-skyrmion) can be parametrized by the number \hat{S} (\hat{A}) of additional spin flips caused by introducing a unit of negative (positive) charge to the system. These numbers can be extracted from the slope of $K_S(\nu)$ on either side of $\nu = 1$. As inferred from Figure 5.6, the values $\hat{S} = \hat{A} = 3.1$ (for $B_{\text{tot}} \sim 3.5$ T) are slightly larger compared to [26] ($\hat{S} = \hat{A} = 2.6$ for $B_{\text{tot}} \sim 7$ T), in qualitative agreement with the change in the ratio of Zeeman and Coulomb energy scales E_Z/E_C , where $E_Z \equiv g^* \mu_B B_{\text{tot}}$ and $E_C \equiv v^2/\epsilon l_B$ [18, 19]. However, a quantitative comparison to the skyrmion model will require data below 1.5 Kelvin at these low fields, since $\mathcal{P}(\nu=1)$ in Figure 5.6 is only¹⁶ ~ 0.8 , which is below the expected low-temperature saturation value of $\mathcal{P}(\nu=1, T \rightarrow 0) = 1$.

5.4 Knight Shift Data in the Vicinity of $\nu = \frac{1}{3}$

5.4.1 Temperature Dependence $K_S(T)$ at $\nu = \frac{1}{3}$

Using the electron densities calculated in Eq. 5.8, we could tilt each sample by the angle θ necessary to achieve $\nu = \frac{1}{3}$ in $B_{\text{tot}} = 12$ Tesla. For the two samples (40W and 10W, respectively), we used the following values of θ , calculated from Eq. 5.7:

$$\theta_{40W} = 46.4^\circ \quad \text{and} \quad \theta_{10W} = 36.8^\circ. \quad (5.9)$$

Figure 5.7 shows ^{71}Ga OPNMR spectra (solid lines) of sample 10W over a range of temperatures at $\nu = \frac{1}{3}$. To resolve the Knight shift K_S better at high temperatures, the amplitude of the barrier signal was suppressed for small K_S spectra by using short (~ 10 s) optical pumping times τ_L .

¹⁵In this Chapter, we use the convention adopted in [48], that $\hat{S} = \hat{A} = 0$ in the non-interacting limit, instead of the earlier definition [26], $S = A = 1$, in the same limit.

¹⁶See Table 5.1 for the data on full spin polarization in these samples.

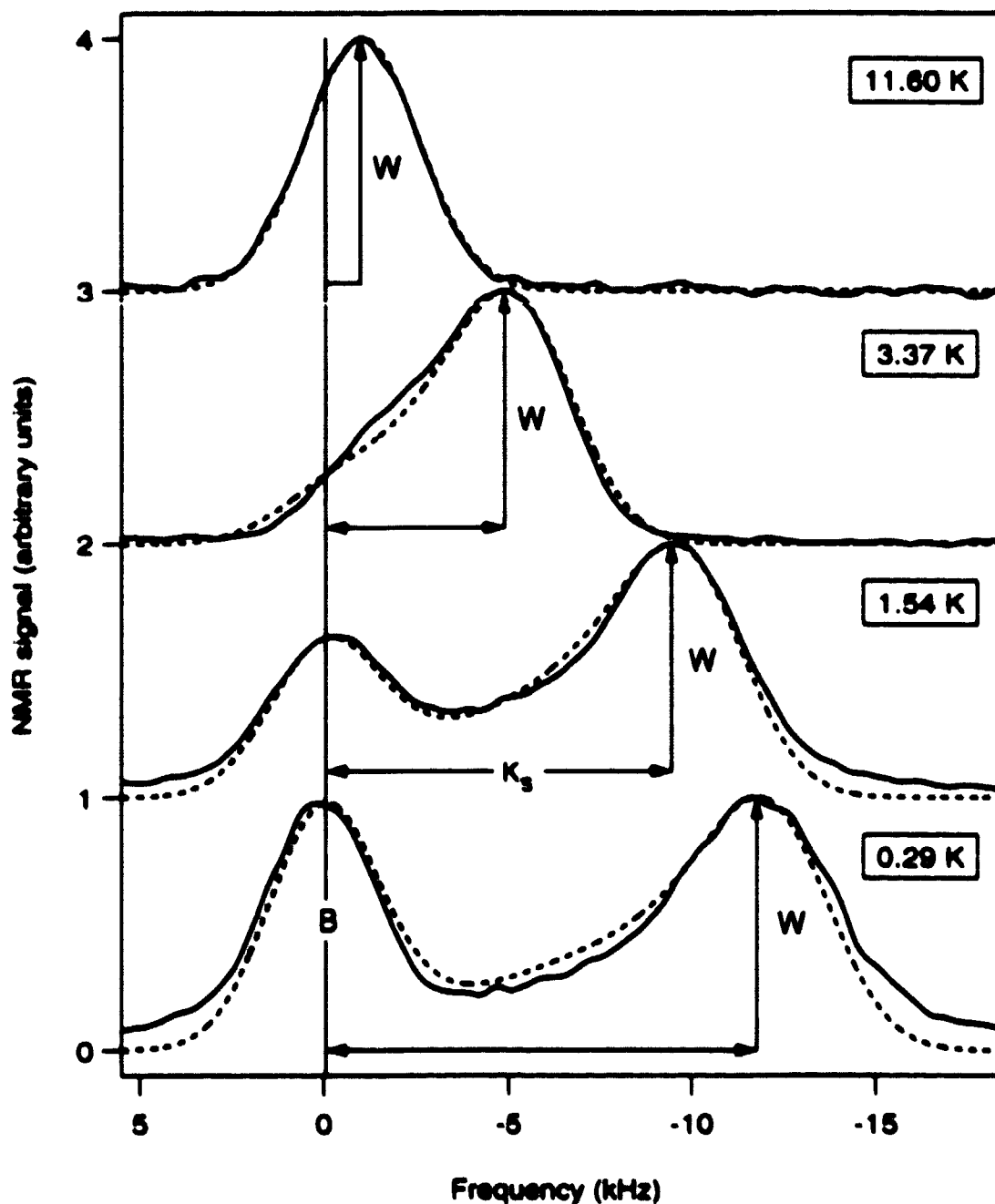


Figure 5.7: ^{71}Ga OPNMR spectra (solid lines) of sample 10W at $\nu = \frac{1}{3}$, taken at $\theta = 36.8^\circ$ in $B_{\text{ext}} = 12\text{ T}$ (155.93 MHz) as a function of temperature. Note, that at small Knight shifts (high temperatures) the barrier signal was suppressed by using short optical pumping times. The fits to the spectra (dashed lines) are made assuming the motionally-narrowed line shape (Equation 5.4).

The evolution of spectra shown in Figure 5.7 demonstrates how the “fractional quantum Hall ferromagnet” is being thermally quenched as its temperature increases from the lowest point that can be obtained in our ^3He system (bottom trace, 0.29 K) towards the highest temperature where OPNMR signal is still detectable from this sample (top trace, ~ 12 K), by which the Knight shift is only 9% of its maximal value). By all standards, this is a very fragile “ferromagnet”, since a temperature of only 3 K (approximately equal to the Zeeman temperature E_Z/k_B) is high enough to reduce its polarization by half.

It should also be noted, that all spectra in Figure 5.7 are well described by fits (dashed lines) of the form given in Eq. 5.4, which implies that over the time scale of the NMR measurement the motional narrowing makes the local electron spin polarization P_{loc} uniform everywhere in the plane of the quantum wells. In other words, although some thermally excited reversed spins are definitely present in the system (as seen from its depolarization) above one Kelvin at $\nu = \frac{1}{3}$, they move along the quantum wells fast enough to cover *all* ^{71}Ga sites (for a given z' , of course) equally on the time scale of $\sim 100 \mu\text{s}$.

Many more spectra were taken at $\nu = \frac{1}{3}$ in both samples as a function of temperature, as Figure 5.8 shows. Two different symbols (squares and triangles) are used for the 40W data which correspond to the independent cool-downs from room temperature¹⁷, which demonstrates the reproducibility of the data.

The inset in Figure 5.8 shows that at low temperatures the Knight shift saturates for both samples, as seen previously [26] in a higher-density sample at $\nu = 1$. The saturation values are marked by the dashed lines in Fig. 5.8 and can be found in Table 5.1.

In Figure 5.9 we plot the corresponding temperature dependence of the electron

¹⁷In the 10W data set, squares and triangles show the data separated by a warm up to about 100 K, that was necessary to change ^4He dewars.

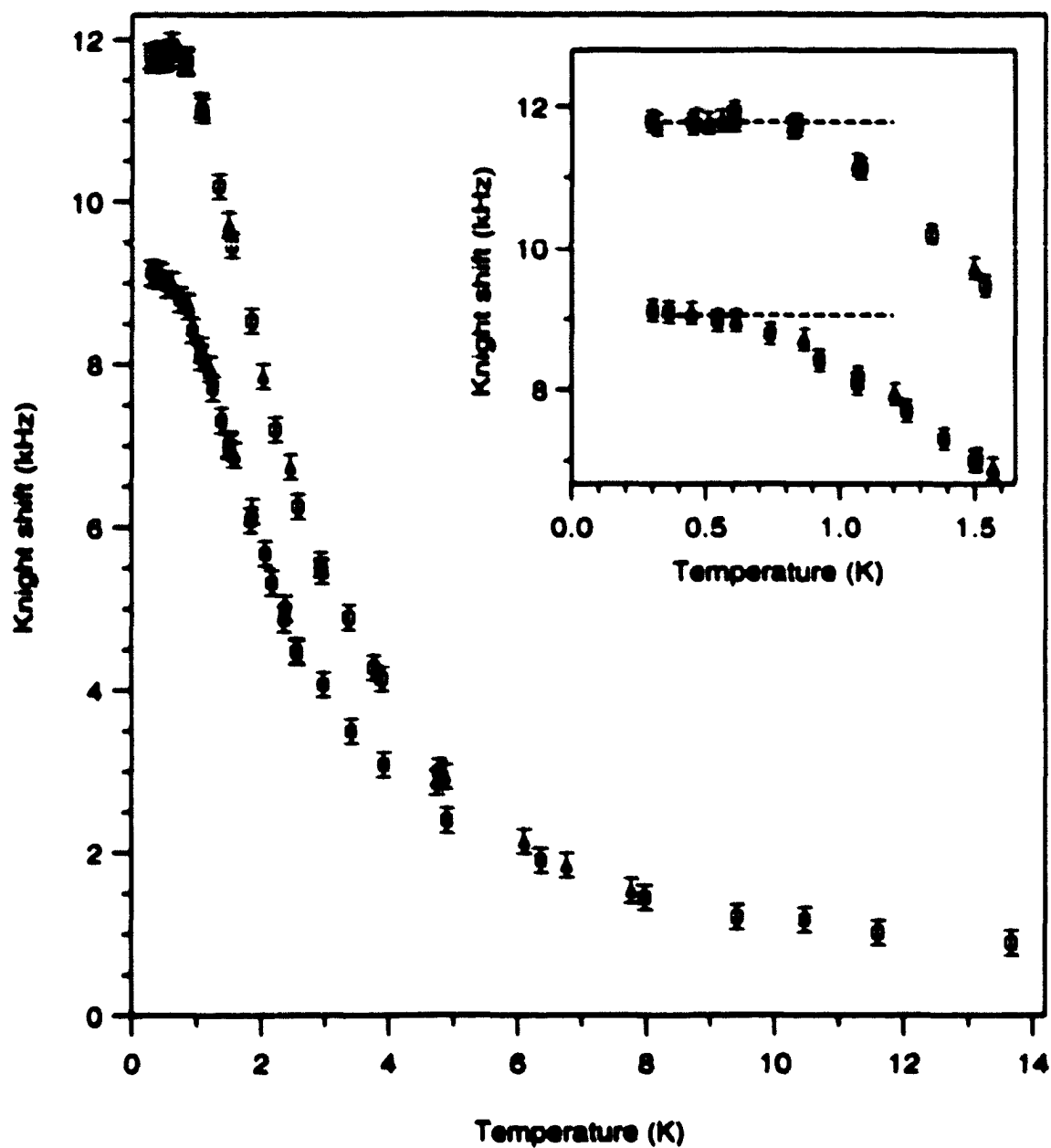


Figure 5.8: Knight shift dependence on temperature, measured for samples 10W (open symbols) and 40W (filled symbols) at $\nu = \frac{1}{3}$ (with $B_{\text{ext}} = 12$ Tesla, $\theta_{40W} = 46.4^\circ$, and $\theta_{10W} = 36.8^\circ$). Insets show the saturation regions. For both data sets, squares and triangles denote data taken on different cool-downs.

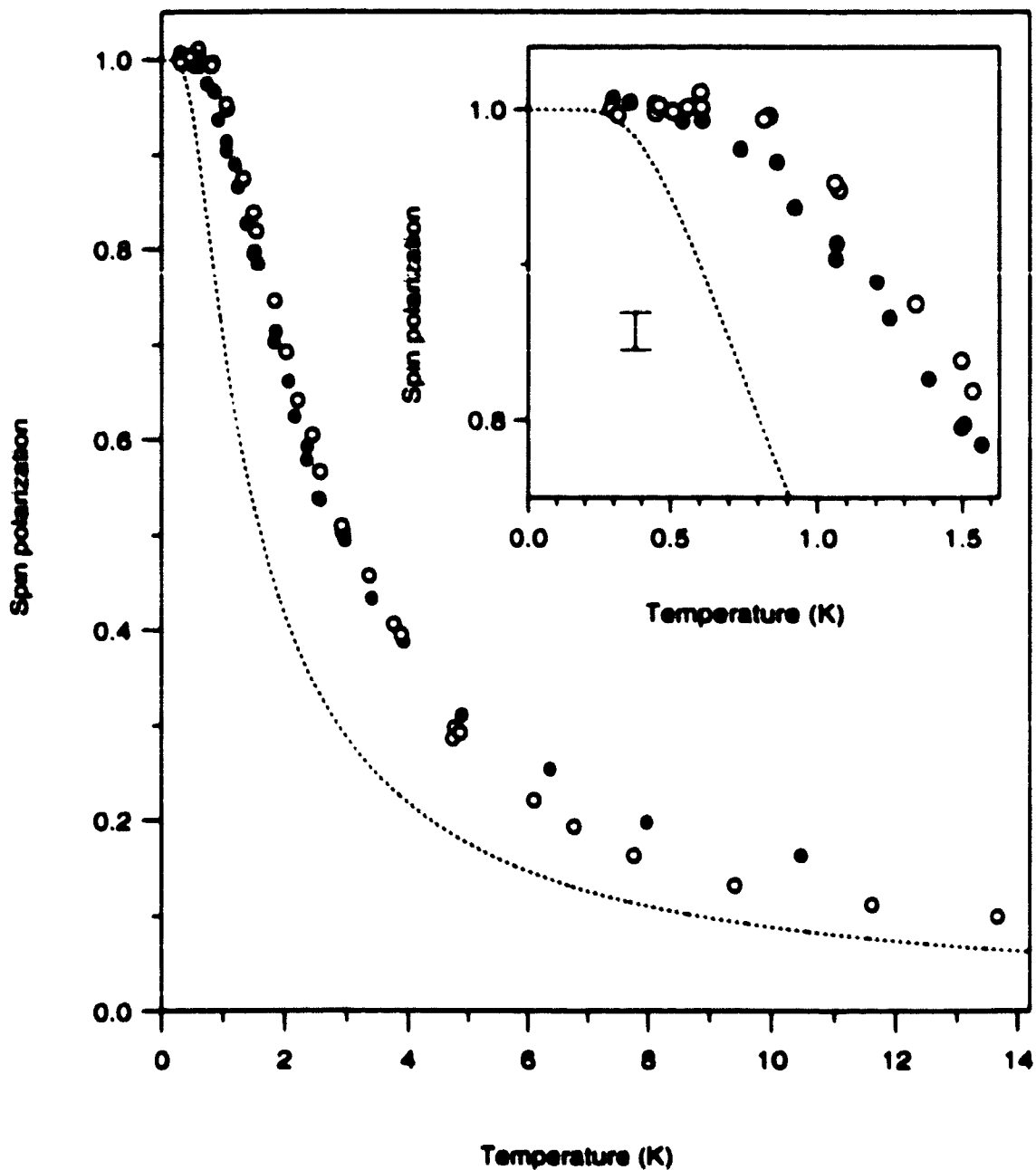


Figure 5.9: Temperature dependence of the electron spin polarization \mathcal{P} for samples 10W (open circles) and 40W (filled circles), obtained from the $K_x(T)$ data (Fig. 5.8) at $\nu = \frac{1}{3}$ (with $B_{\text{tot}} = 12$ T, $\theta_{40W} = 46.4^\circ$, and $\theta_{10W} = 36.8^\circ$). The dashed line is $\mathcal{P}^*(T) = \tanh(E_g/4k_B T)$. The inset shows the saturation region (note the error bar).

Table 5.1: Saturated low-temperature values of $K_S(T)$ and related parameters for the two samples.

Sample	Saturated Knight shift $K_S(T \rightarrow 0)$ (kHz)	Sat. intrinsic Knight shift $K_{sim}(T \rightarrow 0)$ (kHz)	Saturation temperature T_{sat} (K)
40W	9.03	10.12	0.46
10W	11.79	12.88	0.77

spin polarization \mathcal{P} , obtained from the Knight shift data (Fig. 5.8) by using:

$$\mathcal{P}(\nu = \frac{1}{2}, T) = \frac{K_{sim}(T)}{K_{sim}(T \rightarrow 0)} \quad (5.10)$$

where the saturated $K_{sim}(T \rightarrow 0)$ values for each sample are given in Table 5.1. Here the intrinsic Knight shifts $K_{sim}(T)$ were extracted from their corresponding apparent peak-to-peak $K_S(T)$ values using an empirical relationship:

$$K_{sim} = K_S + 1.1 \times \{1 - \exp(-K_S/2.0)\} \quad (\text{all in kHz}) \quad (5.11)$$

The resulting polarization curves $\mathcal{P}(T)$ are almost identical for the two samples (Fig. 5.9), although they were obtained with quite different tilt angles and electron densities. The subtle differences that remain may be due to the slightly higher spin stiffness [53] expected for sample 10W as compared to 40W.

The electron spin polarization $\mathcal{P}(\nu = \frac{1}{2}, T)$ data in Figure 5.9 probe the neutral spin-flip excitations of a fractional quantum Hall ferromagnet. For comparison, the dashed line is the polarization $\mathcal{P}^*(T)$, calculated for *non-interacting* electrons at $\nu = 1$.

using:

$$\mathcal{P}^*(T) = \tanh \frac{E_Z}{4k_B T} . \quad (5.12)$$

where the Zeeman energy is $E_Z = g^* \mu_B B_{tot}$ for the magnetic field $B_{tot} = 12$ T and the bulk value of electron g -factor for GaAs is $g^* = -0.44$. Both $\mathcal{P}(\nu=1, T)$ measured earlier [26, 29] and $\mathcal{P}(\nu=\frac{1}{3}, T)$ reported here saturate at higher temperatures than $\mathcal{P}^*(T)$, although the data at $\nu=\frac{1}{3}$ lie much closer to this $\mathcal{P}^*(T)$ limit.

Fitting $\tanh(\Delta/4k_B T)$ to the saturation region of our $\mathcal{P}(T)$ data results in the value of $\Delta \approx 2E_Z$ at $\nu=\frac{1}{3}$, as opposed to $\Delta \approx 10E_Z$ at $\nu=1$ [26], so that the Zeeman gap appears to be much less enhanced at $\nu=\frac{1}{3}$ than it is at $\nu=1$. We also note that the 40W data set is very well described by $\Delta = 1.82E_Z$ (the curve is not shown in Fig. 5.9) over the *entire* temperature range, in sharp contrast to the behavior at $\nu=1$. These results are consistent with the spin stiffness being much less at $\nu=\frac{1}{3}$ compared to $\nu=1$ [53]. While a recent numerical result [54] is in qualitative agreement with the data in Figure 5.9, it remains to be seen how other theoretical approaches, such as those used at $\nu=1$ [32, 33, 34], can be modified to explain the above features of the data.

5.4.2 Charged Quasiparticles: $K_S(\nu)$ Data around $\nu=\frac{1}{3}$

The Knight shift was also measured at fixed temperature as a function of sample tilt angle θ , in the total magnetic field of $B_{tot} = 12$ T. Figure 5.10(a) shows $K_S(\nu)$ dependence near $\nu=\frac{1}{3}$ for sample 10W at $T = 0.77$ K, and for sample 40W at $T = 0.46$ K. By these low temperatures, $K_S(\nu=\frac{1}{3}, T)$ has essentially saturated for both samples (see inset in Fig. 5.8). The data in Figure 5.10(a) show that $K_S(\nu)$ drops on either side of $\nu=\frac{1}{3}$, a result that is reminiscent of a ‘‘Skyrminion peak’’ seen in the earlier measurements [26] near $\nu=1$.

The $K_S(\nu)$ feature near $\nu \sim \frac{1}{3}$ is distinctly ‘‘sharper’’ for sample 10W as opposed

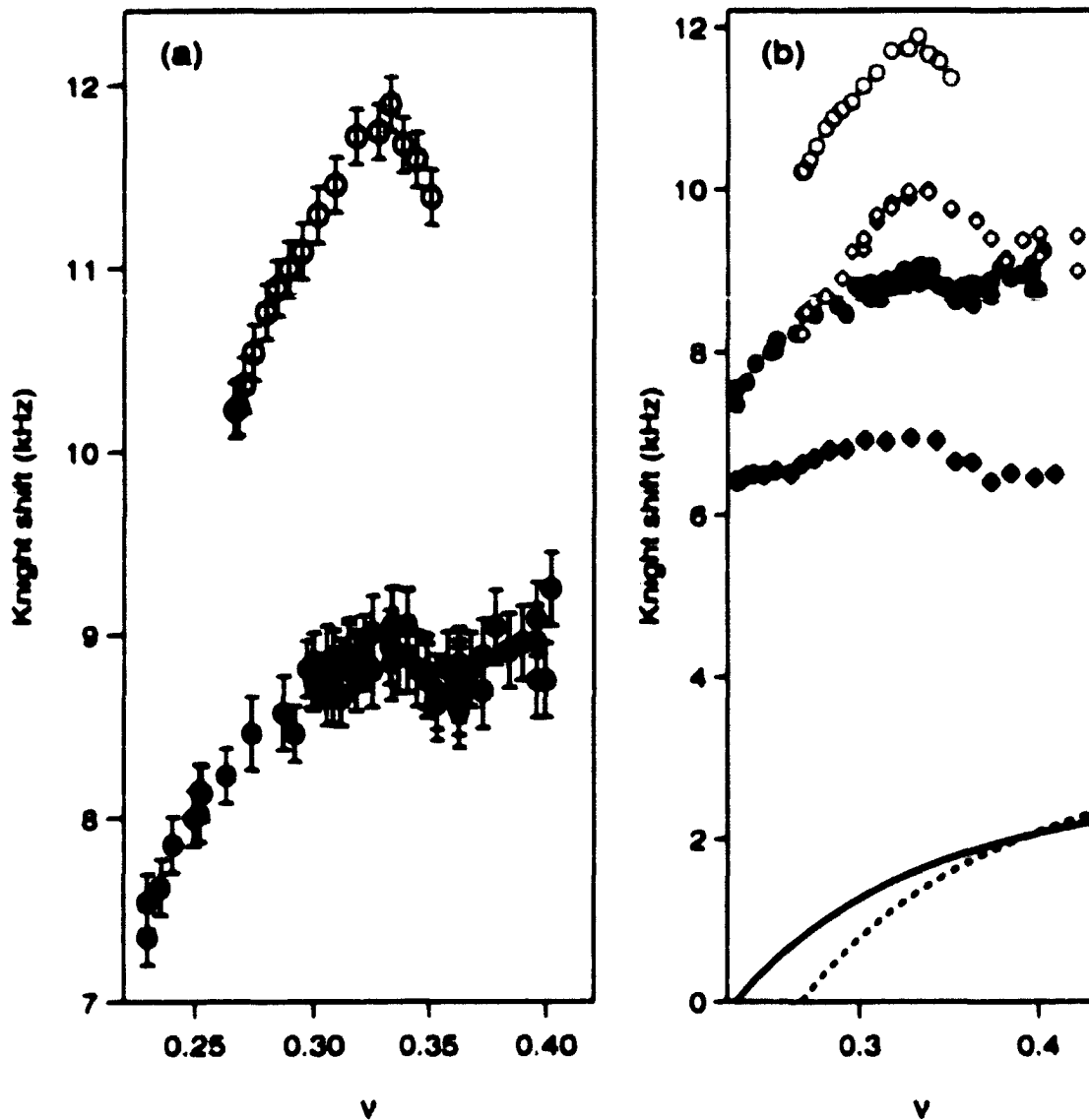


Figure 5.10: Dependence of the Knight shift K_N on the filling factor ν at a fixed temperature, measured in: sample 10W at $T=0.77$ K (open circles*); sample 40W at $T=0.46$ K (filled circles*); samples 10W and 40W at $T=1.5$ K (open and filled diamonds). For samples 40W and 10W, solid and dashed lines show the tilt-dependent effect of a paramagnetic rotation stage on the NMR frequencies, which had to be taken into account in order to obtain the Knight shift from the "W" peak frequency correctly.

* Same data is shown in (a) as in (b), but on a finer K_N scale.

to sample 40W. This difference between the samples is not an artifact of the temperatures plotted, as Figure 5.10(b) shows that the distinction is already present by $T = 1.5$ K. In order to determine $K_S(\nu)$ self-consistently from the well peak positions, we took into account the *extrinsic* tilt-angle dependence of all NMR frequencies (Fig. 5.10(b), solid and dashed curves) caused by paramagnetic impurities in the brass rotation stage.

The Knight shift data shown in Figure 5.10(a) are converted to the corresponding electron spin polarization \mathcal{P} by substituting an empirical expression for the intrinsic Knight shift K_{sim} (Eq. 5.11) into:

$$\mathcal{P}(\nu) \equiv \frac{K_{sim}(\nu)}{K_{sim}(\nu = \frac{1}{3})} \quad (5.13)$$

The resulting $\mathcal{P}(\nu)$ dependence is plotted in Figure 5.11. It can be seen that the electron spin polarization in both samples decreases as ν is varied away from $\frac{1}{3}$, despite the presence of the 12 T field! Perhaps even more remarkably, $\mathcal{P}(\nu)$ decreases monotonically as ν is lowered below $\frac{1}{3}$ over the observed range ($\frac{\nu}{\frac{1}{3}} \sim -30\%$). This strongly suggests that the charged excitations (quasiparticles at $\nu > \frac{1}{3}$ and quasiholes at $\nu < \frac{1}{3}$) of the $\nu = \frac{1}{3}$ ground state involve electron spin flips, that lead to the observed partial depolarization of the 2DES.

A second, independent measurement supports this conclusion. Figure 5.13 in the next section shows a dramatic increase in the OPNMR linewidth as the filling factor is varied away from $\nu = \frac{1}{3}$ (spectra of sample 10W at $T \approx 0.46$ K are shown). While the spectra at higher temperatures are "motionally narrowed" [6], the dramatic broadening of the line shape at $\nu < \frac{1}{3}$, $T \approx 0.5$ K provides evidence that the time-averaged local values of electron spin polarization \mathcal{P}_{loc} are no longer spatially homogeneous. This inhomogeneity requires the existence of spin-reversed regions, that appear to move more slowly at low temperatures. Further details of these measurements will be discussed in sections 5.5 and 5.6 (also reported in publication [49]).

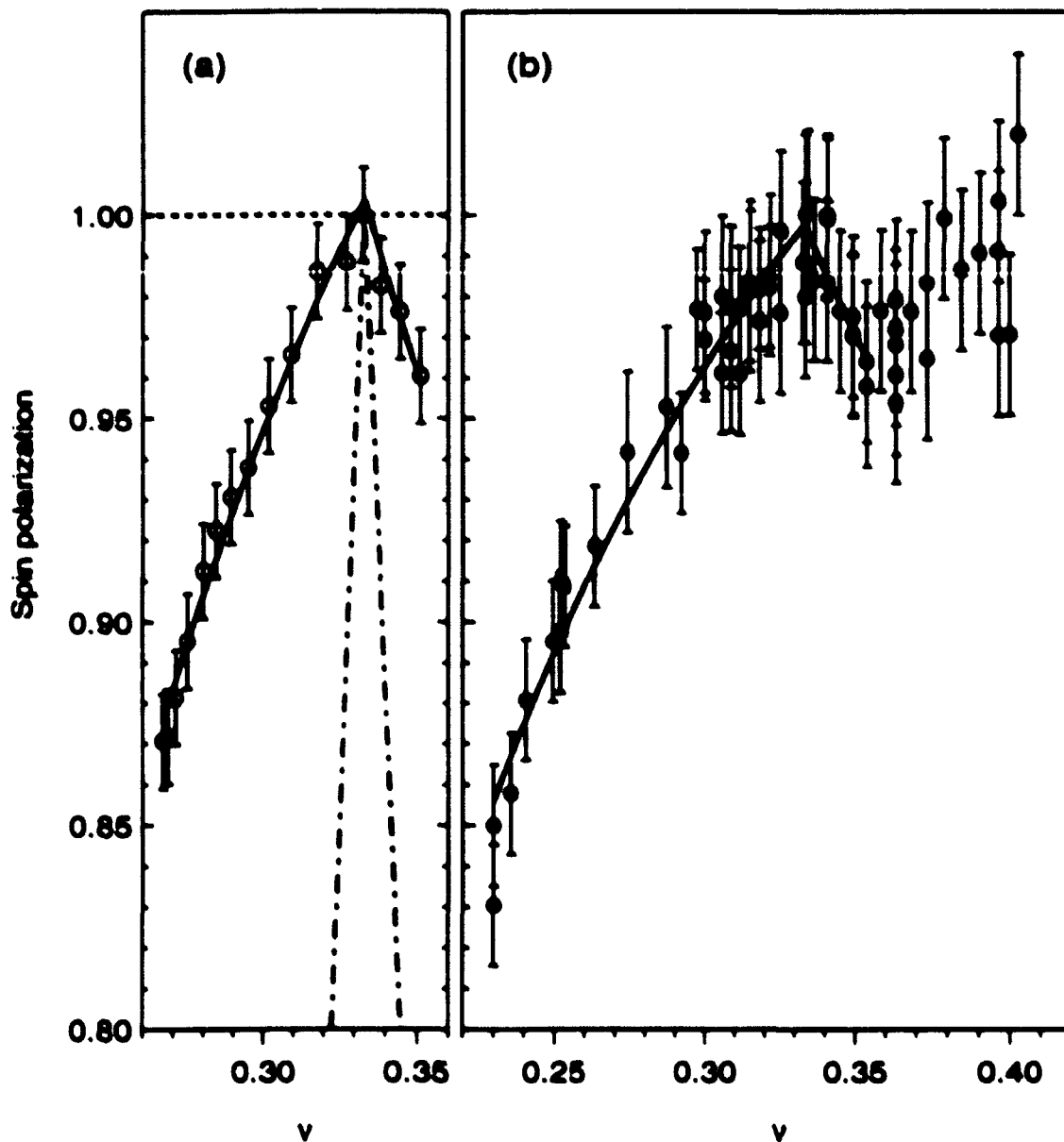


Figure 5.11: Dependence of electron spin polarization \mathcal{P} on the filling factor ν at a fixed temperature. (a) sample 10W: $\mathcal{P}(T)$ data at $T=0.77$ K (open circles); the behavior of our model (Eq. 5.14) at $\nu_e = \frac{1}{3}$ for: $\dot{A}=\dot{S}=0$ (dashed line), $\dot{A}=0.085$ and $\dot{S}=0.15$ (solid line), and $\dot{A}=\dot{S}=1$ (dash-dotted line). (b) Sample 40W: $\mathcal{P}(T)$ data at $T=0.46$ K (filled circles); fits of our model (Eq. 5.14, with $\nu_e = \frac{1}{3}$) to the data, resulting in $\dot{A}=0.053$ and $\dot{S}=0.10$ (solid line).

To quantify the rate of depolarization in Figure 5.11, we extend a simple model previously used [26] near $\nu=1$. Our model parametrizes the effect of interactions in the neighborhood of a ferromagnetic filling factor $\nu_0 < 1$. We assume that adding a quasiparticle (or quasihole) to the ground state causes \dot{S} (or \dot{A}) electron spins to flip. Within this model, the electron spin polarization is:

$$\mathcal{P}(\nu) = 1 + 2\left(\frac{1}{\nu} - \frac{1}{\nu_0}\right)\left(\dot{S}\Theta(\nu - \nu_0) - \dot{A}\Theta(\nu_0 - \nu)\right), \quad (5.14)$$

where the Heavyside step function is $\Theta(x) \equiv \{1 \text{ for } x \geq 0; \text{ and } 0 \text{ for } x < 0\}$. This form is simply a pair of straight lines in the $(\mathcal{P}, 1/\nu)$ plane, corresponding to the constant amount of spin reversal per each new quasiparticle (quasihole) added. Using Eq. (5.14) to fit the data near $\nu_0 = \frac{1}{3}$ (Fig. 5.11, solid lines), we find:

$$\begin{aligned} \text{Sample 10W: } \dot{A} &= 0.085 \pm 0.005, \quad \dot{S} = 0.15 \pm 0.04; \\ \text{Sample 40W: } \dot{A} &= 0.053 \pm 0.008, \quad \dot{S} = 0.10 \pm 0.03. \end{aligned} \quad (5.15)$$

For comparison, the earliest theory [3, 4] of the $\nu=\frac{1}{3}$ ground state assumed fully spin-polarized quasiparticles and quasiholes, i.e., $\dot{S}=\dot{A}=0$ (Fig. 5.11, dashed line). Subsequent calculations [5] considered the possibility of spin-reversed quasiparticles and quasiholes, i.e., $\dot{S}=\dot{A}=1$ (Fig. 5.11, dash-dotted line). However, both the early calculations and the more recent theoretical studies [55, 56] of skyrmion excitations near $\nu=\frac{1}{3}$ suggest $\dot{S}=\dot{A}=0$ for strong magnetic fields. On the other hand, our small but non-zero values are within the bounds set by transport measurements at ambient [57] and high [58] pressures.

A much more difficult feature to understand is the fact that our measured values are fractional ($\dot{S} \sim \dot{A} \sim 0.1$), since the electron spin (S_z) must be a good quantum number [5]. Of course, our experiment does not have the resolution to see the effect of adding a single quasiparticle to the $\nu=\frac{1}{3}$ ground state, thus these values for \dot{S} and \dot{A} are the average numbers of flipped spins per quasiparticle and quasihole.

Nevertheless, Equation 5.14, which assumes that all quasiholes (or quasiparticles) behave in exactly the same way¹⁸, does a remarkably good job fitting our data over the range of filling factors ($0.23 < \nu < 0.36$). This model is expected to break down outside the “dilute” quasiparticle limit (i.e., when the filling factor gets “too far” from $1/3$), since our fitting parameters \hat{S} and \hat{A} are independent of ν . Surprisingly, the above fit actually passes through $\nu=2/7$ without modification. High field, low-temperature ($T = 300$ mK) magnetotransport measurements [38, 59] on samples taken from the same wafer as 10W show much more structure, with well-developed ρ_{xx} minima at $\nu = 1/3, 2/5, 2/7,$ and $1/5$.

The possible explanations of these values ($\hat{S} \sim \hat{A} \sim 0.1$) are constrained by many different aspects of the data. For example, motional narrowing of the NMR lineshape at higher temperatures requires that the time-averaged electron spin polarization to be spatially uniform for all ν . Furthermore, the values of \hat{S} and \hat{A} do not appear to change from $T=0.5$ K to $T=1.5$ K, although we do observe an $\sim 80\%$ drop in the overall spin polarization.

5.5 Broadening of the OPNMR Lineshape at $\nu < \frac{1}{3}$

In all of the measurements reported so far, the OPNMR spectra were well described by the dashed line fits of Eq. 5.4, generated within the model which was introduced in section 5.2. The central assumption of this model is that the electron spins are

¹⁸i.e. on average, each additional quasiparticle or quasihole leads to the same (fractional) amount of spin reversal, regardless of how many excitations have already been added to the system. It can be said that these are “non-interacting” charged excitations, since their average (fractional) spin does not apparently depend on their density.

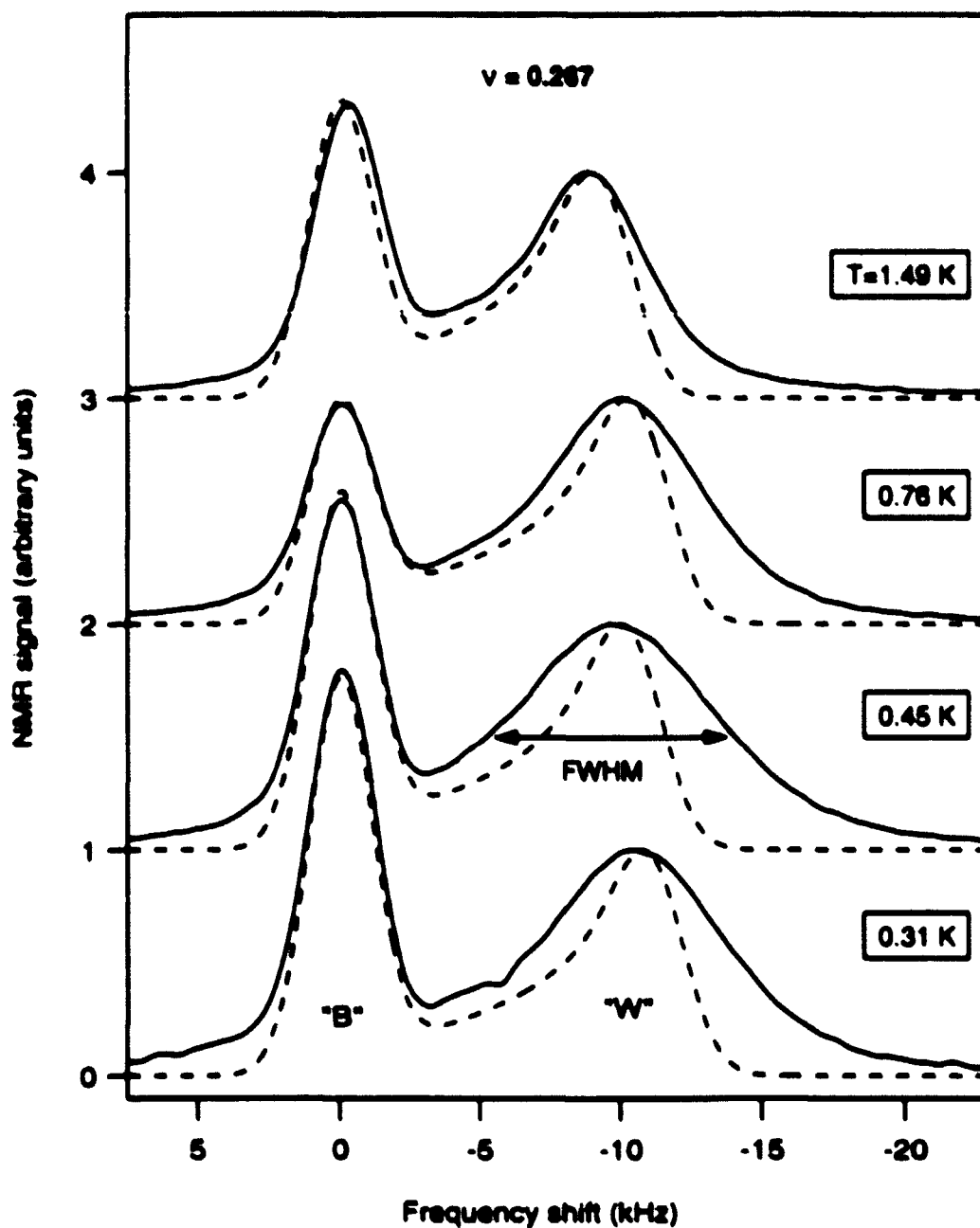


Figure 5.12: Temperature dependence of the ^{71}Ga OPNMR spectra of sample 10W (solid lines) at $\nu = 0.267$ ($\theta = 0^\circ$). The full width at half maximum (FWHM) of the well resonance "W" is shown. Note, that as the temperature is lowered, the "W" peak is broadening beyond the "motionally narrowed" interpretation (dashed line fits of Eq. 5.4), and then is narrowing somewhat again at still lower temperatures (compare the width of "W" peak at 0.31 K to that at 0.45 K).

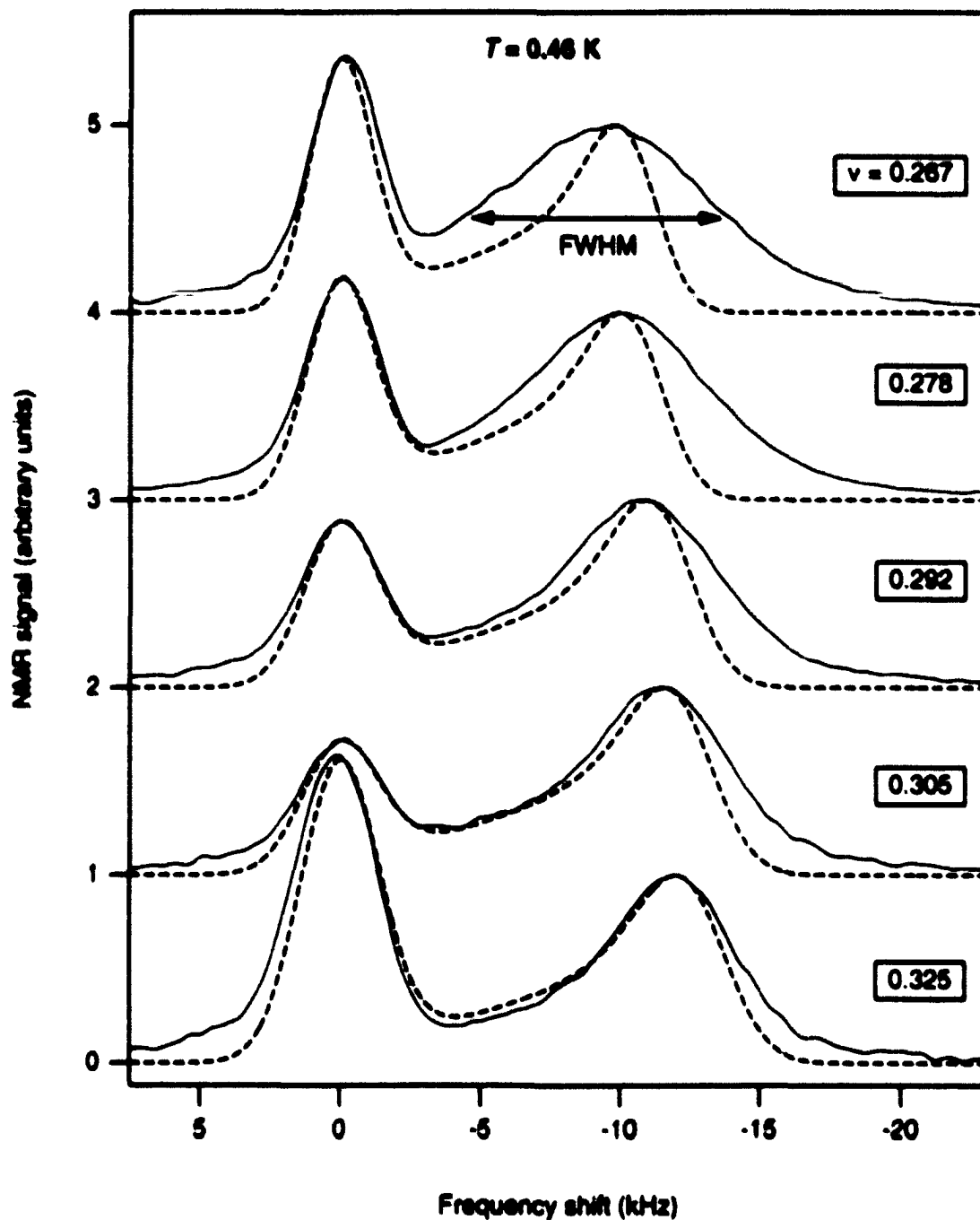


Figure 5.13: ^{71}Ga OPNMR spectra (solid lines) of sample 10W at $T=0.46\text{ K}$, for $0.267 \leq \nu < 1/3$ ($0^\circ \leq \theta < 36.8^\circ$). Note, that as the filling factor ν approaches $1/3$, the spectra converge towards the "motionally narrowed" line shape (dashed lines), given by Eq. 5.4.

delocalized along the well, such that the local values¹⁹ of $\langle S_z(\nu, T) \rangle$ appear spatially homogeneous, when averaged over the NMR time scale²⁰ of $\sim 40 \mu\text{s}$. In this limit, the delocalization of electron spins in the low density²¹ 2DES produces a “motional narrowing” of the OPNMR line shape.

However, as can be seen in Figure 5.12, our low-temperature measurements at $\nu=0.267$ show a crossover to somewhat more complicated line shapes. Although the spectra are in reasonable agreement with our model above 1 K, the width of the “W” peak increases dramatically as the temperature is lowered to $T=0.45$ K and then decreases again upon further lowering to $T=0.31$ K. This remarkable non-monotonic temperature dependence is reminiscent of the behavior seen in NMR studies of systems in which spectra are sensitive to dynamical processes [45], variously referred to in the literature as “motional narrowing,” “dynamical averaging,” or “chemical exchange” [6, 60, 61].

In our experiment, the ^{71}Ga nuclei are rigidly fixed in the lattice of a single crystal, which suggests that the variation in the line shape shown in Figure 5.12 is a signature of electron spin localization. Being temperature-induced, such localization turns off the “motional narrowing” of the well resonance as the sample containing the 2DES is cooled below 1 K.

Figure 5.13 shows that the extra broadening of the well resonance disappears as the sample is tilted from $\theta_{10w} = 0^\circ$ ($\nu = 0.267$) to 36.8° ($\nu = 1/3$), despite a 10% in-

¹⁹Here \hat{z} is the direction of the laboratory magnetic field \hat{B}_{ext} , along which the electron spin operator \hat{S}_z is quantized.

²⁰For nuclei in the center of the quantum well, local values of the electron spin polarization P can fluctuate between 1 and -1, resulting in the corresponding NMR frequency variations of $\pm K_{\text{SM}}$. Thus the NMR time scale which separates fast and slow fluctuations is approximately $(2K_{\text{SM}})^{-1} \approx 40 \mu\text{s}$.

²¹There is approximately one electron per 10^6 nuclei the quantum well.

crease in the dipolar broadening²² (compare to similar variation at room temperature, described by Eq. 5.1). Furthermore, there is a striking correspondence between the decrease in the linewidth, plotted in Figure 5.14 (open symbols), and the increase in the measured Knight shift K_S (filled symbols) as the filling factor ν approaches $1/3$. This anticorrelation strongly suggests that the behavior shown in Figures 5.12 through 5.14 is due to electron spin dynamics.

For a quantitative understanding of these phenomena, we must consider the specific assumptions that lead to the motionally narrowed line shape. Nuclei within the quantum well couple to the electron spins of the 2DES through the isotropic Fermi contact interaction [6, 9, 26, 27, 48]. Thus a nucleus at site \mathbf{R}'_i experiences a hyperfine magnetic field:

$$\mathbf{B}^*(\mathbf{R}'_i) = -\frac{16\pi}{3} \mu_B \sum_j \mathbf{S}_j \delta(\mathbf{r}'_j - \mathbf{R}'_i) \quad (5.16)$$

where μ_B is the Bohr magneton, \mathbf{S}_j is the spin of electron j , the summation runs over all of the conduction electrons within the quantum well, and the delta function guarantees the overlap of the electron wave function with the nucleus located at \mathbf{R}'_i (compare Equation 5.16 above to the "electron-nuclear" Hamiltonian mentioned earlier in section 5.2, Equation 5.3). The average projection of the hyperfine field \mathbf{B}^* , produced by the electron spins, along the laboratory field \hat{B}_{ext} may be written quite generally as:

$$\langle \mathbf{B}^*(\mathbf{R}'_i, \nu, T) \rangle = -\frac{8\pi}{3} \frac{\mu_B n}{u} |\langle \psi^{\uparrow} u(0) \rangle|^2 |\chi(Z'_i)|^2 |\phi(X'_i, Y'_i)|^2 \mathcal{P}(\mathbf{R}'_i, \nu, T) \quad (5.17)$$

Here²³, the probability density of finding electrons at a ^{71}Ga site i has been factored into a term $|\langle \psi^{\uparrow} u(0) \rangle|^2$ with the periodicity of the lattice and terms $|\chi(Z'_i)|^2 |\phi(X'_i, Y'_i)|^2$

²² The ^{75}As nearest-neighbors of the ^{71}Ga nuclei are at the "magic angle" [61] when $\theta_{\text{low}} = 0^\circ$.

²³In this discussion we write the electronic coordinates as (x, y, z) in the laboratory frame (where $\hat{B}_{\text{ext}} \parallel \hat{z}$), or as (x', y', z') in the sample frame (where z' is the growth direction). Similarly, nuclear coordinates are represented by (X, Y, Z) and (X', Y', Z') in those two frames.

which vary slowly over a unit cell [50].

In Equation 5.17, $\mathcal{P}(\mathbf{R}', \nu, T)$ is the local spin polarization²⁴ ($-1 < \mathcal{P} < 1$) of the electrons at \mathbf{R}' . If we assume that electrons are delocalized along the quantum well, then the time-averaged values of $|\phi|^2$ and \mathcal{P} should be spatially homogeneous. In this limit, the local hyperfine frequency shift f (taken to have the sign of \mathcal{P}) is a function of z' only:

$$f(z') = -\frac{\gamma_n}{2\pi} \langle \hat{B}_z(z', \nu, T) \rangle \approx K_{\text{sim}} \cos^2\left(\frac{\pi z'}{w}\right) \quad (5.18)$$

(see Figure 5.5(c)), and the general expression for the intrinsic well signal intensity (such as shown in Fig. 5.5(e)) can be written as:

$$I_{\text{well}}(f') = \sum_{\text{N-wells}} \int d^3\mathbf{r}' \langle \hat{I}_z(z') \rangle \rho_{\text{nuclear}} \delta(f' - f(z')) \quad (5.19)$$

where $\langle \hat{I}_z(z') \rangle$ is the local spin expectation value for ^{71}Ga nuclei, ρ_{nuclear} is their number per unit volume, the summation is over the number of wells N -wells, and the integral is over the volume of each well.

We further assume that the quantum wells are identical, and that the optical pumping gives rise to a nuclear polarization that varies across each quantum well (see Fig. 5.5(d)) as the first power of $f(z')$. Taken together, these assumptions lead to the intrinsic OPNMR well line shape of the form $I_{\text{well}}(f) = \sqrt{f/(K_{\text{sim}} - f)}$ (shown in Fig. 5.5(e)), which was used in all “motionally narrowed” dashed line fits (see Figures 5.4, 5.7, 5.12, and 5.13) of Equation 5.4.

The observed broadening of the well line shape beyond the “motionally narrowed” limit implies that the time-averaged value of the product $|\phi|^2 \mathcal{P}$ becomes spatially inhomogeneous. Although the $|\phi(X'_i, Y'_i)|^2$ term could become inhomogeneous if a pinned Wigner crystal were to form, the corresponding increase in the quantum well

²⁴As defined in Eq. 5.6, \mathcal{P} can only change from -1 (all spins pointing down) to 1 (all spins pointing up).

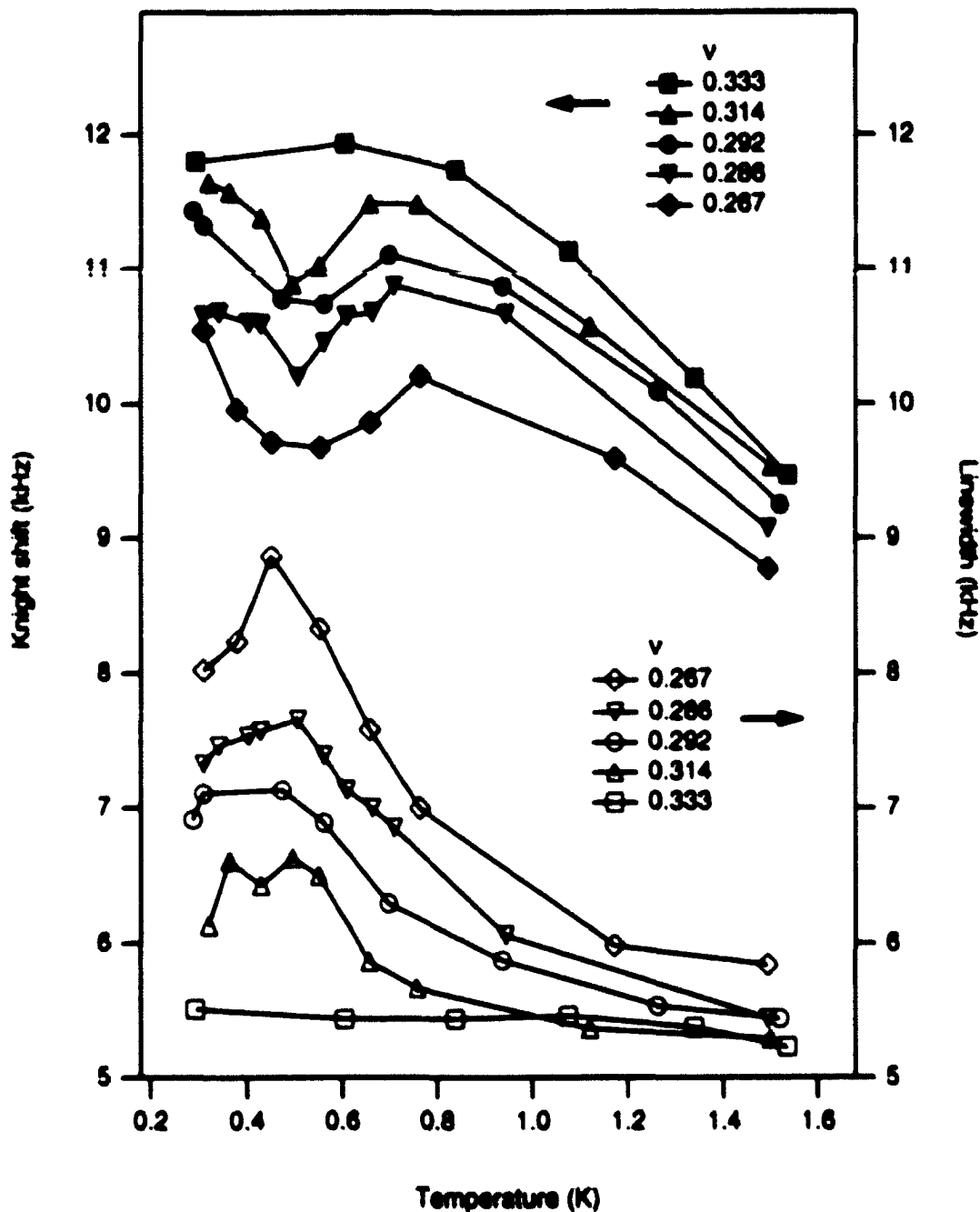


Figure 5.14: The temperature dependence of the Knight shift (filled symbols) and the linewidth (open symbols) for several filling factors $0.267 \leq \nu \leq 1/3$ in sample 10W. Lines are to guide the eye.

linewidth (by orders of magnitude) and the concomitant drop in the peak intensity are not observed.

Furthermore, variations in charge density along the well (for example, arising from fluctuations in the dopant layer) do not appear to explain either the magnitude of the effect²⁵ or the non-monotonic temperature dependence. On the other hand, the Knight shift data show that the total spin polarization drops monotonically as the filling factor is lowered below $\nu = \frac{1}{3}$, allowing the local spin polarization $\mathcal{P}(\mathbf{R}_i')$ to be spatially inhomogeneous at $\nu < \frac{1}{3}$. Thus we conclude that localization of spin-reversed regions is responsible for the behavior shown in Figures 5.12 to 5.14.

5.6 Break-Down of Motional Narrowing

The time scale of the spin localization may be inferred by simulating the observed line shapes.

We propose a simple bipolar model, which illustrates the effect. For every nuclear site (X_i', Y_i') along the plane of the well the local electron spin polarization \mathcal{P} is assumed to be either completely "up" ($\mathcal{P}_+ = 1$) or partially "down" ($\mathcal{P}_- = -0.15$). This simulation corresponds to the case of partially depolarized regions that move around along the quantum well through a fully polarized background. The speed of such motion can be modeled by introducing a time scale over which a given nucleus can become exposed to either a depolarized region or the fully polarized background. In our simulation, we introduce a characteristic "jump time" interval τ_j . After each such time interval, the local polarization at each site instantaneously (and independently from other sites) takes on either the \mathcal{P}_+ or \mathcal{P}_- value with the corresponding probability

²⁵In simulations, we found that an unreasonably large FWHM of 35% is required for a Gaussian distribution of electron densities along the well to explain the maximum NMR linewidth observed at $\nu = 0.267$.

p_+ or $(1-p_+)$. As a result, at all times the ratio of “up” to “down” sites on the average is $p_+/(1-p_+)$.

Within this model we proceed to calculate the OPNMR line shape for a given fixed value of τ_j . The nuclear ^{71}Ga system was represented by 7997 spins²⁶, distributed across the width w of the quantum well from $Z' = -w/2$ to $Z' = w/2$ with the density proportional to $\cos^2(\pi Z'/w)$, consistent with the tendency of optical pumping to preferentially polarize nuclei near the center of the well (see Fig. 5.5(d)). Each ^{71}Ga spin i was assumed to precess independently from others with its own time-dependent intrinsic frequency:

$$f_i(t) = \mathcal{P}_i(t) K_{\text{sim}}^{\text{max}} \cos^2(\pi Z'_i/w), \quad (5.20)$$

where $K_{\text{sim}}^{\text{max}} = 12 \text{ kHz}$ (appropriate for sample 10W), and the time-dependent $\mathcal{P}_i(t)$ was randomly assigned the values of \mathcal{P}_+ or \mathcal{P}_- (with corresponding probabilities of p_+ and $1-p_+$) for a given nucleus i at the beginning of each interval τ_j . Otherwise $\mathcal{P}_i(t)$ was kept constant between the jumps. Equation 5.20 was then integrated for each nucleus to obtain its precession angle:

$$\Omega_i(t) = \int_0^t 2\pi f_i(t') dt'. \quad (5.21)$$

so that its contribution²⁷:

$$M_i = M_0 \exp(-i \Omega_i(t)) \quad (5.22)$$

to the total free induction decay (FID) could be calculated. The resulting total intrinsic signal $M_{\text{FID}}(t) = \sum_i M_i(t)$ was then Fourier transformed to obtain the spectrum $I_{\text{FID}}(f)$ in the frequency domain, and finally convoluted with a 3.5 kHz Gaussian that took into account the dipolar broadening.

²⁶This number resulted from binning the nuclei in the frequency domain using the “intrinsic line shape” distribution (the I_0 term in Eq. 5.4).

²⁷Here $-i = -\sqrt{-1}$ should not be confused with the nuclear index i .

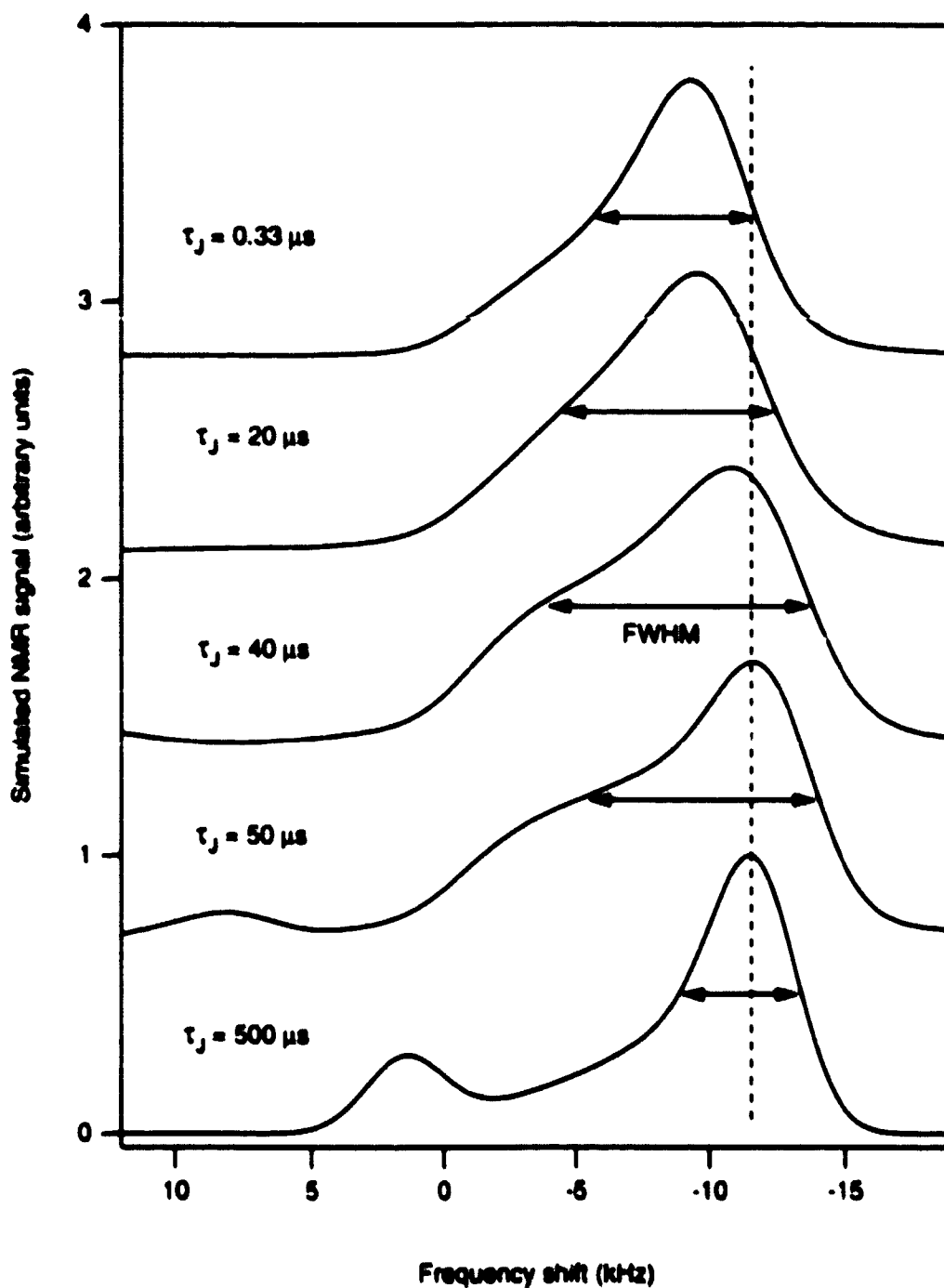


Figure 5.15: Simulated OPNMR spectra, calculated using a bipolar model of transition from motional narrowing (high temperatures, fast τ_j) to the frozen limit ($T \rightarrow 0$, long τ_j), which may be compared to spectra in Fig. 5.12. In calculations, K_{rot} was set to 12 kHz for $P = 1$, and the barrier was suppressed ($a_6 = 0$ in Eq. 5.4) for clarity.

Figure 5.15 shows how the simulated OPNMR spectra depend upon the jump interval τ_j , for the case of $p_+ = 0.85$. The simulation is in reasonable agreement with the corresponding data from sample 10W (see Fig. 5.12). When τ_j is very fast, all nuclei see the same time-averaged local polarization, equal to the global polarization:

$$\langle \mathcal{P}_{\text{local}} \rangle_t = p_+ \mathcal{P}_+ + (1 - p_+) \mathcal{P}_- = \mathcal{P}_{\text{global}} . \quad (5.23)$$

Thus we get $\mathcal{P}_{\text{global}} = 0.828$ for $p_+ = 0.85$, a check that our model parameters are consistent with the measured depolarization at $\nu = 0.275$. At the other extreme of $\tau_j \rightarrow \infty$ the motion is frozen out, and the well resonance is split into “up” and “down” lines, with areas proportional to p_+ and $(1 - p_+)$, respectively (for example, see the $\tau_j = 500 \mu\text{s}$ trace in Fig. 5.15).

Even within this simple bipolar model, the inhomogeneous broadening of the frozen line shape in the direction perpendicular to the plane of the wells (Eq. 5.18) leads to a non-trivial evolution of the spectrum in the intermediate motion regime (for example, a given value of τ_j might be simultaneously “fast” for nuclei at the edge of the well and “slow” for nuclei in the center of the well, depending on the magnitude of the local Knight shifts). In the intermediate motion regime, the width of the “W” peak goes through a maximum when $\tau_j = 40 \mu\text{s}$. Although varying the parameters p_+ and $K_{\text{stat}}^{\text{max}}$ (over the range relevant for samples 10W and 40W) does affect the extreme value of the width, the characteristic τ_j , at which this value occurs, is approximately the same.

Based upon this simple model, the peaks in the line width at $T_{\text{loc}} \approx 0.5 \text{ K}$, shown in Figure 5.14, reflect the localization of reversed spins, such that they fail to cover the sample area uniformly over the time scale of $\sim 40 \mu\text{s}$. The self-similar curves in Fig. 5.14 suggest that temperature T_{loc} , at which the linewidth goes through a maximum, is not a strong function of the filling factor (or, in other words, of the density of reversed spins) for $\nu < 1/3$. Note also that below 0.5 K, the measured

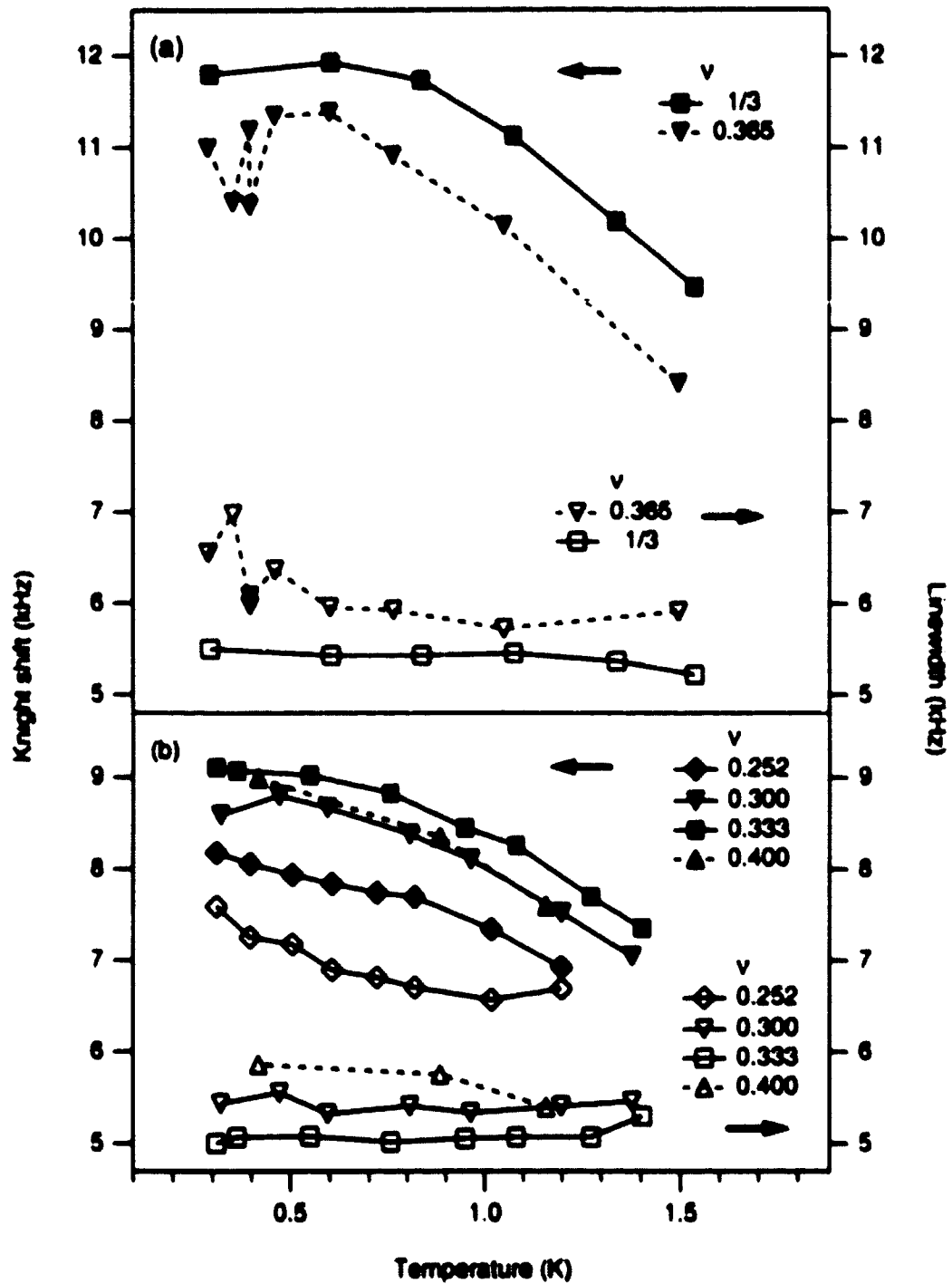


Figure 5.16: The temperature dependence of the Knight shift (filled symbols) and the linewidth (open symbols) for (a) $\nu = 1/3$ and $\nu = 0.365$ in sample 10W, and (b) filling factors $0.252 \leq \nu \leq 0.400$ in sample 40W. Lines are to guide the eye.

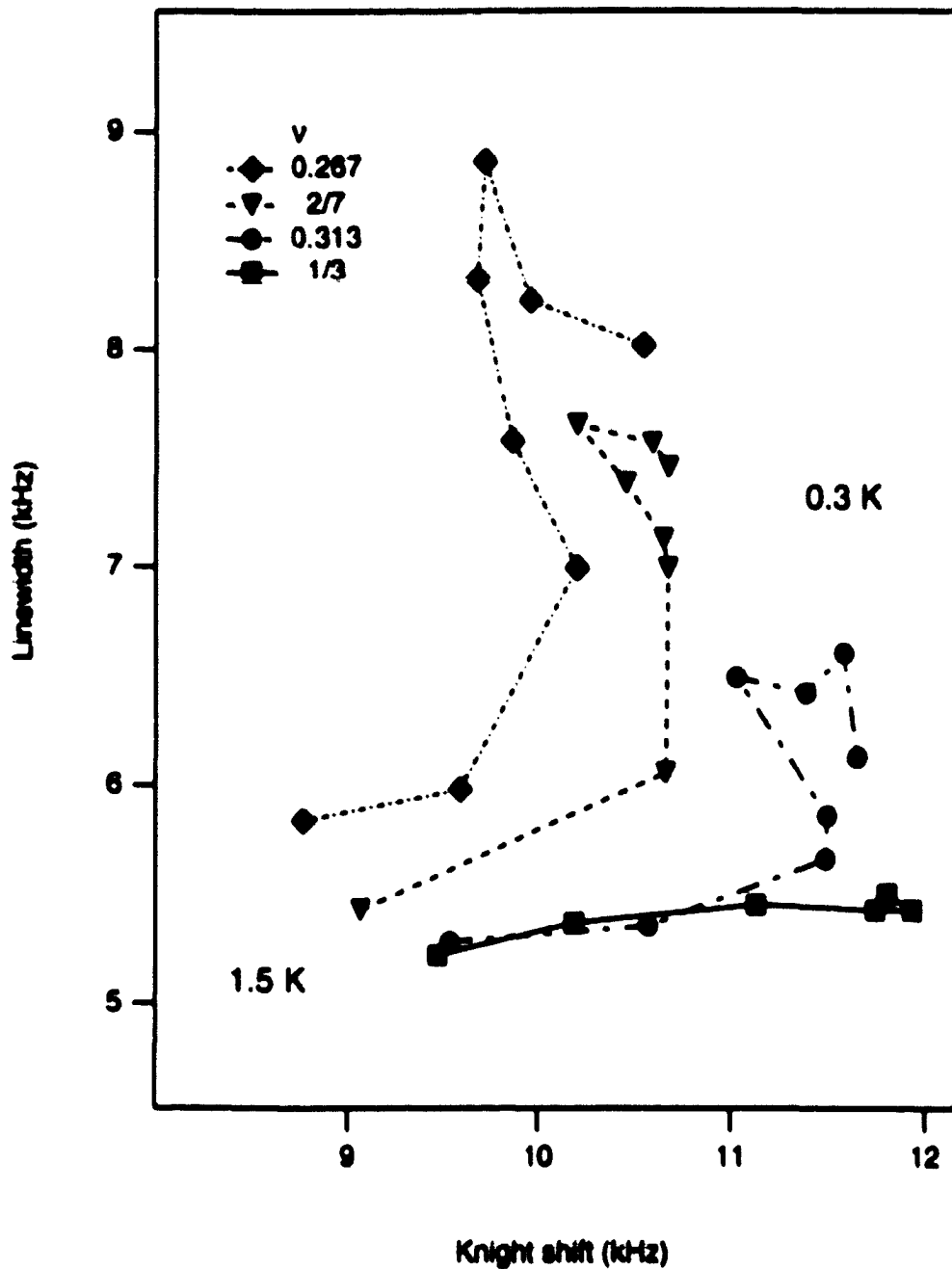


Figure 5.17: Simultaneous evolution of the well linewidth and Knight shift as the temperature of sample 10W is varied from 1.5 K (lower left) to 0.3 K (upper right), for filling factors below $1/3$. Same data as in Fig. 5.14, lines are to guide the eye.

$K_S(\nu < \frac{1}{3})$ increases toward $K_S(\nu = \frac{1}{3})$, as seen in the model. However, even down to the lowest temperatures of $T = 0.3$ K, the spectra do not appear to match the frozen limit of our simulation²⁸.

Surprisingly, as the filling factor is varied below $\nu = 1/3$, the observed trends in the linewidth data (Figure 5.14) continue smoothly through $\nu = 2/7$ without interruption, as is also the case for the Knight shift data. It remains to be reconciled with the fact that magnetotransport measurements on samples taken from the same wafer as 10W show much more structure, including well-developed minima in $\rho_{xx}(B)$ at $\nu = 1/3, 2/5, 2/7,$ and $1/5$ at $T = 0.3$ K [38, 59].

Figure 5.16(a) shows additional measurements of the linewidth for $\nu > 1/3$ in sample 10W, which are consistent with the above picture. Measurements in sample 40W for $\nu \leq 1/3$ are also in qualitative agreement (Fig. 5.16(b)), with one important quantitative difference: the temperature T_{lin} , at which the maximum in the line width is supposed to occur, appears to be shifted lower, so that only the high temperature side of that peak is observed down to the lowest temperatures of $T \approx 0.3$ K. There is a similar sample variation in the saturation temperature (see Table 5.1) of the spin polarization P at $\nu = \frac{1}{3}$, with $T_{10W}^{sat} \approx 0.77$ K and $T_{40W}^{sat} \approx 0.46$ K.

The observed spectra contain more information than our simple bipolar simulation has revealed. A more sophisticated model²⁹ might explain the nontrivial behavior shown in Figure 5.17 and should probably include:

- (i) a detailed structure for the reversed spin regions present below $\nu = 1/3$:

²⁸Unfortunately, the barrier signal (which is not included in the simulated spectra in Fig. 5.15 for clarity) happens near the possible location of the split-off peak (i.e. near +3 kHz), thus masking the effect if such a peak exists at all. If, for example, P_{total} assumes a continuous range of values as opposed to only two (as was the case in our bipolar model), the second "peak" in the frozen limit can look like a trailing tail of the main peak and not develop a maximum at all.

²⁹See, for example, reference [62], where some progress in this direction has been made.

(ii) the 2D dynamics of these reversed spins; and

(iii) the effects of thermally excited spin flips, since the observed T_{out} is not that much greater than the T_{inc} (compare Figures 5.8 and 5.14).

Chapter 6

Non-equilibrium Measurements of Electron Spin Relaxation

6.1 Detection of RF heating

For each of the measurements described in Chapter 5, we applied a weak rf tipping pulse long after laser light was turned off (see Fig. 4.6(a)), in order to probe *equilibrium* properties of the 2DES. In addition, interesting non-equilibrium dynamics of the electron spin system can be studied at low temperatures by varying the parameters of the OPNMR experiment, with a number of remarkable results obtained at $\nu = \frac{1}{4}$.

Chronologically, heating of the electron spin system by rf tipping pulses was first detected as an unfortunate circumstance that interfered with our attempts to make equilibrium Knight shift (K_S) measurements as a function of temperature. In practice, the dependence of K_S values on rf pulse power at low temperatures combined with a “flaky” bistable pulse attenuator led to a mysterious irreproducibility of our data below 0.5 K.

To understand what could go wrong, we set out to measure the Knight shift as a function of all possible OPNMR parameters, such as laser power P_{laser} , optical

pumping time τ_L , dark time τ_D , and also the duration of the rf tipping pulse τ_{pulse} and its magnetic field amplitude H_1 .

A word should be said about measuring H_1 . The rf voltage level V_{rf} in the main NMR cable was monitored on a *Tektronix* digital oscilloscope through a -40 dB *Bird* directional coupler, and the corresponding magnetic field produced by the NMR coil (Fig. 4.8(b)) was estimated¹ as $H_1 = kV_{\text{rf}}$. The constant k was obtained using ^{71}Ga OPNMR in a separate "loop" experiment² [41], in which a series of spectra were acquired as a function of the pulse length τ_{pulse} (as in Fig. 6.1(b)) for a given rf voltage level. The first maximum in the well signal intensity occurs at a value of τ_{pulse} that corresponds to the tipping angle²:

$$\alpha = \frac{1}{2} \gamma_n H_1 \tau_{\text{pulse}} = \frac{\pi}{2} \quad (6.1)$$

from which H_1 for a given rf voltage level can be easily worked out.

Figure 6.1(a) shows a set of OPNMR spectra taken at $T = 0.45$ K as a function of the pulse length at $H_1 = 33$ Gauss, which exhibits a depression in the Knight shift for $\tau_{\text{pulse}} \geq 5 \mu\text{s}$. This effect exhibits a strong dependence on the rf field amplitude, as Figure 6.1(b) demonstrates: at $H_1 = 15.5$ G, only a small deviation of the well peak from its equilibrium position is observed for $\tau_{\text{pulse}} = 30 \mu\text{s}$ (dashed-dotted trace), although the corresponding tipping angle $\alpha = 108^\circ$ is quite large compared to 38° for $\tau_{\text{pulse}} = 5 \mu\text{s}$ at 33 Gauss. Conversely, at fields $H_1 > 33$ Gauss the Knight shift becomes

¹Note, that H_1 could not be calculated directly from the known room-temperature parameters of the components used in our NMR probe, since the incident rf voltage is amplified in the resonant impedance-matched tank circuit by a large factor, which varies widely as the circuit's temperature and the dielectric constant of the helium liquid/gas environment change during the cool-down.

²A factor of $\frac{1}{2}$ here comes from the fact that the linearly polarized field $\vec{H}_1(t) = xH_1 \cos(2\pi f_0 t) = \vec{H}_{\text{left}} + \vec{H}_{\text{right}} = \frac{1}{2}H_1 [x \cos(2\pi f_0 t) + y \sin(2\pi f_0 t)] + \frac{1}{2}H_1 [x \cos(2\pi f_0 t) - y \sin(2\pi f_0 t)]$, produced by the coil, is decomposed into the left- and right-circularly polarized components, only one of which does the "tipping" of nuclei in the rotating frame [6].

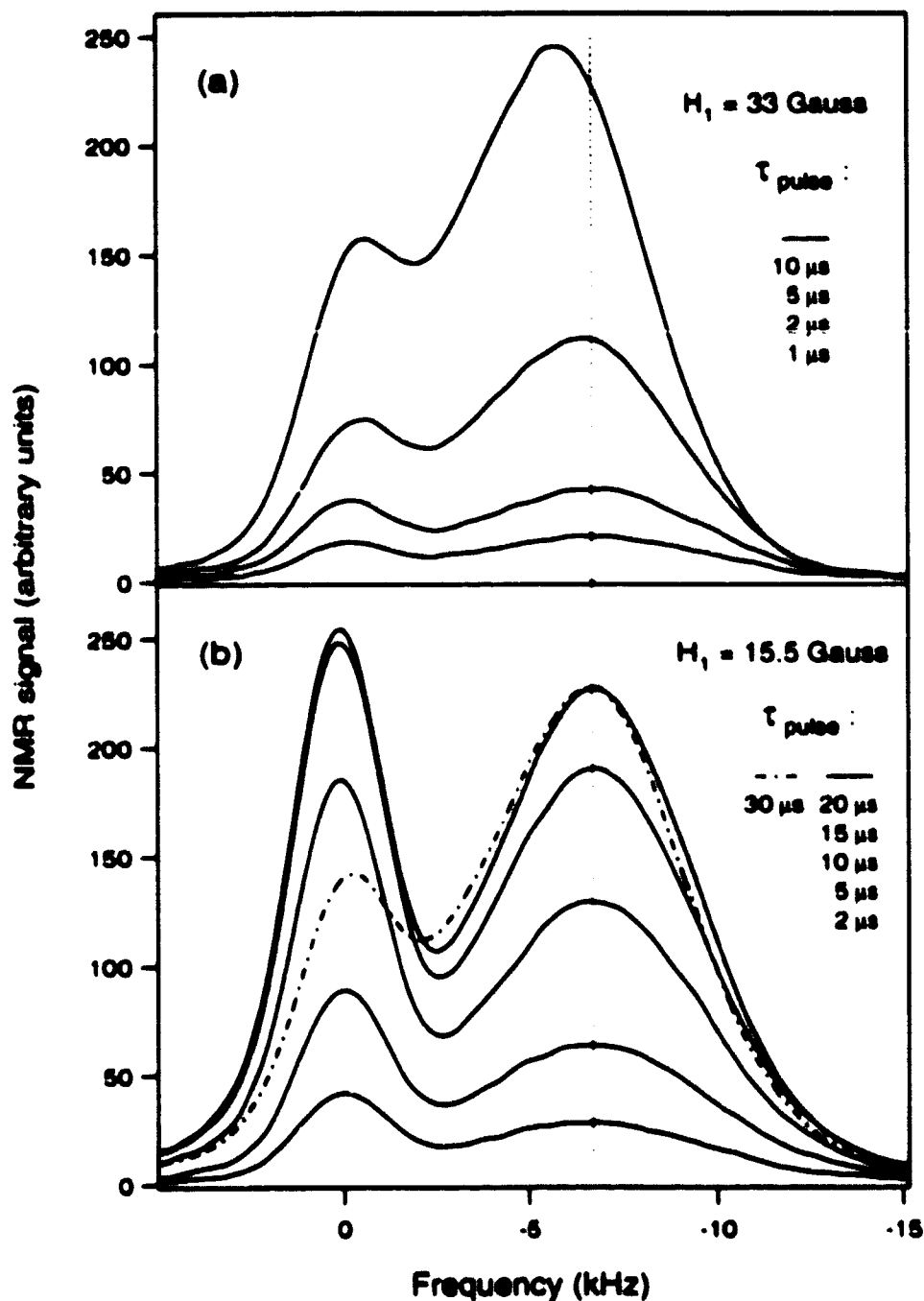


Figure 6.1: ^{71}Ga OPNMR spectra of sample 40W, acquired at $\nu = 0.230$ ($\theta = 0$) with a single rf tipping pulse of amplitude (a) $H_1 = 33$ Gauss and (b) $H_1 = 15.5$ Gauss at $T = 0.45$ K. The duration of the pulse τ_{pulse} is shown for each spectrum. Note that the spectra with similar values of tipping angle $\theta = \frac{1}{2}\gamma H_1 \tau_{\text{pulse}}$ have very different Knight shift in cases (a) and (b). A vertical dashed line marks the frequency of the well peak in the limit of no rf heating.

depressed at even smaller tipping angles. This drop in K_S for large H_1 is similar to the decrease in K_S that occurs in equilibrium as the sample temperature is raised, so we call this effect “rf heating”. Ironically, rf heating has made our efforts to improve the arcing threshold (section 4.3.3) virtually useless, at least as far as the equilibrium OPNMR measurements near and at $\nu = \frac{1}{2}$ are concerned.

6.2 Knight Shift Thermometry of the Electron Spin System

To summarize our observations thus far, we have found that OPNMR spectra can be sensitive to a linearly polarized (perpendicular to both \vec{z} and \vec{B}_{ext}) rf magnetic field of amplitude H_1 , produced at a frequency $f_{\omega} = 155.93$ MHz in the sample coil (Fig. 6.2(c), inset) during the NMR tipping pulse of length τ_{pulse} . Measurements performed with weak pulses (i.e. $H_1 < 14$ Gauss and $\tau_{\text{pulse}} < 20 \mu\text{s}$) yield an OPNMR line shape independent of the tipping pulse parameters (Fig. 6.1), which justifies our use of $H_1 \approx 10$ Gauss and $\tau_{\text{pulse}} = 20 \mu\text{s}$ in the studies of *equilibrium* states, reported in Chapter 5.

If stronger pulses are used at $T < 0.5$ K, the measured Knight shift K_S drops sharply below its equilibrium value, even though the lattice temperature is unaffected by the pulses³. We attribute this drop to an increase in the spin temperature T_{spin} above the lattice temperature T , where T_{spin} characterizes the polarization of the electron spin system.

³Experiments similar to those described in section 4.5 confirm that the sample temperature is not affected by the multiple rf pulses (up to 60 over a 200 ms interval) during the saturation train, even when the highest achievable H_1 levels are used.

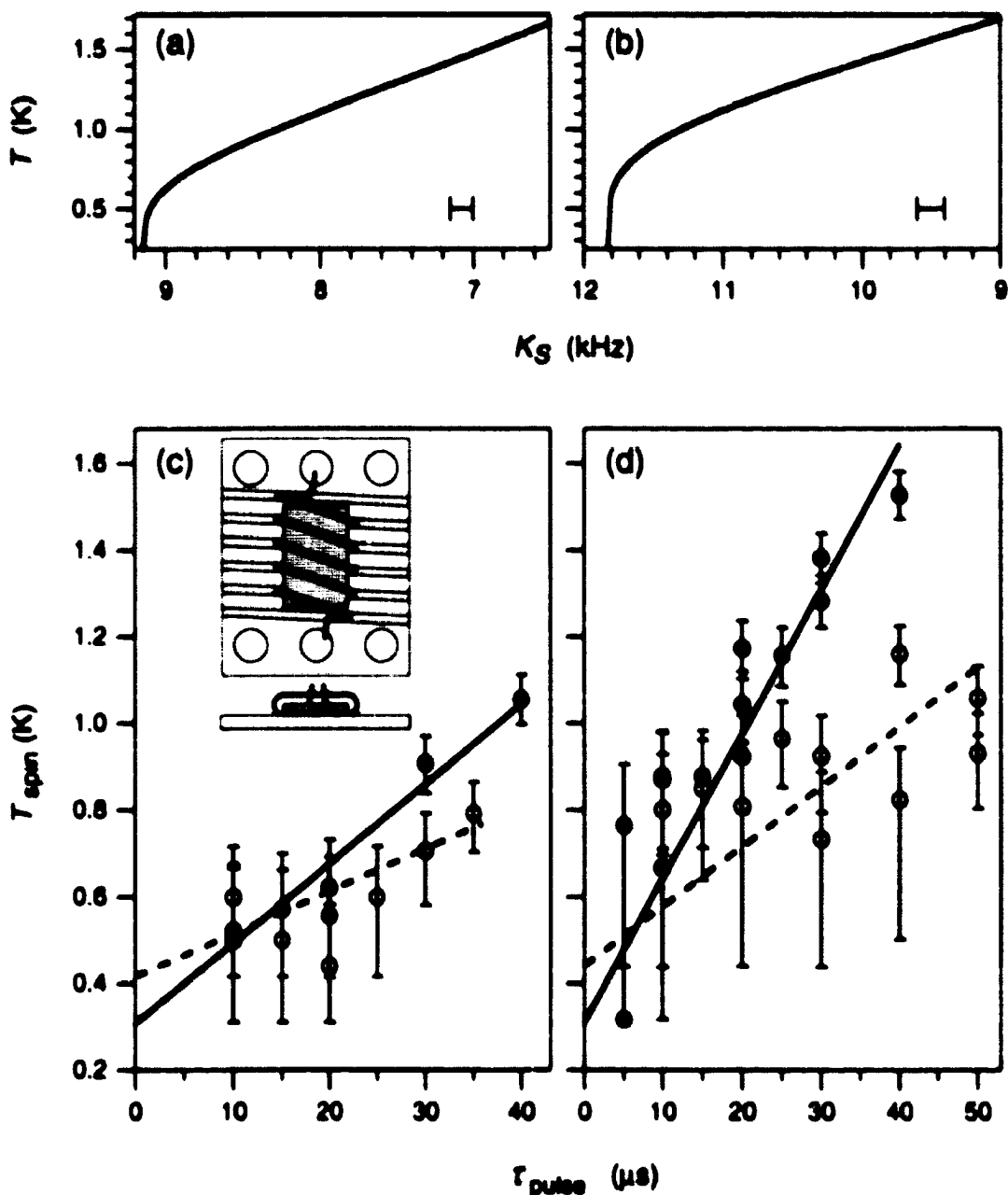


Figure 6.2: Top: $T(K_S)$ calibration curves based on the equilibrium $K_S(T)$ data for (a) sample 40W and (b) sample 10W. Error bars for K_S are shown. Bottom: The dependence of the effective electron spin temperature on the rf pulse length ($H_1 \sim 14$ Gauss) for (c) sample 40W and (d) sample 10W. The intercept of the straight line fit was constrained to be the lattice temperature: $T = 0.31$ K (filled circles 10W and 40W), $T = 0.42$ K (open circles 40W), and $T = 0.44$ K (open circles 10W). The inset shows the top (along \hat{z}') and the front (along the rotation axis) views of the grooved sapphire platform holding a sample in a 5-turn rf coil.

To quantify this phenomenon, we can use the equilibrium $K_S(T)$ data⁴, described in section 5.4.1 and plotted as $T(K_S)$ in Figure 6.2(a,b), to calibrate our non-equilibrium OPNMR line shape, which can be regarded as a “Knight shift thermometer” sensitive to the effective electron spin temperature T_{spin} .

Figure 6.2(c,d) demonstrates the behavior of electron spin temperature T_{spin} (as inferred from the Knight shift data) for the two samples. In both cases, T_{spin} rises linearly above the lattice temperature T as the duration of the tipping pulse τ_{pulse} increases, for $H_1 \sim 14\text{G}$. This observable rise in T_{spin} is sharply reduced as the lattice temperature is increased (compare the solid lines drawn through the $T = 0.31\text{K}$ data to the dashed lines, that correspond to the lattice temperatures of $T = 0.42\text{K}$ and 0.44K for the two samples), and no deviations of the electron spin temperature T_{spin} from the lattice temperature T are observable for $T > 0.5\text{K}$. The large error bars for short τ_{pulse} points are primarily due to the saturation of our “Knight shift thermometer” at low temperatures. Also note, that T_{spin} plotted in Fig. 6.2(c,d) can be up to a factor of 5 higher compared to the corresponding lattice temperature!

6.3 Evidence for Establishment of a Common Electron Spin Temperature

As Figure 6.3 (solid line) illustrates, the non-equilibrium spectra at $\nu = \frac{1}{3}$ remain motionally narrowed, and appear indistinguishable from the corresponding equilibrium spectra (dotted line), measured with a weak tipping pulse at a substantially

⁴In equilibrium, a single temperature characterizes all sub-systems of the sample, i.e. $T = T_{\text{spin}} = T_{\text{lattice}}$.

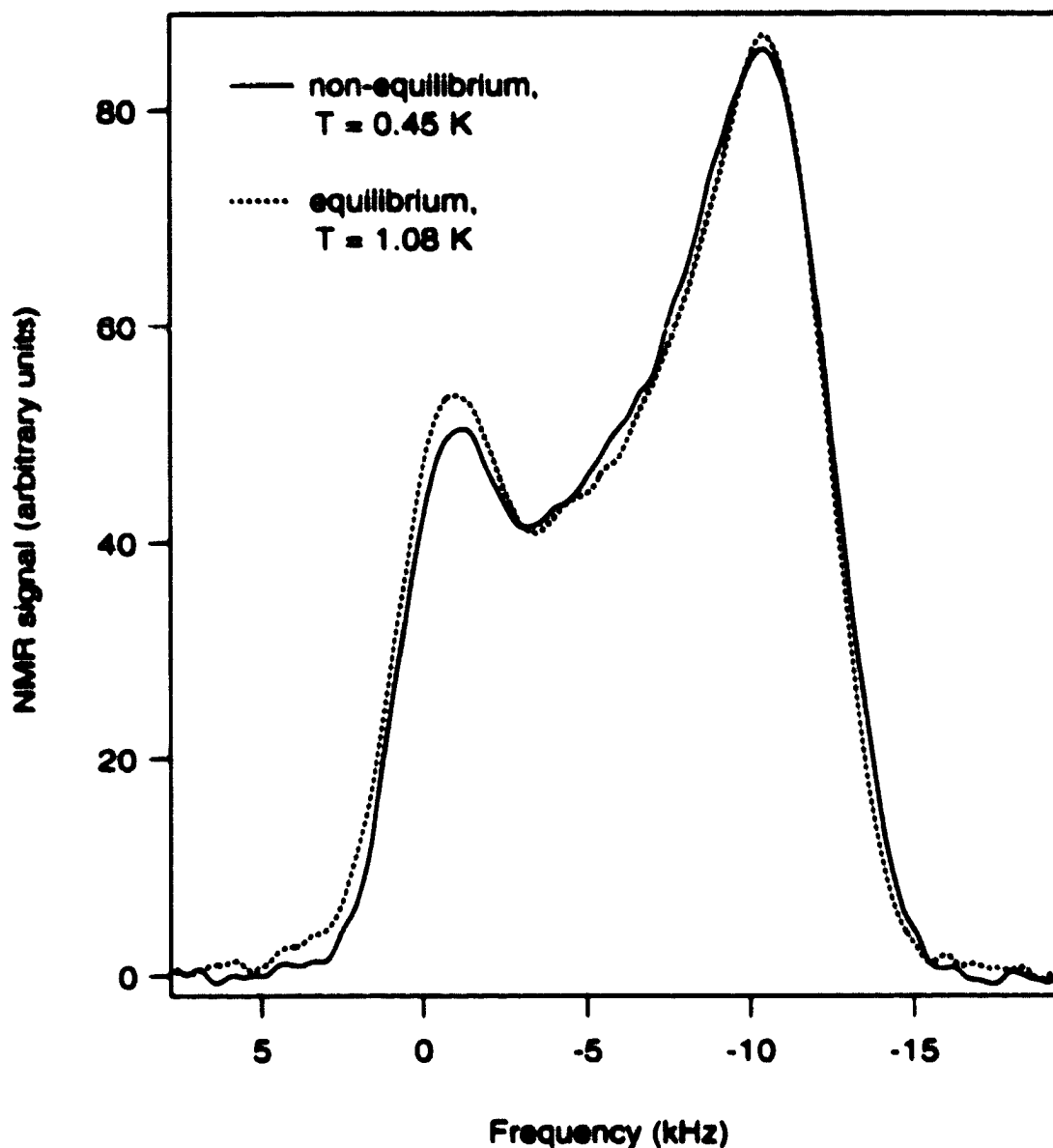


Figure 6.3: ^{71}Ga OPNMR spectra of sample 10W, acquired at $\nu = \frac{1}{3}$ ($\theta = 36.8^\circ$) using identical pumping conditions (laser power $\sim 10\text{ mW}$ at $\lambda = 811.5\text{ nm}$ over $\tau_L = 90\text{ ns}$, followed by $\tau_D = 40\text{ ns}$), but quite different rf pulse parameters and bath temperature: (solid line) $T_{\text{bath}} = 0.45\text{ K}$, $H_1 = 25.5\text{ Gauss}$, $\tau_{\text{pulse}} = 5\text{ }\mu\text{s}$ (tipping angle being $\alpha = 30^\circ$); in contrast with (dotted line) $T_{\text{bath}} = 1.08\text{ K}$, $H_1 = 8.5\text{ Gauss}$, $\tau_{\text{pulse}} = 20\text{ }\mu\text{s}$ ($\alpha = 40^\circ$), the latter corresponding to the “equilibrium” conditions used to obtain $K_S(T)$ data in Fig. 5.8. Remarkable agreement between these spectra provides evidence that the electron spins equilibrate at a common temperature $T_{\text{spin}} > T_{\text{bath}}$ much faster, and relax back to T_{bath} much slower compared to a typical NMR time scale of $100\text{ }\mu\text{s}$.

higher lattice temperature³.

Thus, the electron spin system achieves its internal equilibrium shortly after the tipping pulse, just before the NMR acquisition begins (as is shown schematically in Figure 6.4(a-c)), so that our use of T_{spin} is justified [6]. This can be easily understood, as any possible variations in the local electron spin temperature over the area of the sample would translate into the variations of local Knight shifts, which would in turn lead to an extra inhomogeneous broadening of the OPNMR line shape, something that has never been observed.

However, our measurements also show that the electron spins remain “hot” at a temperature $T_{\text{spin}} > T$ that should be roughly constant long after the rf tipping pulse is turned off (see Fig. 6.4(a,b)): otherwise an extra “dynamical” broadening of the OPNMR line shape would occur due to a temporal variation of Knight shift during the NMR acquisition window (Fig. 6.4(c)). This implies that the longitudinal electron spin-lattice relaxation time $\tau_{1e} > 100 \mu\text{s}$, for the sample lattice temperatures below 0.5 K at $\nu = \frac{1}{2}$.

6.4 Constraints on Possible Heating Mechanisms

The apparent heating depends strongly on the alternating field strength and scales as H_1^η , where the exponent is estimated to be $2 < \eta < 5$. This rules out the coupling to the nuclear spin system as the heat source, since their tipping angle α scales as $H_1 \times \tau_{\text{pulse}}$ (as in Eq. 6.1), while the energy absorbed in a unit volume is given by:

$$\mathcal{E}_n = n_n \mathcal{P}_n \gamma_n \hbar B_{\text{tot}} (1 - \cos \alpha) . \quad (6.2)$$

³At other filling factors (as, for example, in Fig. 6.1), both equilibrium and non-equilibrium spectra broaden at low temperatures due to lack of motional narrowing discussed in sections 5.5 and 5.6. However, even with this complication the “rf-heated” spectra appeared the same as their equilibrium counterparts measured at higher lattice temperatures.

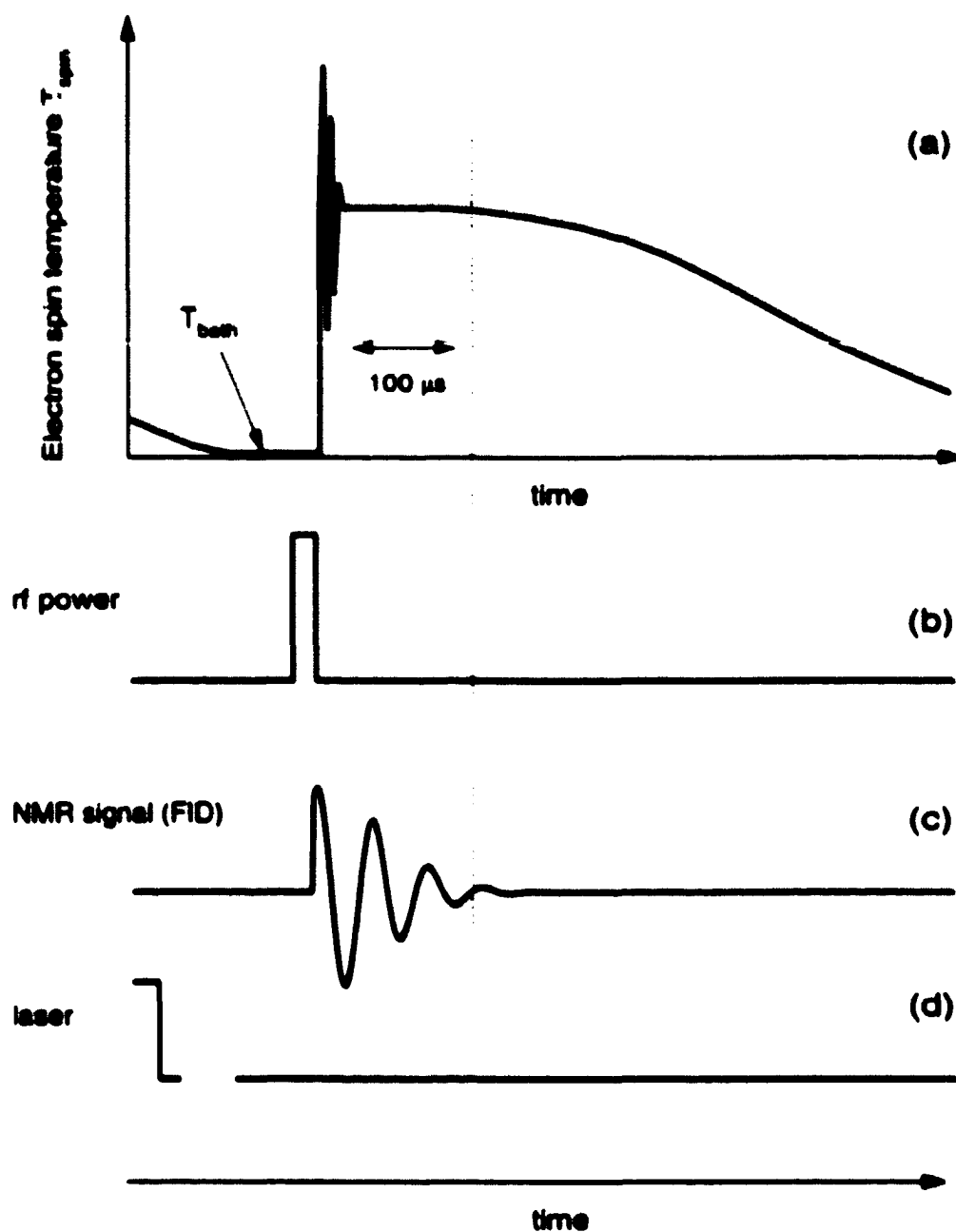


Figure 6.4: Possible behavior of the electron spin system during an OPNMR measurement: (a) initially spins are in equilibrium with the lattice and ^3He bath ($T_{spin} = T_{bath}$), then an rf pulse (b) excites spin system, but it quickly equilibrates at its own temperature $T_{spin} > T_{bath}$. The spin temperature must be fairly constant over the NMR time scale (c), otherwise a broadening of OPNMR line shape would occur, which is not observed (Fig. 6.3). Note that prior to the rf pulse ^3He bath (and thus the spin system) is cooling slowly over the dark time τ_D after a laser pulse (d).

Here n_n is the density of nuclei, and \mathcal{P}_n is the local nuclear polarization. The observed rf heating is clearly very different, depending on H_1 , for quite similar values of α (compare Fig. 6.1 (a) and (b)). It is this fact, that enabled us to avoid rf heating during our equilibrium measurements by turning down H_1 and proportionately increasing τ_{pulse} , which resulted in roughly constant tipping angles on the order of $\pi/2$, and thus reasonable NMR signal intensity.

Another possible mechanism, ohmic heating by eddy currents, appears inconsistent with the strong lattice temperature dependence of the effect⁶. Note that the dashed and solid lines corresponding to different lattice temperatures in Figure 6.2(c,d) actually cross each other, which thwarts any attempts to explain this behavior by heat absorption and/or thermal conductivity in certain parts of a bulk sample (e.g., if no heating is observed at $T > 0.5$, how can some part of the sample continue to heat up above 1 K, while being thermally anchored⁷ to the rest of the sample at $T \approx 0.3$ K?). It appears that rf energy is easily absorbed by the electron spins, but then takes a long time to escape this subsystem, as if the lattice decouples from the spins at low temperatures.

Our data therefore provides evidence for a direct coupling between the rf pulse and the spins in the 2DES. The mechanism for this interaction in a clean system is not known, because the applied rf photon energy⁸ is well below the electron spin

⁶It is also inconsistent with the strong H_1^2 dependence of the electron spin temperature, since any heating by eddy currents should result in $\eta = 2$.

⁷Using low-temperature specific heat [63] and thermal conductivity [64] data for bulk GaAs, we can estimate the thermal relaxation time of the sample to be about $1 \mu\text{s}$ (consistent with the speed of sound), too short to be observed in our OPNMR measurements.

⁸Our preliminary measurements also confirm this effect at $\nu = 1/2$, at the rf frequencies as low as 91.35 MHz. At that filling factor our "Knight shift thermometer" works much better, as no saturation is observed in the $K_S(T)$ data [65] down to 300 mK.

resonance at ~ 74 GHz. Impurities in the bulk or edge states may be playing a role in this process.

6.5 An Upper Limit for Electron Spin Relaxation Time

The evolution of equilibrium⁹ OPNMR spectra with the increasing dark time τ_D , such as shown in Figure 6.5, provides an upper bound on the electron spin relaxation time τ_{1s} . The measured spectra are essentially independent of τ_D beyond the first 0.5 s after the laser pulse is turned off, consistent with the time it takes for the laser-heated sample to equilibrate with the helium bath at 0.45 K (see section 4.5).

Combining this observation with the results of section 6.3, we arrive at the following estimate for the longitudinal electron spin relaxation time: $100 \mu\text{s} < \tau_{1s} < 500 \text{ ms}$, for the lattice temperature $T < 0.5$ K at $\nu = 1/3$. While this value of τ_{1s} is at least a factor of 1000 longer than recent measurements of the transverse relaxation time τ_2^* in bulk GaAs [66], it is consistent with a previous theoretical prediction [67] which assumed conditions rather similar to our experiment.

The experiments described in this Chapter can be further refined using a second independently gated rf power source. That way cooling of the electron spin system can be tracked directly by applying an off-resonant pulse at a higher power level, followed after a variable time τ_{delay} by another, weaker, tipping pulse at the NMR frequency f_0 . The resulting dependence of the electron spin temperature T_{spin} on τ_{delay} will provide, for instance, an exact value for the longitudinal electron spin relaxation time τ_{1s} . Also, any contributions of the ^{69}Ga and ^{75}As nuclear systems can be studied in detail by applying the first (heating) pulse at the corresponding resonant frequency.

⁹Here "equilibrium" means acquired using weak tipping pulses.

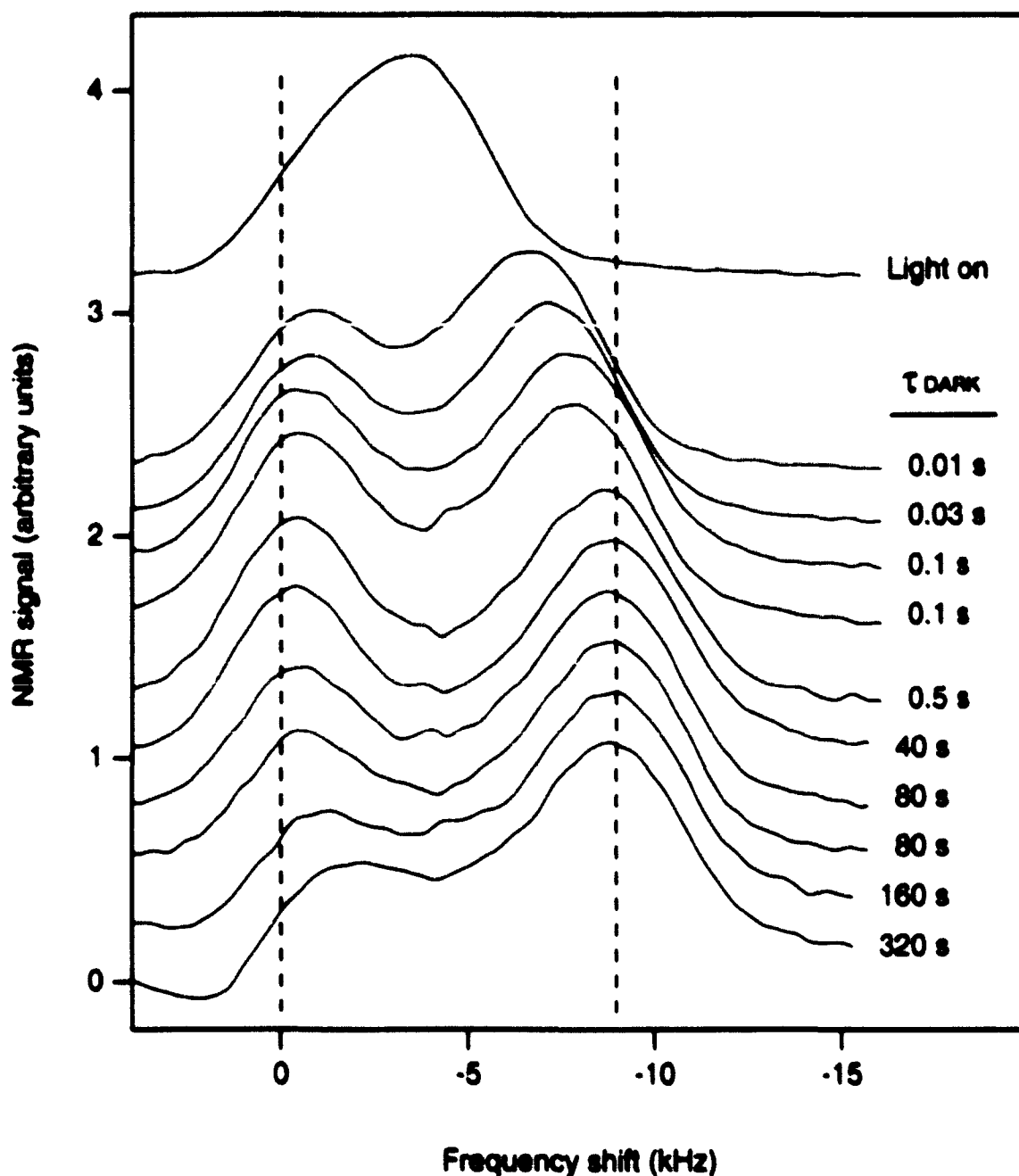


Figure 6.5: ^{71}Ga OPNMR spectra acquired with sample 40W at $T_{\text{bath}} = 0.45$ K. with the laser light ON during signal acquisition (the "Light on" spectrum) and with different dark times τ_D . The evolution of the line shape as a function of dark time shown here allows us to place an upper limit on the electron spin-lattice relaxation time τ_{1e} . The dashed lines mark the barrier (at 0 kHz) and the equilibrium well peak frequencies; the spectra are offset from one another vertically for clarity.

Chapter 7

NMR Measurements in GaN Epitaxial Films

7.1 Introduction and Theory

Advances in GaAs technology have led to the development of low-cost and long-lived red/infra-red diode lasers, with applications ranging from bar-code scanners to high-speed fiber optics communication networks. While the shorter wavelength of blue/ultra-violet semiconductor lasers would enable higher information density ($\sim \lambda^{-2}$) on storage media (e.g., compact disks) and in optoelectronics applications, the development of this technology has proved to be quite challenging. The unique characteristics of materials used in blue lasers are interesting to study from a basic physics research perspective, which may lead to the eventual technological breakthroughs that will enable these blue lasers to take over.

Early attempts to develop a short-wavelength diode laser focused on ZnSe-based materials (see Figure 7.1), and after much effort the lifetime of a continuously running laser was pushed beyond 100 hours, as reported by Taniguchi et al. [68] in 1996. However, residual defects and the device degradation associated with them

are a severe limitation, which have not yet been overcome in devices using the II-VI semiconductors.

Recently, attention has turned to $\text{In}_x\text{Ga}_{1-x}\text{N}$ -based devices, such as the blue and green LED's that were first produced by the Nichia Chemical Company in Japan. A critical breakthrough was accomplished in early 1997, when Nakamura et al. demonstrated the first continuously operated deep blue nitride diode laser [69]. In contrast to ZnSe-based laser materials, the nitrides are very robust even in the presence of high current densities, with excellent optical properties (e.g. high quantum efficiency) that may lead to high-power blue and ultra-violet lasers.

Despite significant recent progress in the development of GaN-based devices, many fundamental issues concerning their material properties have not yet been resolved. For instance, currently available GaN epitaxial layers are grown on poorly matched substrates, and as a result possess a complex crystal defect microstructure [70], where the extended state defect densities are of the order of typical *electron* densities in GaAs quantum wells. The details of this microstructure and the mechanisms that allow it to be compatible with the efficient light emission in GaN lasers are still far from being clearly understood, especially from the point of view of lowering the threshold current density.

Another issue of a fundamental importance for InGaN/GaN heterostructure design is the presence of large spontaneous and strain-induced macroscopic electric fields¹, such as shown in Figure 7.2, which could lead to interesting modifications of the electron band structure near the interfaces in multi-layer compounds [71].

Finally, the low miscibility of indium in GaN under typical growth conditions

¹As opposed to arsenides, the nitrides possess a wurtzite crystal structure with a lower symmetry, which allows them to exhibit a pyro-electric effect. In addition, large piezo-electric coefficients of the nitrides lead to significant strain-induced fields near defects and interfaces, that are of the same order of magnitude as the spontaneous pyro-electric fields.

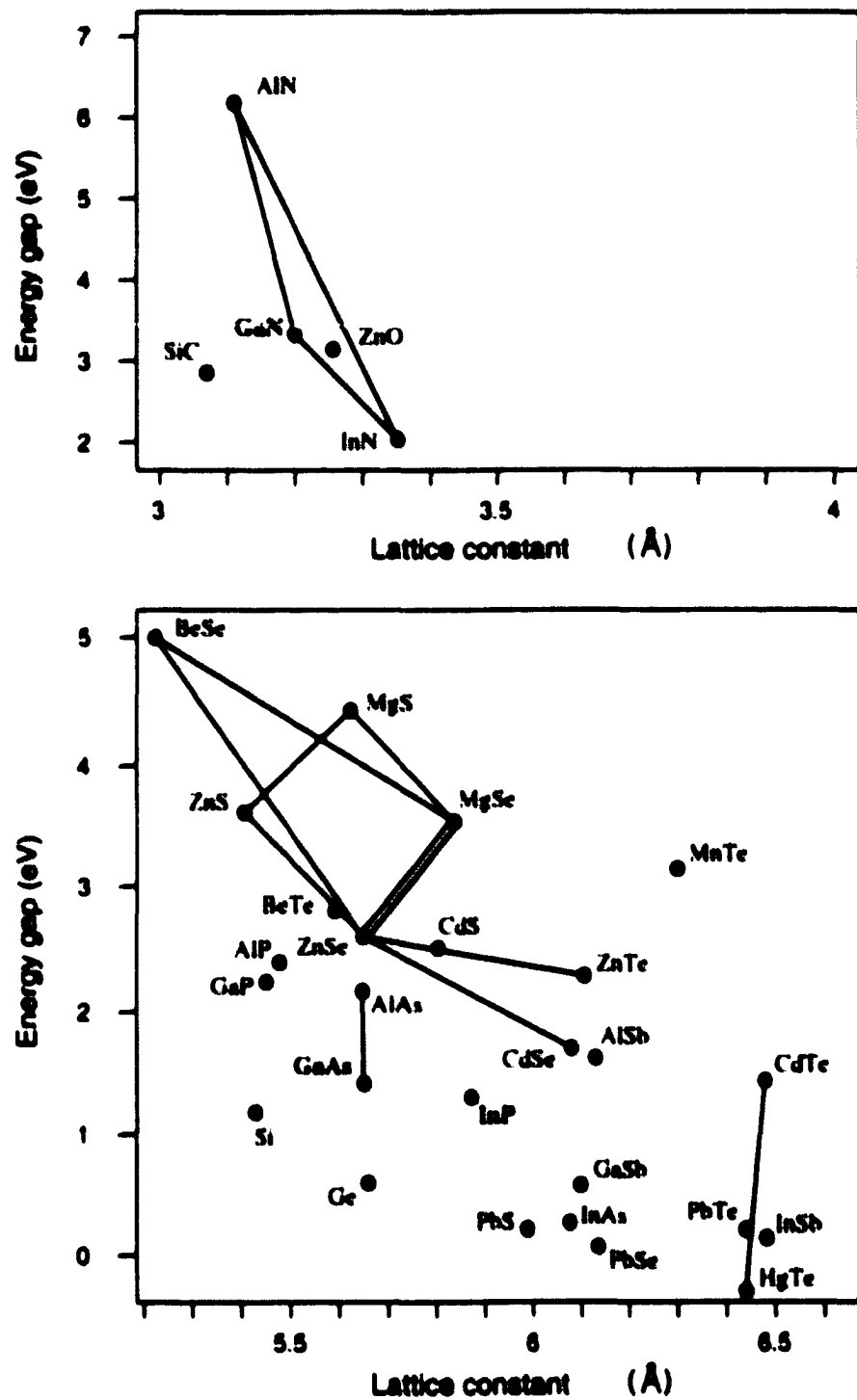


Figure 7.1: Bandgap - vs. - lattice constant diagram for wurtzite nitrides (top) and some ZnSe-based II-VI cubic semiconductors (bottom), along with possible substrate choices (after [72]). Solid lines show common alloy combinations.

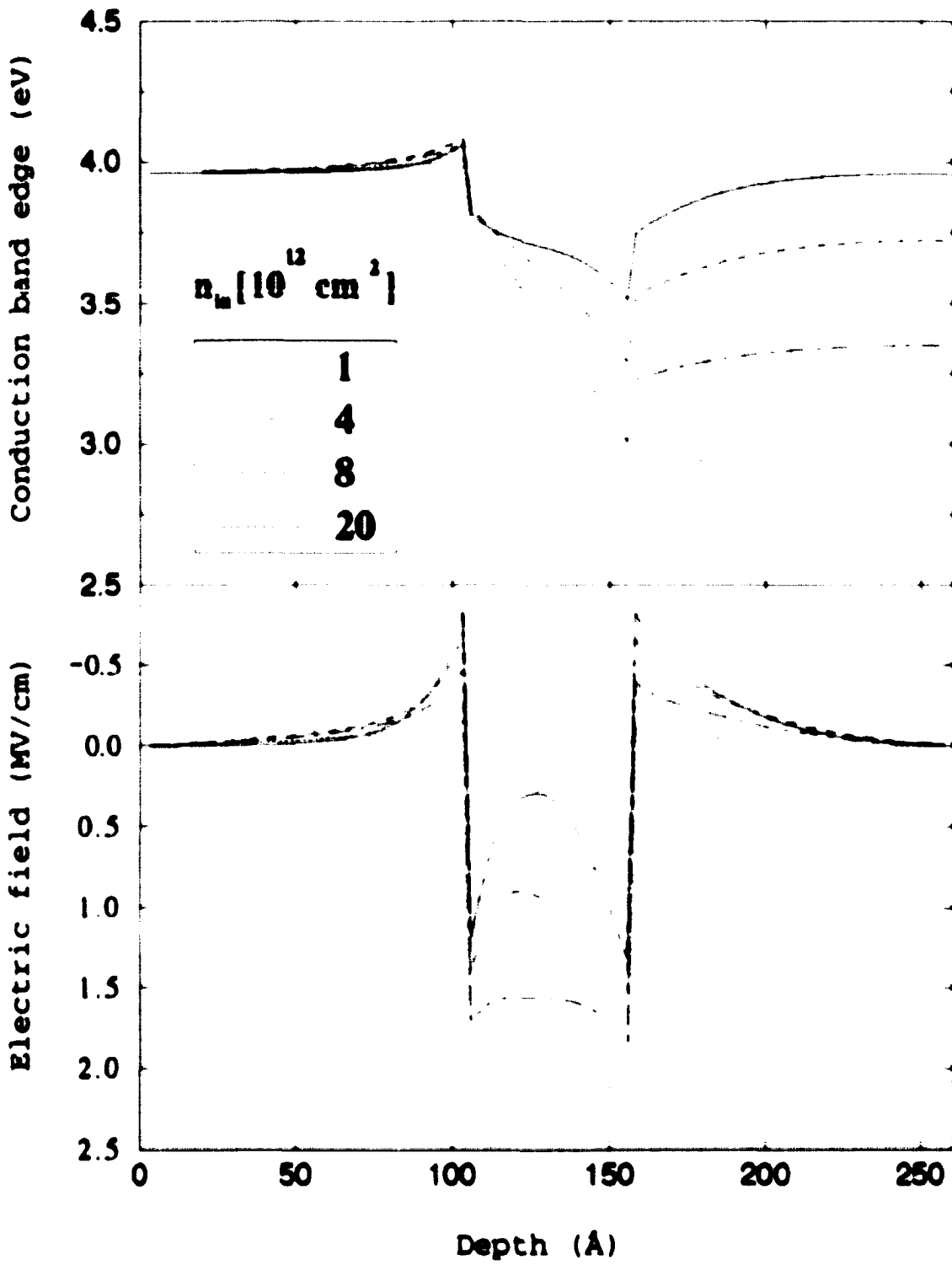


Figure 7.2: Self-consistent simulated band edge (a) and electric field (b) profiles for various sheet densities in a 50 Å thick QW. Adapted from Fiorentini et al. [71].

suggests that significant regions of pure InN can exist in a typical InGaN quantum well. In order to understand, control, and make use of these unusual properties, it is crucial to develop new probes of the local structure in these novel thin films [73].

NMR is a powerful local probe of the electronic and structural properties of materials. For nuclear species with spins $I > \frac{1}{2}$, such as ^{71}Ga , ^{69}Ga , ^{27}Al , ^{115}In , or ^{113}In (see Table 4.2), the electric quadrupole moment Q of the nucleus couples directly to electric field gradient $\nabla E^i = V_{i,j}$ at the nuclear site². The corresponding contribution to the Hamiltonian can be expressed (after diagonalizing $V_{i,j}$) as [6, 45]:

$$\mathcal{H}_Q = \frac{eQ}{4I(2I-1)} \left[V_{z,z}(3I_z^2 - I^2) + (V_{x,x} - V_{y,y})(I_x^2 - I_y^2) \right], \quad (7.1)$$

where the second term in the square brackets vanishes if $V_{i,j}$ is axially symmetric, which we further assume for simplicity. In the absence of \mathcal{H}_Q , all transitions between nuclear states corresponding to $\Delta m_I = \pm 1$ are at the same frequency $f^{(0)} = \frac{1}{2\pi} \gamma_n B_{\text{ext}}$, whereas a non-zero quadrupole coupling will perturb the nuclear Hamiltonian:

$$\mathcal{H}_n = -\gamma_n \hbar B_{\text{ext}} I_z + \frac{eQV_{z,z}}{4I(2I-1)} (3I_z^2 - I^2). \quad (7.2)$$

In typical laboratory fields $B_{\text{ext}} \sim 10\text{ T}$ the first (Zeeman) term dominates, so that we can use perturbation theory to calculate corrections to the energy levels E_m and the corresponding shifts in transition frequencies between $\Delta m_I = \pm 1$ states. Assuming that the sample symmetry axis \hat{z} (along which the component $V_{z,z}$ of the electric field gradient is taken) is tilted by angle θ with respect to the \hat{z} direction of magnetic field \vec{B}_{ext} , we obtain in the first order:

$$E_m = E_m^{(0)} + E_m^{(1)} = -\gamma_n \hbar B_{\text{ext}} m + \frac{eQV_{z,z}}{4I(2I-1)} \left(\frac{3\cos^2\theta - 1}{2} \right) [3m^2 - I(I+1)]. \quad (7.3)$$

In the case of half-integer nuclear spin, transition frequencies can be nicely labeled by the average m -value of the states involved:

$$f_{(m)} \equiv \frac{1}{\hbar} (E_{m-\frac{1}{2}} - E_{m+\frac{1}{2}}) = f^{(0)} + f_{(m)}^{(1)} + (\text{higher order terms}). \quad (7.4)$$

²Here we use tensor notation: $V_{i,j} \equiv \frac{\partial^2 V}{\partial x_i \partial x_j}$.

so that frequency $f_{(0)}$ of the central transition $m = -\frac{1}{2} \rightarrow \frac{1}{2}$ is not affected by the quadrupole coupling to the first order (i.e. $f_{(0)}^{(1)} = 0$), whereas the frequencies of transitions with $\langle m \rangle = \pm 1, \pm 2$, etc., are shifted symmetrically above and below it:

$$f_{(m)}^{(1)} = 3\langle m \rangle \frac{eQV_{zz'}}{4hI(2I-1)} (1 - 3\cos^2\theta) . \quad (7.5)$$

It turns out that axially symmetric wurtzite crystal structure of the nitrides does lead to huge microscopic electric field gradients at each nuclear site due to the local arrangement of electrons in the unit cell³. The resulting quadrupole splitting $f_{\pm 1m}^{(1)}$, proportional to the tilt parameter $r = 1 - 3\cos^2\theta$ and the magnitude $V_{zz'}$ of the local electric field gradient, can be as large as several MHz, compared to a typical dipolar linewidth of few kHz. This enormous spectral resolution makes quadrupole NMR spectroscopy an extremely sensitive probe of the local crystalline orientation (e.g. misalignments of the lattice in the vicinity of defects) as well as a perfect tool to study relatively weak electric field gradients due to piezo- and pyro-electricity in InGaN/GaN heterostructures.

In addition, chemical shift of NMR lines can play a role in identifying clusters of pure InN in InGaN quantum wells, provided optical pumping or some other method is used to boost NMR sensitivity at these sub-micron sample sizes.

7.2 GaN Samples

Samples were kindly provided to us by Dr. Noble Johnson and Dr. Dave Bour of Xerox PARC, along with x-ray and TEM data. The two GaN thin film samples were

³It should be noted here that usually electron charge density at the nucleus is neglected (since typical Knight shift in a semiconductor is much smaller compared to the quadrupole splitting), so that $\sum_{\alpha} V_{\alpha\alpha} = \nabla \cdot \mathbf{E} = 0$. From this it follows that if cubic symmetry is assumed ($V_{xx} = V_{yy} = V_{zz}$), the gradient and thus the quadrupole coupling vanishes: $\mathcal{H}_Q = 0$, which is the case for crystalline fields in the arsenides, which have the Zincblende crystal structure.

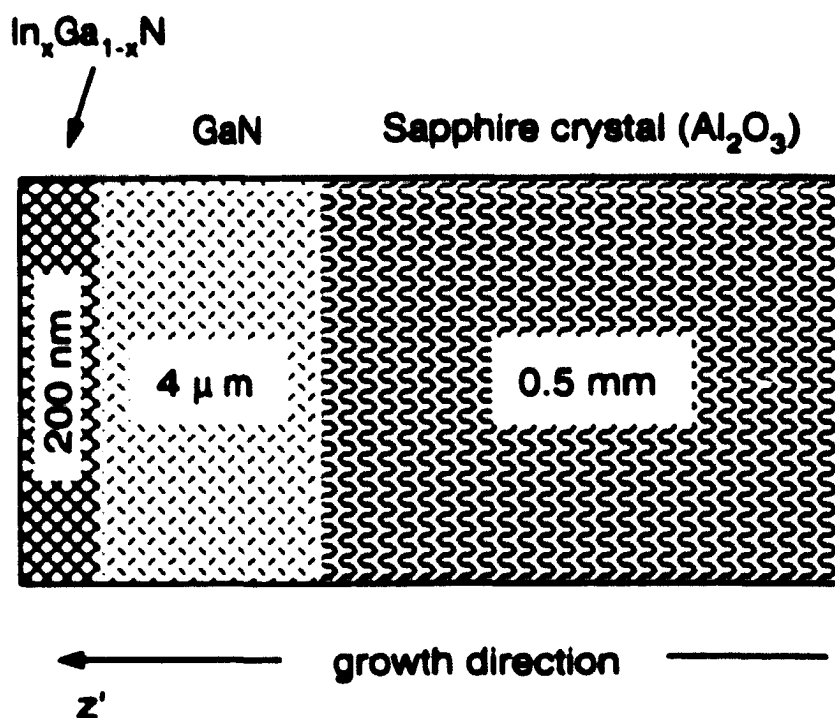
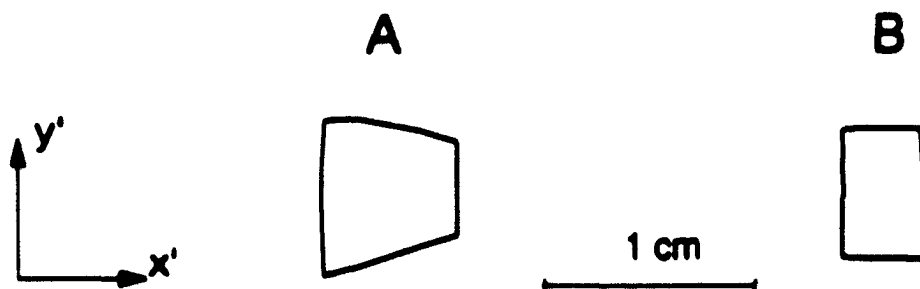
MOCVD:**Samples:**

Figure 7.3: Schematic diagram of the MOCVD layer structure, common to both GaN samples under study (top) and their planar dimensions (bottom). Note, that the indium fraction x is different for the two samples (see Table 7.1).

grown by MOCVD on a (0001)-sapphire substrate, and contain 4 μm of GaN as a buffer layer under a 200 nm InGaN quantum well, see Table 7.1. One sample is Mg doped, the other is nominally undoped. The schematic of this structure is shown in Figure 7.3 along with the planar dimensions for both samples.

Table 7.1: Dimensions and composition data for the GaN samples.

Parameter	(units)	Sample A	Sample B
Grower's ID number		B874	B870
Quantum Well width, w	(nm)	200	200
Quantum Well material		$\text{In}_x\text{Ga}_{1-x}\text{N}$	$\text{In}_x\text{Ga}_{1-x}\text{N}$
QW indium fraction, x		$x=0.07$	$x=0.21$
Buffer layer width	(μm)	4	4
Buffer layer material		GaN	GaN
Number of Quantum Wells		1	1
Substrate width	(mm)	0.5	0.5
Substrate material		Al_2O_3 (0001)	Al_2O_3 (0001)
Two-dimensional area	(cm^2)	0.393	0.242
Total number of nuclei:			
^{71}Ga		2.9×10^{18} (0.34 mg)	1.8×10^{18} (0.21 mg)
^{69}Ga		4.3×10^{18} (0.50 mg)	2.7×10^{18} (0.30 mg)
^{115}In		2.3×10^{16} (4.4 μg)	4.3×10^{16} (8.1 μg)

7.3 NMR Spectroscopy

As Table 7.1 shows, the amount of Ga available for NMR is minimal even in the relatively thick buffer layer, which makes detection of NMR signals a challenging task. Nevertheless, in our preliminary investigations reported in this Chapter, we did not use optical pumping, trying first to study these novel materials with conventional NMR.

After a week-long effort, thwarted initially by acoustic resonances of the NMR coil, we found the room temperature ^{71}Ga signal, shown in Figure 7.4(a). This spectrum was acquired with 2000 scans over ~ 7 minutes. It takes about 500 scans at room temperature before the peak starts to appear in the noise.

The situation is strikingly different at low temperatures, as Figure 7.4(b) demonstrates. At 1.5 Kelvin the nuclear relaxation time T_1 approaches several hours, and the practical strategy would be to take one or at most two scans, each after waiting for the nuclear polarization to build up for as long as the hold time of our ^4He bucket dewar (described in section 4.5) permits.

Both spectra shown in Fig. 7.4 contain only the central transition peaks, which are the easiest to observe since they are insensitive (to first order) to the broadening by local variations in the tilt and/or the electric field gradient, as can be seen from Equation 7.5 for $\langle m \rangle = 0$. We could compare the frequency of these peaks to our GaAs data at the same field, and estimate the difference in chemical shifts between GaN and GaAs. Our room-temperature value of $\sigma^{71\text{Ga}}(\text{GaN}) - \sigma^{71\text{Ga}}(\text{GaAs}) \approx 110$ ppm is in a good agreement with the published value of 117 ± 3 ppm measured in powder samples [74], which gave us confidence that we were actually observing NMR signals from GaN.

Despite our best attempts to scan the spectrum on both sides of the central peak, no satellite transitions (corresponding to $\langle m \rangle = \pm 1$) were observed even at angles

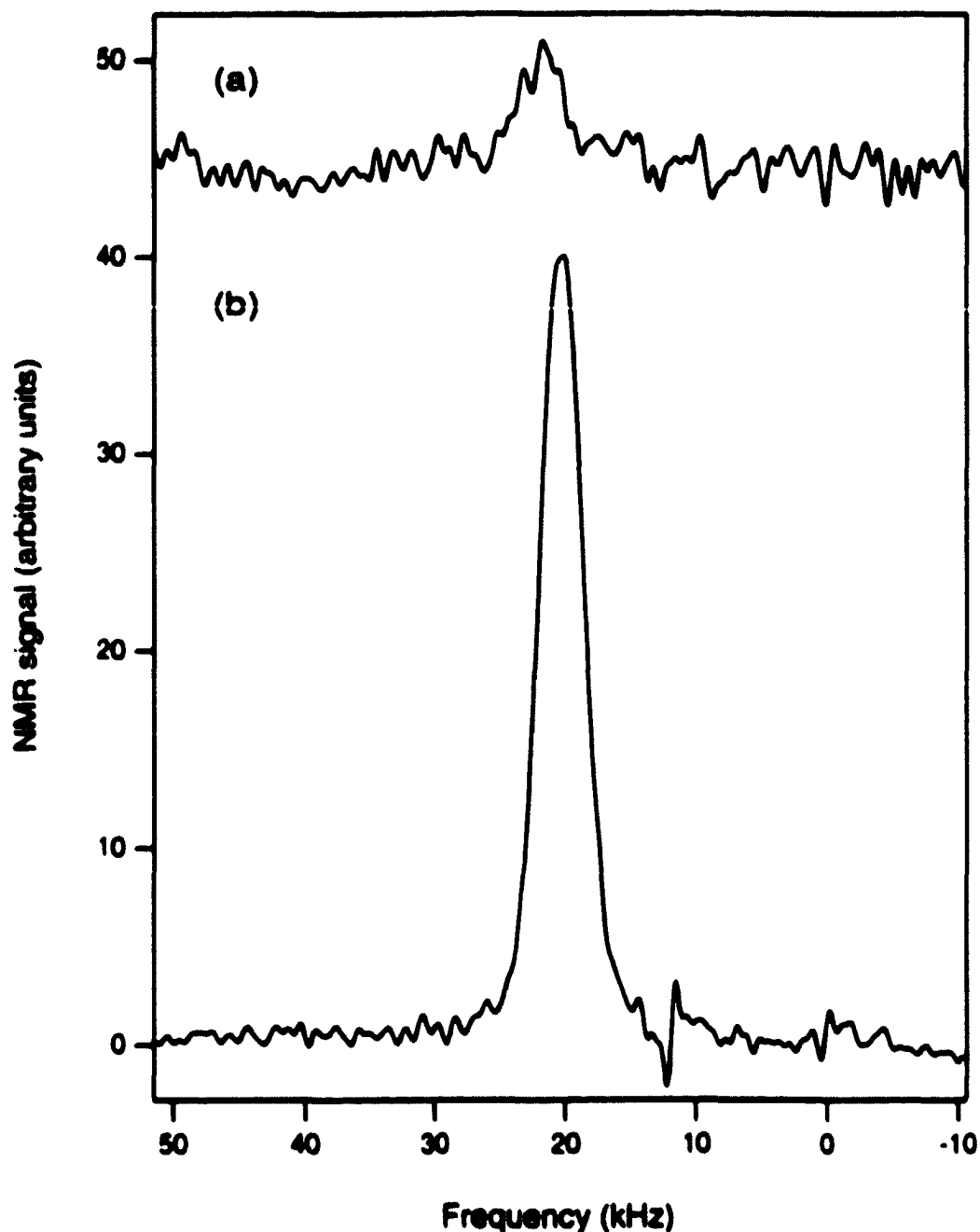


Figure 7.4: The first ^{71}Ga spectrum of sample "A" at room temperature (a), taken at $\theta = 53.2^\circ$ in $B_{\text{ext}} = 7.03\text{ T}$ ($f_0 = 91.34\text{ MHz}$). Only the central transition is observed after 2000 scans. A much better signal-to-noise can be achieved by cooling the sample down to 1.5 K (b), where a ^{69}Ga signal was recorded at $f_0 = 71.88\text{ MHz}$ in the same field. Still no satellites are observed at $\theta = 54.5^\circ$ after a single shot 5 hours long.

close to the “magic angle” of 54.7° , where the tilt parameter is $1 - 3 \cos^2 \theta \approx 0$ and the quadrupole splitting approaches zero, so that all transitions can fit within the same spectral window. The apparent absence of GaN satellites was extremely intriguing, since we could easily see all four ^{27}Al satellites in the single crystal sapphire substrate (see Appendix B).

Thus the satellite resonance is the key to answering a fundamental question about these as-grown epitaxial layers, namely: do they possess a long-range order of a single crystal, or are they closer to the limit of an amorphous material (due to the high density of defects arising from the lattice mismatch with the substrate)? To answer this big question, we needed to understand why it was so difficult to see the satellite transitions in the spectra. The next section describes how this issue was experimentally resolved in a rather non-trivial way.

7.4 Search for the Satellites

Figure 7.5 shows the dependence of ^{71}Ga and ^{69}Ga central transition frequencies on the sample tilt parameter $x = 1 - 3 \cos^2 \theta$ at $T = 4.2\text{ K}$.

For a complete lack of global crystalline orientation, such as in powder samples (which would result in an enormous broadening of the satellites, making them below the detection limit), one would expect no tilt dependence of the central transition frequency, since the corresponding NMR line would be already averaged over all possible local orientations. In the other extreme, if GaN in the sample were to form a single crystal without any defects or inhomogeneous electric field gradients (inconsistent with the absence of satellites) the central transition frequency would display a second order quadrupole shift, which has a parabolic dependence on the sample tilt parameter:

$$f_{(0)}^{(2)} = \frac{9}{256} \frac{2\pi e^2 Q^2 V_{zz}^2}{h^2 I^2 (2I - 1)^2 \gamma_n B_{\text{tot}}} \left[4I(I + 1) - 3 \right] \left[\left(x + \frac{2}{3} \right)^2 - \left(\frac{4}{3} \right)^2 \right]. \quad (7.6)$$

As Figure 7.5 demonstrates, our observations of the second order quadrupole shift in both ^{71}Ga and ^{69}Ga are much closer to the second limit. Although the minima of parabolic fits do not occur exactly at $x = -2/3$ as Equation 7.6 suggests, the quadratic coefficients obtained for ^{71}Ga and ^{69}Ga do scale as Q^2/γ_n for the two isotopes. From these coefficients we can extract the quadrupole splitting factor:

$$\nu_Q = \frac{3x QV_{zz}'}{2\hbar I(2I-1)} \quad (7.7)$$

which gives the first order splitting between NMR lines at $\theta = 0$ ($x = -2$), as can be seen from Eq. 7.5. Our values, extracted from the tilt dependence of the second-order quadrupole shift in the central transition frequency:

$$\nu_Q(^{71}\text{Ga}) = 885 \text{ kHz} \quad \text{and} \quad \nu_Q(^{69}\text{Ga}) = 1403 \text{ kHz} \quad (7.8)$$

are in very good agreement with the published quadrupole splittings of 0.85 and 1.4 MHz respectively, that were obtained from the linewidth measurements in polycrystalline (powder) samples [74].

The second-order tilt dependence of ^{71}Ga and ^{69}Ga central transition frequencies shown in Fig. 7.5 reflects a high degree of global order in the GaN epitaxial film. Knowing ν_Q allows us to find the satellite transition frequencies to first (Eq. 7.5) and second orders for any given tilt parameter x :

$$f_{(m)}^{(2)} = f_{(0)}^{(2)} + (m)^2 \frac{51}{64} \frac{2\pi r^2 Q^2 V_{zz}'^2}{\hbar^2 I^2 (2I-1)^2 \gamma_n B_{\text{tot}}} \left[\left(x + \frac{10}{17}\right)^2 - \left(\frac{24}{17}\right)^2 \right] \quad (7.9)$$

For the particular values of ν_Q quoted in Eq. 7.8 and $B_{\text{tot}} = 7.03 \text{ T}$, we can estimate that $|f_{(x1)}^{(2)}|_{\text{max}} \sim 10^{-2} |f_{(x1)}^{(1)}|_{\text{max}}$, and thus neglect the above second order correction to the satellite frequencies without loss of generality.

Now we can ask, what particular kinds of disorder can exist in the GaN film that would lead to a broadening of the satellite transitions $f_{(x1)}^{(1)} \propto QV_{zz}'(1 - 3\cos^2\theta)$ beyond the detection limit?

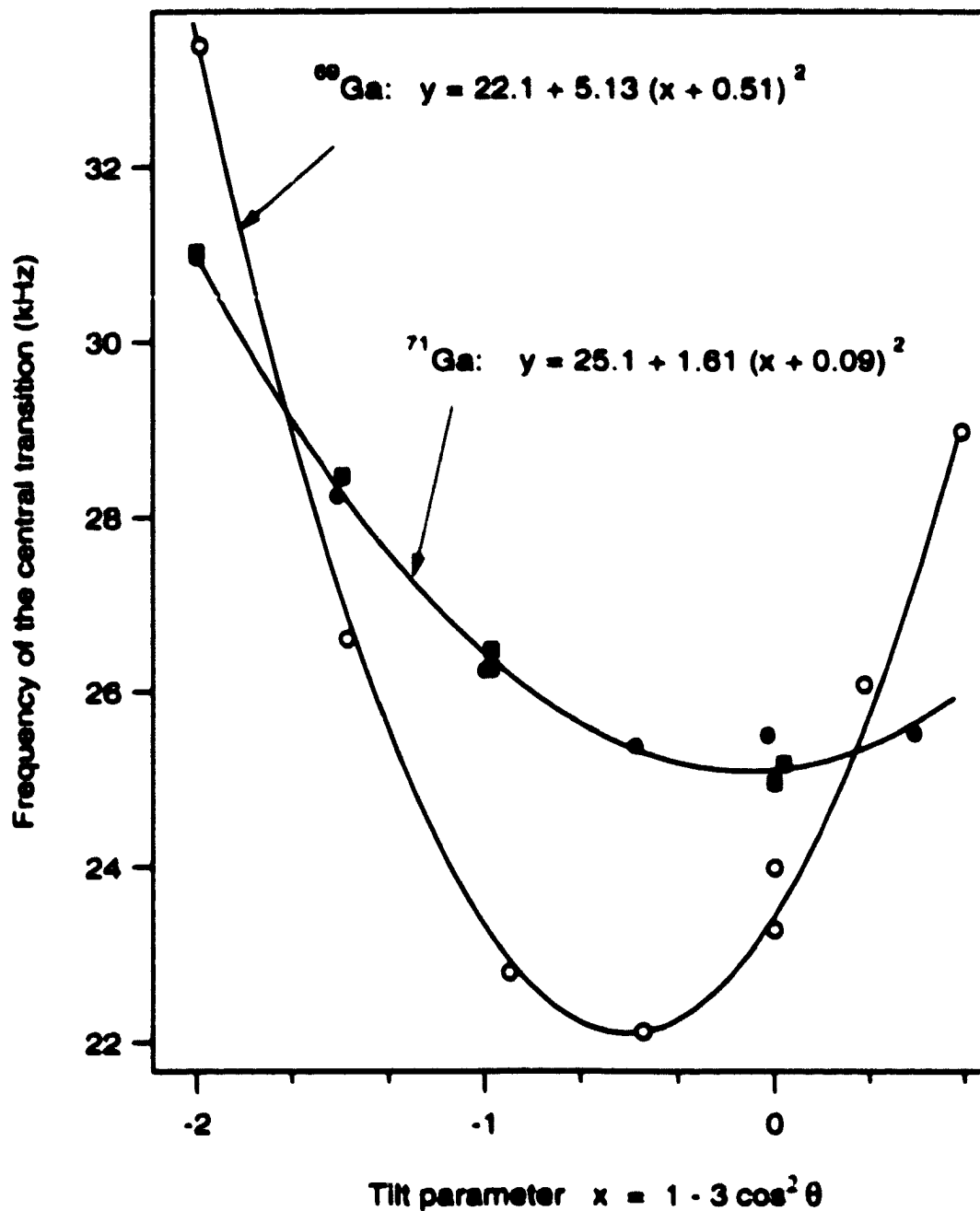


Figure 7.5: Second order electric quadrupole shift of the ^{71}Ga and ^{69}Ga central transition frequencies ($m = \frac{1}{2} \rightarrow -\frac{1}{2}$) as a function of sample tilt angle θ , plotted versus $x = 1 - 3 \cos^2 \theta$. Solid line fits are polynomials of the second order, to be compared to Equation 7.6. The quadratic coefficients 1.61 and 5.13 obtained from these fits do scale as Q^2/γ_n (see Table 4.2) to within 5%.

Suppose local fluctuations in the amplitude of $|V_{z'z'}|$ are primarily responsible for this. Then the broadening should be proportional to $f_{(\pm 1)}^{(1)}$ and thus vanish close to the magic angle. We mapped out thoroughly a range of θ on both sides of the magic angle, but found no trace of the satellites.

Another possibility can involve local variations in angle θ between the primary z' -axis of tensor $V_{\alpha\beta}$ and the laboratory field \vec{B}_{ext} . In that case, the broadening of satellite lines for a given angular spread $\Delta\theta$ should be:

$$\Delta f^{(1)} = \Delta\theta \frac{df^{(1)}}{d\theta} \propto \cos\theta \sin\theta. \quad (7.10)$$

Realizing this, we tuned our spectrometer to the frequency 1.4 MHz above the central transition in ^{69}Ga , and set the sample tilt angle to $\theta = 0$, such that the term $\cos\theta \sin\theta = 0$ and thus the broadening caused by the supposed angular spread of the local electric field gradients becomes minimal⁴. For best results we cooled the sample down to 1.5 K and waited for 5 hours before taking a single scan. The spectrum showed a weak, but clearly observable NMR peak⁵.

Our missing satellite transitions were thus finally discovered, with our subsequent observations confirming the existence of the lower satellite peak at $\theta = 0$, and also both upper and lower satellites in ^{71}Ga , all at frequencies consistent to the second order with our estimated quadrupole splitting constants given in Equation 7.8.

⁴Once $\int f^{(1)} = 0$, the satellites can still be broadened to some extent by the terms which are proportional to $\Delta\theta^2 \int f^{(1)}$.

⁵Other (broader) peaks due to acoustic ringing of the NMR coil initially obscured the spectrum. We could discriminate against those by taking multiple "dummy" scans at very high repetition rate (~ 30 ms) shortly after the "signal" scan. NMR signal with its long T_1 longitudinal relaxation time saturates [41, 6] and is hardly present in the "dummy spectrum", but the short-lived ringing is exactly the same in each scan regardless of the repetition rate. This allows to subtract the dummy spectrum, divided by the number of dummy scans, from the initial spectrum, with the remarkable results shown in Figure 7.6.

7.5 Characterization of the Disorder

Figure 7.6 shows a gradual disappearance of the ^{69}Ga upper satellite (i.e. $(m) = 1$) signal as the sample is tilted away from $\theta = 0$. Note that this transition is shifting towards lower frequencies (in agreement with Eq. 7.5) and at the same time is broadened as the tilt angle θ between the sample's growth axis and the magnetic field is increased. This progressive broadening leads to a drop in the peak intensity (as the integrated intensity is conserved), which eventually brings the satellite signal below the noise level at tilt angles $\theta > 12^\circ$.

To describe this behavior quantitatively, we assumed a uniform distribution of the local tilt angles θ and a Gaussian distribution of the local magnitudes $|V_{T,z}|$ around their average "global" values of $\bar{\theta}$ and $|\bar{V}_{T,z}|$. We then simulated the satellite line shape for variable amounts of scatter and tried to fit it to the measured spectra shown in Fig. 7.6.

We found that the satellite linewidth of ~ 15 kHz (FWHM) observed at $\theta = 0$ can not be explained by the angular scatter only, and we need at least a 1% FWHM Gaussian scatter in the magnitude of $V_{T,z}$ throughout the epitaxial layer to fit the top spectrum in Fig. 7.6.

On the other hand, if this were the only kind of disorder present in the epitaxial film, we would not be able to explain the observed *increase* in the linewidth as the sample is tilted away from $\theta = 0$, since the broadening due to variations in $|V_{T,z}|$ is proportional to $r = 1 - 3\cos^2\theta$ and is *the largest* at $\theta = 0$. Thus, a spread of $\sim \pm 2^\circ$ in the local $V_{\alpha\beta}$ principal axis directions around the sample z' axis (Fig. 7.3) is needed to explain other spectra in Fig. 7.6.

This kind of angular spread can in principle be attributed to low-angle tilts of individual crystalline grains, except for the fact that it is about twenty times larger in magnitude than the angular inhomogeneity inferred from the x-ray and TEM mea-

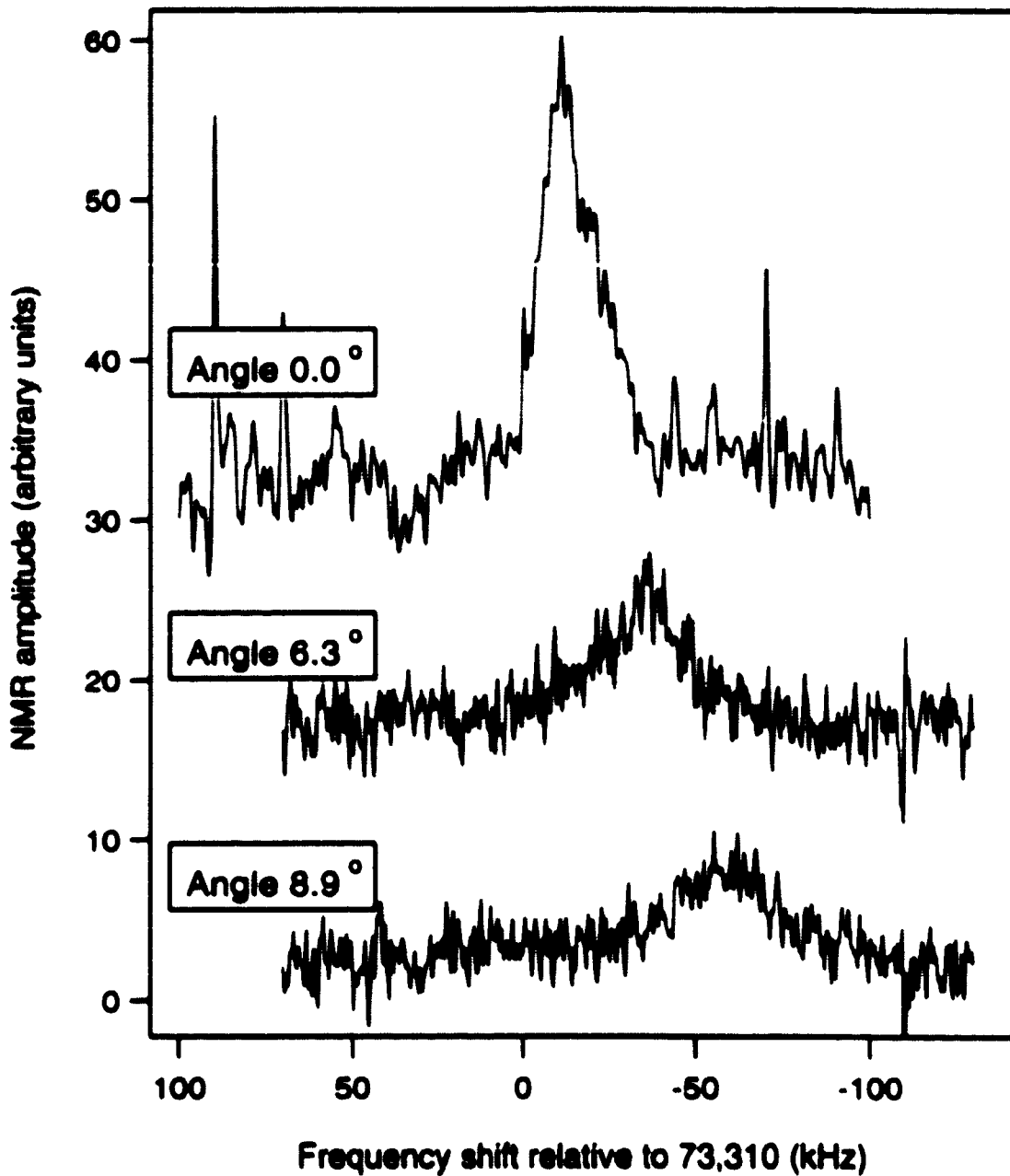


Figure 7.6: The upper ^{69}Ga satellite transition ($m = -\frac{1}{2} \rightarrow -\frac{3}{2}$) for several different tilt angles θ . Note how the satellite line shape broadens (leading to a drop in the peak amplitude) as the tilt angle between the sample growth direction and the magnetic field is increased away from $\theta = 0^\circ$ ($x = -2$). Each spectrum took 5 hours at $T = 1.5\text{ K}$.

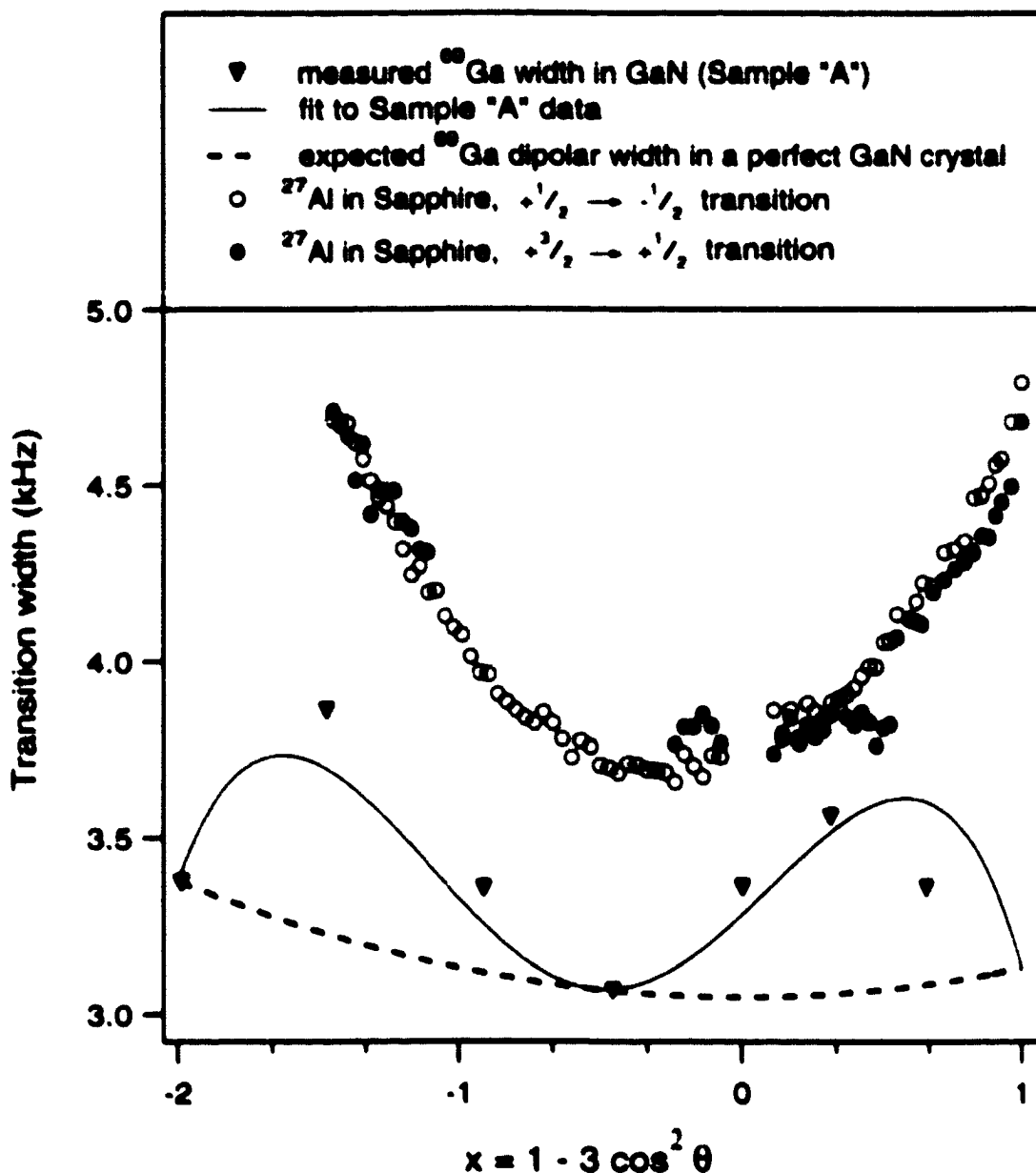


Figure 7.7: The dependence of the ^{69}Ga central transition linewidth (open triangles) on the sample tilt angle θ is distinctly different from both the expectation for a "perfect" GaN crystal (dashed line) and the ^{27}Al linewidth measurements on a single-crystal sapphire (open and filled circles). Rather, the observed GaN linewidth exhibits an extra broadening away from $x = -2$, $-2/3$, and 1 , following a solid line fit which is consistent with an angular scatter of $\pm 2^\circ$ in the local electric field gradients).

measurements on these samples [75]. Thus, it appears likely that our observed spread is reflecting something else... such as internal piezo- and /or pyro-electric fields (possibly caused by defects and interfaces), superimposed on the crystalline fields at each nuclear site.

Figure 7.7 shows an independent measurement which leads to the same conclusion. The linewidth of the ^{69}Ga central transition is varying markedly as a function of $x = 1 - 3\cos^2\theta$. This is in contrast to the smooth behavior of the ^{27}Al central transition measured⁶ in single crystalline sapphire (Figure 7.7, open circles), and the observed tilt dependence of dipolar linewidth in GaAs (Equations 5.1 and 5.2). To explain this behavior in our GaN samples, we note that the central transition resonance frequency for ^{69}Ga , expressed to the second order in perturbation theory in Equation 7.6, is observed in practice (see Fig. 7.5) to be:

$$f_{(0)} = \text{const.} + 5.13 [\text{kHz}] \times \left[(1 - 3\cos^2\theta) + 0.51 \right]^2 \quad (7.11)$$

This expression can be differentiated with respect to θ to obtain the extra broadening $\delta f_{(0)}$ of the central transition, produced by the a spread $\delta\theta$ in the tilt angles: $\delta f_{(0)} = \delta\theta \frac{d}{d\theta} f_{(0)}$. Remarkably, the observed central transition linewidth (Figure 7.7, open triangles) displays no extra broadening only at three values of x , namely $x = -2$, 1, and $x \sim -0.5$ (where the minimum of the parabolic fit shown in Figure 7.5 occurs). These are the only values of x at which the derivative $\frac{d}{d\theta} f_{(0)}$ is equal to zero. The magnitude of the observed extra broadening of the ^{69}Ga central transition again implies a spread of $\sim \pm 2^\circ$ in the “local” principal axis directions of the electric field gradient tensor.

⁶See Appendix B for details.

7.6 Future Goals

All of the results described thus far in this Chapter are based on NMR signals that were primarily due to the 4 μm thick GaN buffer layer, and can hardly be used to characterize the disorder and the internal electric field gradients in a 200 nm thick InGaN quantum well.

Figure 7.8 illustrates our attempts to detect the quantum well signal directly by switching to the indium frequency, since indium is not present anywhere else in the sample. To optimize the NMR acquisition parameters, we used a small piece of InP wafer⁷, which produced easily detectable signals for both In isotopes (see Fig. 7.8), once placed into the sample coil. We then took InP out, lowered the temperature down to $T = 1.5$ K, and accumulated 42 scans⁸ from sample A over the 5 hour hold time of our ⁴He cryostat. The resulting spectrum showed no indium signal, even after subtraction of the background signal due to acoustic resonances in the NMR coil.

This negative result indicates that a natural step to take next would be to use optical pumping, which our laboratory has specialized in from its conception in 1995. This will allow us to boost and thus detect NMR signals from a single InGaN quantum well, which so far is below the conventional NMR detection threshold. Since GaN is a wide-bandgap semiconductor, it has to be optically pumped with a blue light, and thus many of the optical components in our system need to be optimized for the new

⁷The wafer was kindly provided to us by Prof. Lou Guido from the Yale Electrical Engineering Department.

⁸We used a relatively fast (for the temperature $T = 1.5$ K) repetition time of ~ 7 min because the expected T_1 relaxation time of indium is much shorter than that for both gallium isotopes. At these low temperatures longitudinal nuclear spin relaxation is dominated (in the absence of free electrons) by a quadrupole coupling to the time-dependent electric field gradients, associated with phonons. The enormous quadrupole moment of indium (see Table 4.2) will thus most likely lead to relatively short indium T_1 relaxation times in InGaN.

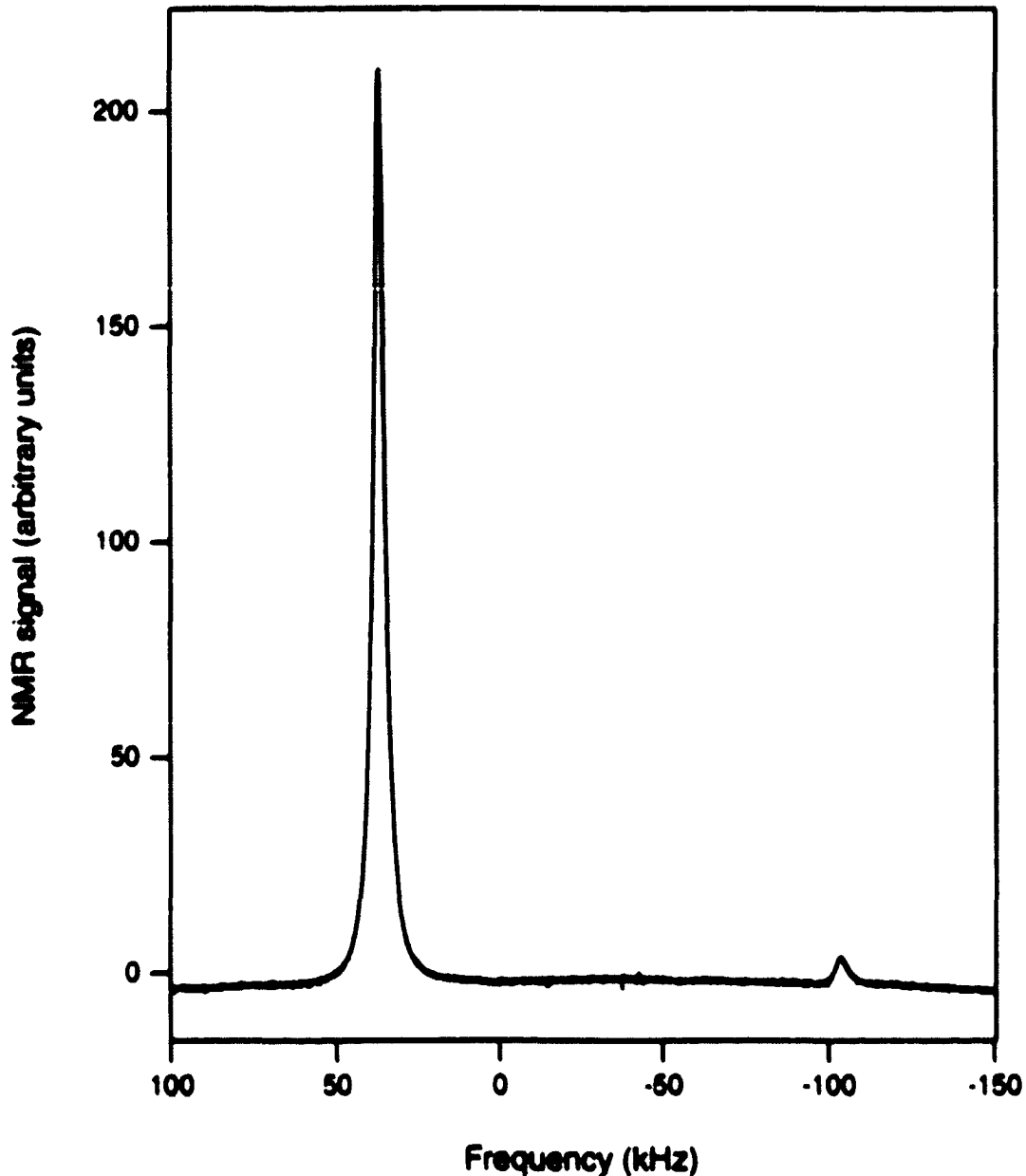


Figure 7.8: In our attempts to detect indium NMR signal from the 200 nm thick $\text{In}_{0.07}\text{Ga}_{0.93}\text{N}$ epitaxial layer in sample "A", we inserted a small fragment of InP substrate into our NMR coil, which resulted in the indium spectrum shown. Here $B = 7.0348\text{ T}$ and $f_0 = 65.677\text{ MHz}$. Note, that signals both from ^{115}In (large peak) and ^{113}In (small peak) isotopes can be easily seen (see Table 4.2). However, the indium signal from the epitaxial $\text{In}_x\text{Ga}_{1-x}\text{N}$ layer proved to be below the sensitivity limit of our conventional NMR measurement.

wavelength.

As a proof of principle, we used OPNMR to detect the signal from a single 250 Å wide GaAs quantum well. Figure 7.9 shows an OPNMR spectrum obtained after pumping for 60 s using ~50 mW of red (813 nm) light. The “W” peak here is detected with a good signal-to-noise ratio from mere 8.6×10^{15} , or about 1 μg , of ^{71}Ga nuclei, a number that is even somewhat smaller than the number of indium nuclei in sample A (see Table 7.1). The direct comparison, however, is complicated by large differences in the relaxation time T_1 and by the number of expected satellites, on which the signal amplitude strongly depends.

To summarize, even though we have been working at the very limit of conventional NMR detection, quantitative information about disorder in the GaN epitaxial layers may be already inferred from our preliminary measurements⁹. Major equipment and experimental changes, necessary to apply an OPNMR approach to the study of GaN-based thin films are already in the development stage, with our ultimate goal being the ability to probe local microscopic properties of the associated nitride quantum wells. Based upon our experience in GaAs, we expect to obtain an approximately hundred-fold signal enhancement when optical pumping is used, which will open up the exploration of crystal structure and internal electric field gradients in the novel GaN-based heterostructures down to 3 – 5 Å length scales.

⁹Recently the first successful attempts to grow bulk GaN single crystals have been reported [76] with a view towards developing perfectly matched substrates for InGaN/GaN-based devices. Characterization of these crystals can be another potential application of the NMR techniques described in this Chapter.

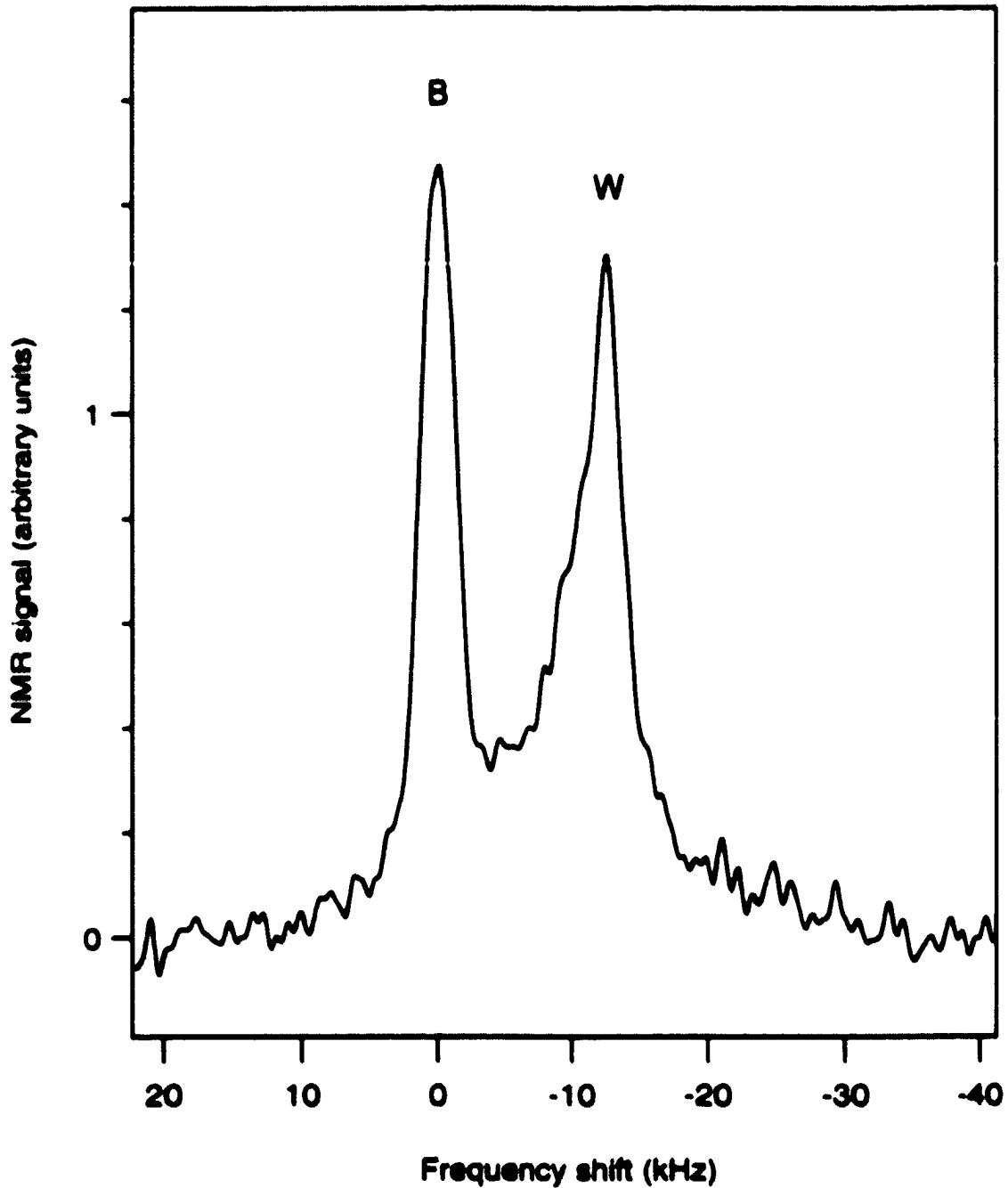


Figure 7.9: ^{71}Ga OPNMR emission spectrum of a single 250 Å-wide GaAs quantum well (containing 8.6×10^{15} , or about $1 \mu\text{g}$, of ^{71}Ga nuclei), acquired at $\theta = 19^\circ$ and $T = 1.5 \text{ K}$, in $B_{\text{ext}} = 7.985 \text{ T}$ at a frequency $f_0 = 103.7 \text{ MHz}$. “B” and “W” refer to the barrier and the quantum well signals, respectively.

Chapter 8

Conclusions

Our measurements of electron spin polarization and dynamics near the primary Fractional Quantum Hall effect ground state of $\nu = 1/3$ provide evidence for novel spin phenomena and place important constraints on the theoretical description of this “fragile” quantum Hall ferromagnet.

Whereas the earliest theory of the fractional QHE assumed that the electrons are fully spin-polarized for $0 < \nu < 1$, our Knight shift measurements indicate that in the immediate vicinity of $\nu = 1/3$, there is a small (but measurable) depolarization. Although it appears similar to the Skyrmion peak at $\nu = 1$, the effect at $\nu = 1/3$ is much weaker: only ~ 0.1 of electron spin is reversed per unit of flux added to the system. Surprisingly, this trend continues unchanged through a large range of the filling factors, including $\nu = 2/7$, in contrast to the distinct structure seen in the transport measurements.

This spin reversal, associated with charged excitations of the $\nu = 1/3$ ground state, is even more evident in our linewidth measurements, showing a non-monotonic temperature dependence of the well lineshape broadening, which grows continuously as the filling factor is varied away from $\nu = 1/3$. We attribute this non-trivial behavior to localization of the spin reversed regions over the NMR time scale of $\sim 40 \mu\text{s}$.

In addition, we observed an unusual coupling of the radio-frequency magnetic fields to the spins of 2DES. This effect exhibits an extremely strong non-linear dependence on the sample lattice temperature and the amplitude of the field. Surprisingly, the electron spins relax very slowly once excited by the rf field, which allows us to place an estimate on the longitudinal electron spin-lattice relaxation time: $0.1 \text{ ms} < \tau_{1s} < 500 \text{ ms}$.

In an attempt to use OPNMR in the studies of new wide-bandgap semiconductor materials, we performed preliminary measurements on GaN epitaxial layers with conventional NMR, which despite the very small sample sizes led to a number of interesting results. The measured second-order quadrupole broadening of the central transition is consistent with our observations of enormously broadened satellite transitions in the limited range of tilt angles, from which we infer that the local electric field gradients have an angular scatter of $\pm 2^\circ$, exceeding the spread in the local crystalline lattice orientations by a factor of ~ 20 .

Appendix A

Calibration of RuO₂ thermometer in high magnetic fields

Table A.1 shows the field-dependent calibration data for our 2000 Ω RuO₂ thermometer (Fig. 4.9(a), position 2), that was obtained by sweeping the magnetic field at a fixed temperature using a field-independent capacitance reference sensor.

Table A.1: Measured field dependence of the RuO₂ calibration data.

Magnetic field (T)	Temperature (K)					
	0.42	0.58	0.65	0.89	1.51	5.15
	Sensor impedance (Ω)					
0	5850	4938	4679	4057	3321	2453
1	5757	4859	4592	4051	3325	2457
2	5726	4820	4605	4055	3337	2462
3	5731	4821	4654	4066	3353	2467
4	5752	4858	4704	4081	3373	2472
5	5777	4919	4736	4098	3393	2476
6	5796	4993	4746	4116	3412	2481
7	5807	5063	4742	4134	3429	2486
8	5811	5117	4739	4149	3443	2490
9	5814	5150	4749	4162	3455	2495
10	5830	5173	4777	4173	3465	2499
11	5877	5218	4816	4181	3473	2503
12	5984	5349	4839	4189	3483	2508

A detailed zero-field calibration of our RuO₂ sensor, obtained for the range of temperatures $0.285 < T < 200$ K by using three independent factory-calibrated thermometers, could be approximated by:

$$T_0(R) = \exp \left[a_1 - \left(\frac{a_2}{r} \right)^{a_3} + \left(\frac{a_4}{r} \right)^{a_5} - a_6 \ln(r) + \sum_{j=1}^6 (c_{2j-1} \cos jt + c_{2j} \sin jt) \right], \quad (\text{A.1})$$

where $r = R - 1893 \Omega$; $t = a_7 \ln(a_8 + \ln r)$, and a_j, c_j are given in Table A.2.

Using the data in Table A.1, we made the following interpolation of the field-dependent calibration:

$$T(R, B) = T_0(R) + b \left(d_1 + d_2 \left(1 + \exp \left[\frac{1}{d_3} \left(-T_0(R) + \sum_{j=0}^n g_j B^j \right) \right] \right)^{d_4} \right) T_{\Delta}(R), \quad (\text{A.2})$$

where $b = \frac{B}{12 \text{ T}}$, d_j, g_j are given in Table A.2, and

$$T_{\Delta}(R) = \frac{\exp \left[-(3q + h_1)^4 / h_2 \right]}{1 + \exp[h_3 q + h_4]} \sum_{j=0}^{14} k_j q^j, \quad (\text{A.3})$$

with $q = \frac{1}{4} [h_5 + \ln(R - 1999 \Omega)]$, and h_j, k_j given in Table A.2.

Table A.2: Interpolation coefficients for the field-dependent RuO₂ calibration.

j	a_j	c_j	d_j	g_j	h_j	k_j
0				-0.14662		1.11316
1	9.478759	0.009067	-4.5	40.73259	1.9514	0.13411
2	107.12972	-0.003381	5.5	-522.52437	118.89	-1.82538
3	14.352	-0.034878	0.18	3015.30139	-13.46922	-4.41193
4	157.25296	0.005544		-9510.26425	-5.25075	29.04096
5	2.3709	0.010230		17385.15091	-5.5	30.74219
6	1.2499	0.028322		-18357.09345		-151.91103
7	1.13633	0.008261		10388.66573		-71.48978
8	-4.7	0.004888		-2440.56451		335.14834
9		0.000331				74.45248
10		-0.006830				-366.72384
11		-0.000921				-34.80849
12		-0.003085				199.21497
13						5.79426
14						-42.82845

Appendix B

Quadrupole Aluminum NMR as a Precision Tilt Sensor

Figures on the following pages demonstrate possible use of ^{27}Al NMR as a tool to calibrate the sample rotator *in situ* with respect to the magnetic field. All of the data shown in this Appendix were obtained in $B_{\text{ext}} = 7.985\text{ T}$ at room temperature, although similar results were also obtained at a temperature of $T = 4.2\text{ K}$.

From our measurements we extract the following values of the quadrupole splitting constant (Eq. 7.7) for sapphire:

$$\nu_Q(\sim 285\text{ K}) = 360.17\text{ kHz} \quad \text{and} \quad \nu_Q(4.2\text{ K}) = 357.13\text{ kHz} . \quad (\text{B.1})$$

consistent with $\nu_Q(T)$ data obtained from the single crystal measurements [77].

Our measurements are also fully consistent with the second order perturbation theory of the quadrupole shift (Equations 7.6 and 7.9), and confirm the accuracy of the Swedish rotator stage to be¹ well within $\pm 0.1^\circ$ over the entire accessible range of angles for $\theta > -25^\circ$.

¹Assuming our knowledge of the constant rotator offset which can be determined exactly from the measurements in Figure B.3.

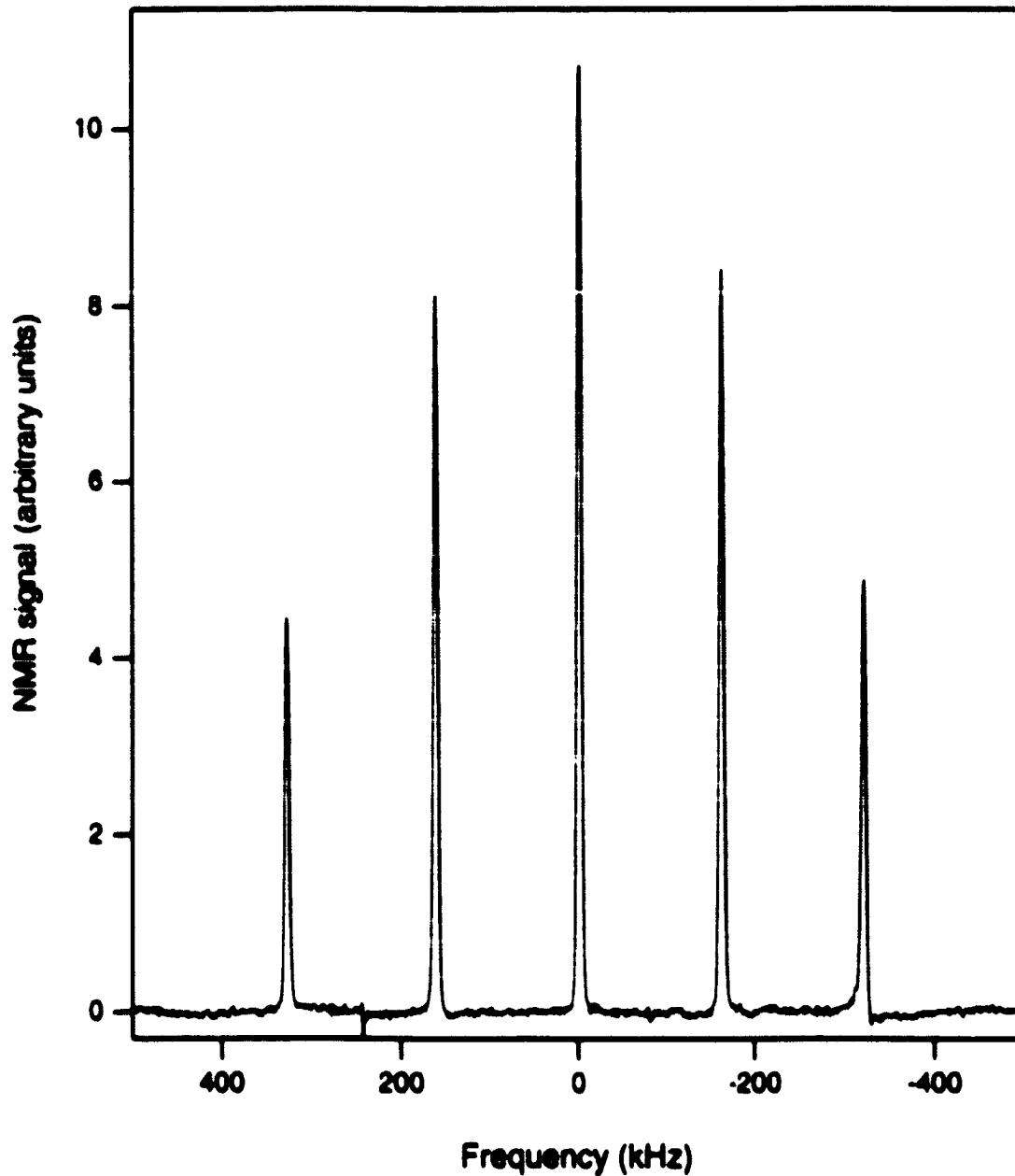


Figure B.1: Typical room temperature ^{27}Al NMR spectrum of single crystal sapphire, taken at $\theta = 37^\circ$ in $B_{\text{ext}} = 7.985 \text{ T}$ ($f_0 = 88.58 \text{ MHz}$). All five transitions, split by a quadrupole coupling to the crystalline electric field gradients, are observed. Similar spectra are easily obtained at temperatures down to $T \sim 4.2 \text{ K}$ by waiting for nuclear polarization to build up and then using a small tipping angle of $\alpha \approx 5^\circ$, which allows a rapid acquisition of spectra one after another.

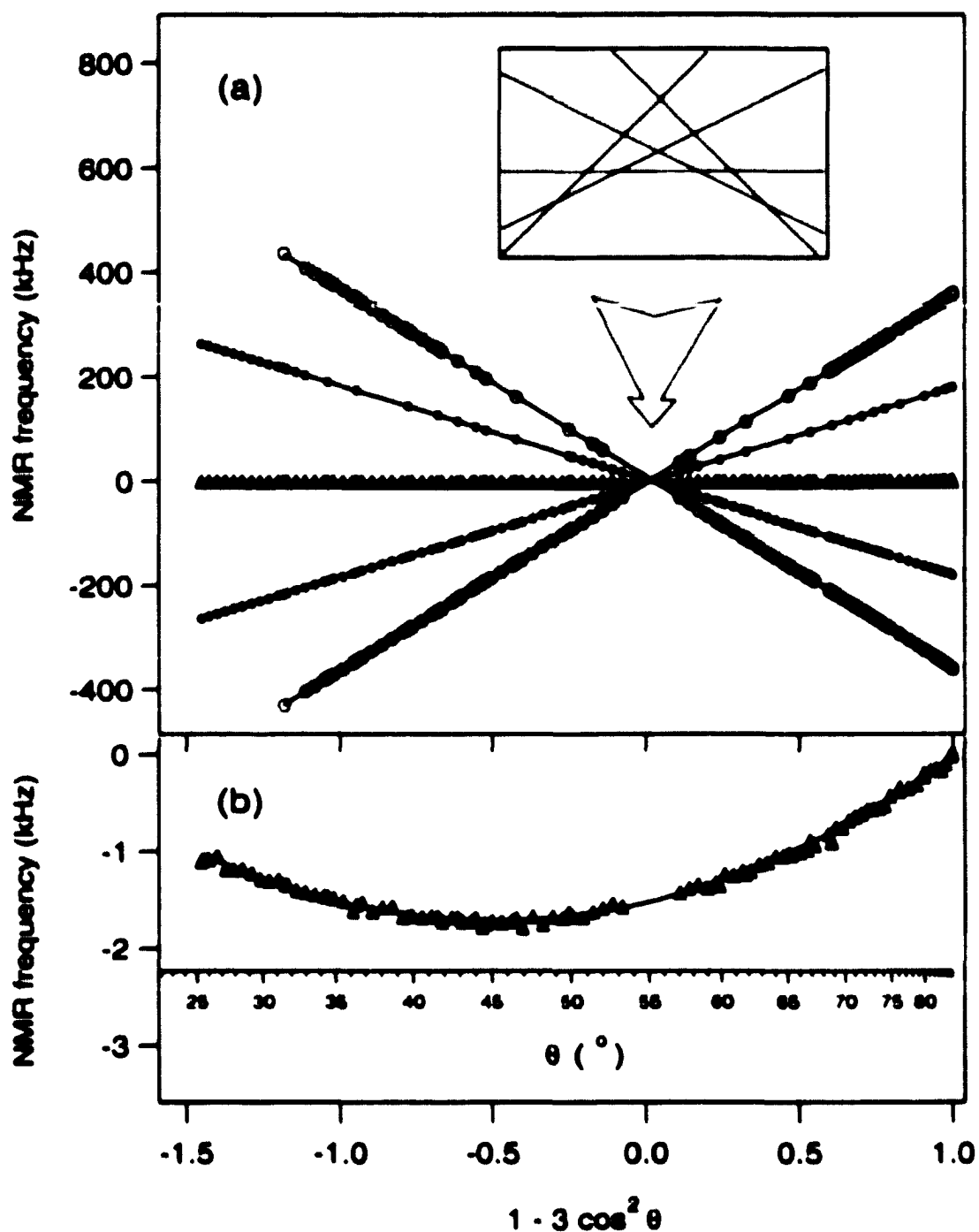


Figure B.2: Quadrupole shift of the ^{27}Al satellite transition frequencies as a function of tilt (a), with the second order shift of the central transition shown in (b) on a finer scale. The inset shows crossing of the parabolae fitted to the data for each transition. Proportions of the delta-like pattern are consistent with the second order perturbation theory (Equations 7.6 and 7.9).

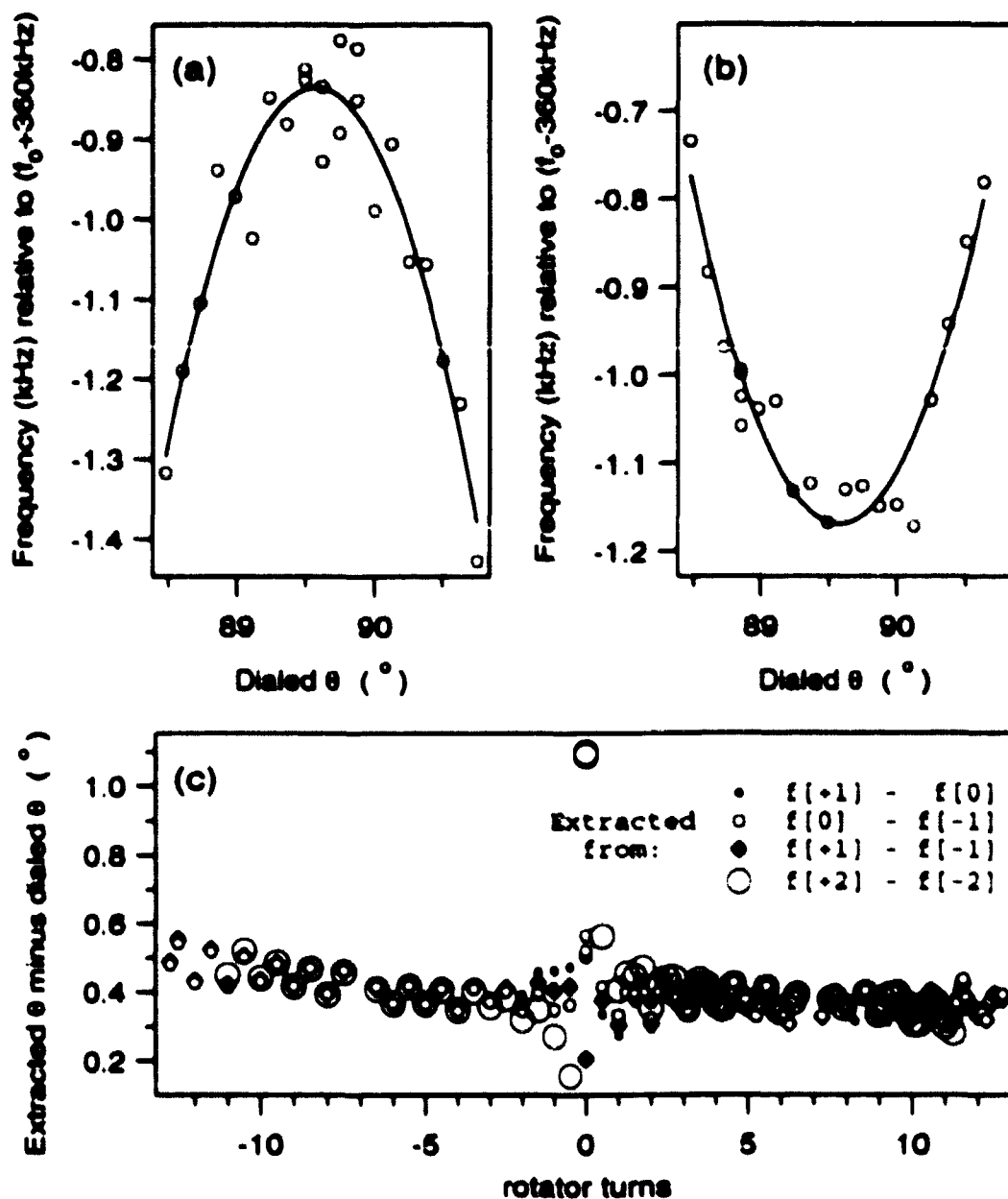


Figure B.3: (a,b) Determination of the quadrupole splitting constant ν_Q by precise measurements of the outer satellite frequencies as the sample is tilted through $\theta = 90^\circ$. Note that the synthesizer frequency was shifted by ± 360 kHz for each satellite.

(c) Using the obtained value of ν_Q , we can solve Equation 7.9 for any pair of satellite frequencies and thus extract θ . The difference between the extracted and the dialed values shows some periodic fluctuations as the rotator spiral advances through each turn, which is so-called tooth-to-tooth error. Note the average constant offset of about 0.4° between the extracted and the dialed values, which depends on how a particular sample is attached to the rotator platform.

Bibliography

- [1] K. von Klitzing, G. Dorda, M. Pepper, *Phys. Rev. Lett.* **45**, 494 (1980).
- [2] D. C. Tsui, H. L. Störmer, A. C. Gossard, *Phys. Rev. Lett.* **48**, 1559 (1982).
- [3] R. B. Laughlin, *Phys. Rev. Lett.* **50**, 1395 (1983).
- [4] *The Quantum Hall Effect*, R. E. Prange and S. M. Girvin, Eds., Springer, N. Y., 2nd ed., 1990.
- [5] T. Chakraborty and P. Pietiläinen, *The Quantum Hall Effects: Integral and Fractional*, Springer, Berlin, 2nd ed., 1990.
- [6] C. P. Slichter, *Principles of Magnetic Resonance*, Springer, N. Y., 3rd ed., 1990.
- [7] W. D. Knight, *Phys. Rev.* **76**, 1259 (1949).
- [8] A. W. Overhauser, *Phys. Rev.* **91**, 476 (1953).
- [9] S. E. Barrett, R. Tycko, L. N. Pfeiffer, and K. W. West, *Phys. Rev. Lett.* **72**, 1368 (1994).
- [10] M. A. Paalanen, D. C. Tsui, and A. C. Gossard, *Phys. Rev. B* **25**, 5566 (1982).
- [11] L. D. Landau and E. M. Lifshitz, *Quantum Mechanics: Non-Relativistic Theory*, Pergamon, Oxford, 3rd ed., 1977.

- [12] H. L. Störmer, *Physica B* **177**, 401 (1992); *Phys. Scr. T* **45**, 168 (1992).
- [13] For comprehensive reviews, see: *Composite Fermions*, ed. by O. Heinonen (World Scientific, 1998); *Perspectives in Quantum Hall Effects*, ed. by S. Das Sarma and A. Pinczuk (Wiley, New York, 1997); J. K. Jain, *Adv. Phys.* **41**, 105 (1992); R. L. Willett, *ibid.* **46**, 447 (1997).
- [14] For recent theoretical developments, see: N. Read, *Phys. Rev. B* **58**, 16262 (1998); A. Stern, B. I. Halperin, F. v. Oppen, and S. H. Simon, *ibid.* **59**, 12547 (1999); R. Shankar, cond-mat/9903064.
- [15] V. J. Goldman, B. Su, and J. K. Jain, *Phys. Rev. Lett.* **72**, 2065 (1994).
- [16] A. Auerbach, *Phys. Rev. Lett.* **80**, 817 (1998).
- [17] B. I. Halperin, *Helv. Phys. Acta* **56**, 75 (1983).
- [18] S. L. Sondhi, A. Karlhede, S. A. Kivelson, and E. H. Rezayi, *Phys. Rev. B* **47**, 16419 (1993).
- [19] H. A. Fertig, L. Brey, R. Côté, and A. H. MacDonald, *Phys. Rev. B* **50**, 11018 (1994).
- [20] Y. A. Bychkov, S. V. Iordanskii, and G. M. Eliashberg, *JETP Lett.* **33**, 143 (1981).
- [21] C. Kallin and B. I. Halperin, *Phys. Rev. B* **30**, 5655 (1984).
- [22] E. M. Purcell, H. C. Torrey, and R. V. Pound *Phys. Rev.* **69**, 37 (1946).
- [23] T. R. Carver and C. P. Slichter, *Phys. Rev.* **92**, 212 (1953); *ibid.* **102**, 975 (1956).
- [24] G. Lampel, *Phys. Rev. Lett.* **20**, 491 (1968).

- [25] *Optical Orientation*, F. Meier and B. Zakharchenya, Eds., North-Holland, N. Y., 1984.
- [26] S. E. Barrett *et al.*, *Phys. Rev. Lett.* **74**, 5112 (1995).
- [27] R. Tycko *et al.*, *Science* **268**, 1460 (1995).
- [28] E. H. Aifer, B. B. Goldberg, and D. A. Broido, *Phys. Rev. Lett.* **76**, 680 (1996).
- [29] M. J. Manfra *et al.*, *Phys. Rev. B* **54**, R 17 327 (1996).
- [30] A. Schmeller, J. P. Eisenstein, L. N. Pfeiffer, and K. W. West, *Phys. Rev. Lett.* **75**, 4290 (1995).
- [31] D. K. Maude *et al.*, *Phys. Rev. Lett.* **77**, 4606 (1996).
- [32] N. Read and S. Sachdev, *Phys. Rev. Lett.* **75**, 3509 (1995).
- [33] M. Kasner and A. H. MacDonald, *Phys. Rev. Lett.* **76**, 3204 (1996).
- [34] R. Hausmann, *Phys. Rev. B* **56**, 9684 (1997); C. Timm, P. Henelius, A. W. Sandvik, and S. M. Girvin, cond-mat/9710220.
- [35] C. A. Michal and R. Tycko, *Phys. Rev. Lett.* **81**, 3988 (1998).
- [36] T. Pietraß and M. Tomaselli, *Phys. Rev. B* **59**, 1986 (1999).
- [37] L. N. Pfeiffer, private communication.
- [38] L. N. Pfeiffer *et al.*, *Appl. Phys. Lett.* **61**, 1211 (1992).
- [39] P. Horowitz and W. Hill, *The Art of Electronics*, Cambridge University Press, Cambridge, 2nd ed., 1989.
- [40] D. D. Traficante, *Concepts in Mag. Res.* **2**, 181 (1990).

- [41] E. Fukushima and S. B. W. Roeder, *Experimental Pulse NMR: A Nuts and Bolts Approach*, Addison-Wesley, Reading (Massachusetts), 1981.
- [42] L. B. Loeb, *Fundamental Processes of Electrical Discharge in Gases*, Wiley, N. Y., 1939.
- [43] *IEEE Standard Dictionary of Electrical and Electronic terms*, Institute of Electrical and Electronic Engineers, 2nd ed., 1977.
- [44] R. C. Richardson and E. N. Smith, *Experimental Techniques in Condensed Matter Physics at Low Temperatures*, Addison-Wesley, Reading (Massachusetts), 1988.
- [45] A. Abragam, *Principles of Nuclear Magnetism*, Oxford Univ. Press, N. Y., 1961.
- [46] S. E. Barrett, private communication.
- [47] D. Heimann, Chap. 1 in *The Spectroscopy of Semiconductors*, D. G. Semler and C. L. Littler, Eds., Academic Press, San Diego, 1992.
- [48] P. Khandelwal *et al.*, *Phys. Rev. Lett.* **81**, 673 (1998).
- [49] N. N. Kuzma *et al.*, *Science* **281**, 686 (1998)
- [50] J. Winter, *Magnetic Resonance in Metals*, Oxford Univ. Press, London, 1971.
- [51] C. Weisbuch and B. Vinter, *Quantum Semiconductor Structures*, (Academic Press, San Diego, 1991).
- [52] G. Fishman, *Phys. Rev. B* **27**, 7611 (1983).
- [53] K. Moon *et al.*, *Phys. Rev. B* **51**, 5138 (1995).
- [54] T. Chakraborty and P. Pietiläinen, *Phys. Rev. Lett.* **76**, 4018 (1996).
- [55] R. K. Kamilla, X. G. Wu, and J. K. Jain, *Solid State Commun.* **99**, 283 (1996).

- [56] K. H. Ahn and K. J. Chang, *Phys. Rev. B* **55**, 6735 (1997).
- [57] R. J. Haug *et al.*, *Phys. Rev. B* **36**, 4528 (1987).
- [58] D. R. Leadley *et al.*, *Phys. Rev. Lett.* **79**, 4246 (1997).
- [59] R. L. Willett (private communication).
- [60] J. I. Kaplan and G. Fraenkel, *NMR of Chemically Exchanging Systems*, Academic Press, N. Y., 1980.
- [61] M. Mehring, *Principles of High Resolution NMR in Solids*, Springer-Verlag, Berlin, 2nd ed., 1983.
- [62] J. Sinova, S. M. Girvin, T. Jungwirth, and K. Moon, preprint cond-mat/9908029.
- [63] U. Piesbergen *et al.*, *Z. Naturforsch.* **18a**, 141 (1963).
- [64] V. Bayot, M. B. Santos, and M. Shavegan, *Phys. Rev. B* **46**, 7240 (1992).
- [65] A. E. Dementyev *et al.*, submitted to *Phys. Rev. Lett.*; preprint also available at cond-mat/9907280.
- [66] J. Kikkawa and D. Awschalom, *Phys. Rev. Lett.* **80**, 4313 (1998).
- [67] D. M. Frenkel, *Phys. Rev. B* **43**, 14228 (1991).
- [68] S. Taniguchi *et al.*, *Electron. Lett.* **32**, 552 (1996).
- [69] S. Nakamura *et al.*, *Appl. Phys. Lett.* **70**, 1417 (1997).
- [70] F. Ponce and D. Bour, *Nature* **386**, 351 (1997).
- [71] V. Fiorentini, F. Bernardini, F. Della Sala, A. Di Carlo, and P. Lugli, *Phys. Rev. B* **60**, 8849 (1999), preprint available at cond-mat/9905186.

- [72] A. Nurmikko and R. L. Gunshor, *Semicond. Sci. Technol.* **12**, 1337 (1997).
- [73] For recent examples of experimental developments in this area, see: F. K. Koschnick *et al.*, *Phys. Rev. B* **54**, R11042 (1996); G. Denninger and D. Reiser, *ibid.* **55**, 5073 (1997); E. R. Glaser *et al.*, *ibid.* **57**, 8957 (1998).
- [74] O. H. Han, H. K.C. Timken, and E. Oldfield, *J. Chem. Phys.* **89**, 6046 (1988).
- [75] D. P. Bour, N. M. Johnson, and L. Romano, data supplied by the growers.
- [76] I. Grzegory *et al.*, *Physica B* **185**, 99 (1993).
- [77] B. Filzinger *et al.*, *J. Mag. Res.* **125**, 280 (1997).